

Michael Pachler, BSc

**Structural and Electronic  
Properties of Quinacridone  
Grown on Cu(110) and  
Cu(110)-(2x1)O**

**MASTER THESIS**

For obtaining the academic degree  
Diplom-Ingenieur

Master Programme of  
Technical Physics



**Graz University of Technology**

Supervisor:

Ao.Univ.-Prof. Dipl.-Ing. Dr.techn. Roland Resel  
Institute of Solid State Physics  
in cooperation with the University of Graz

Graz, March 2015

# Contents

<b>1</b>	<b>Introduction</b>	<b>7</b>
<b>2</b>	<b>Acknowledgements</b>	<b>9</b>
<b>3</b>	<b>Theory</b>	<b>10</b>
3.1	Forces in molecular crystals . . . . .	10
3.1.1	Van der Waals force . . . . .	10
3.1.2	Hydrogen Bonds . . . . .	11
3.2	X-ray Diffraction . . . . .	12
3.2.1	Crystal . . . . .	12
3.2.2	Miller Indices . . . . .	14
3.2.3	Symmetry . . . . .	15
3.2.4	Infinite Grids and Finite Crystals . . . . .	15
3.2.5	Interaction of X-rays with Matter . . . . .	16
3.2.6	Braggs Law . . . . .	16
3.2.7	The Reciprocal Lattice . . . . .	17
3.2.8	General Theory of Diffraction . . . . .	17
3.2.9	The Laue condition and the Ewald sphere . . . . .	20
3.2.10	The Structure Factor and The Atomic Formfactor . . . . .	21
3.3	Different types of X-ray scans . . . . .	22
3.3.1	Specular Scan or $\theta/2\theta$ . . . . .	23
3.3.2	Rocking curve . . . . .	24
3.3.3	Polefigures . . . . .	25
3.3.4	Powder Diffraction and the $\theta/2\theta$ scan . . . . .	26
3.4	Ultraviolet Photoemission Spectroscopy . . . . .	28
3.4.1	The Three Step Model . . . . .	30
<b>4</b>	<b>Experimental Setup</b>	<b>35</b>
4.1	Siemens D501 Krystalloflex Goniometer . . . . .	35
4.2	Phillips X'Pert four circle Texture Goniometer . . . . .	35
4.3	UHV System: ADES 400 Spectrometer . . . . .	36
<b>5</b>	<b>Materials</b>	<b>39</b>
5.1	Cu(110) and Cu(110)-(2x1)O . . . . .	39
5.1.1	Creating the Cu(110)-(2x1)O reconstruction . . . . .	40
5.1.2	Substrate Cleaning . . . . .	40
5.2	Quinacridone . . . . .	41
5.2.1	$\alpha$ phase . . . . .	41
5.2.2	$\beta$ phase . . . . .	43
5.2.3	$\gamma$ phase . . . . .	44
<b>6</b>	<b>Experiments and Results</b>	<b>45</b>
6.1	Powder Diffraction . . . . .	45
6.2	"Thick" Film Samples . . . . .	48
6.2.1	Sample 1, Quinacridone on Cu(110) at $T_S$ 25 °C . . . . .	48
6.2.2	Sample 2, Quinacridone on Cu(110) at $T_S$ 140 °C . . . . .	56
6.2.3	Sample 3, Quinacridone on Cu(110)-(2x1)O at $T_S$ 25 °C . . . . .	62

6.3	Growth and Electronic Structure measurements of Monolayer, Multilayer and Bulk Films of Quinacridone on Cu(110) and Cu(110)-(2x1)O. . . . .	73
6.3.1	Experiments on Cu(110) at $T_S$ 25 °C . . . . .	74
6.3.2	Experiments on Cu(110) at $T_S$ 140 °C . . . . .	82
6.3.3	Experiments on a Cu(110)-(2x1)O at $T_S$ 25 °C . . . . .	89
<b>7</b>	<b>Conclusion</b>	<b>94</b>
<b>8</b>	<b>Table-, Picture- and Literature glossary</b>	<b>96</b>

## **EIDESSTATTLICHE ERKLÄRUNG**

### ***AFFIDAVIT***

Ich erkläre an Eides statt, dass ich die vorliegende Arbeit selbstständig verfasst, andere als die angegebenen Quellen/Hilfsmittel nicht benutzt, und die den benutzten Quellen wörtlich und inhaltlich entnommenen Stellen als solche kenntlich gemacht habe. Das in TUGRAZonline hochgeladene Textdokument ist mit der vorliegenden Masterarbeit/Diplomarbeit/Dissertation identisch.

*I declare that I have authored this thesis independently, that I have not used other than the declared sources/resources, and that I have explicitly indicated all material which has been quoted either literally or by content from the sources used. The text document uploaded to TUGRAZonline is identical to the present master's thesis/diploma thesis/doctoral dissertation.*

---

Datum / Date

---

Unterschrift / Signature

**Abstract** Quinacridone ( $C_{20}H_{12}N_2O_2$ ) is the hydrogen bonding analogon to pentacene, which is the worlds most studied organic semiconducting molecule. It has three different very well defined crystalline phases  $\alpha$ ,  $\beta$  and  $\gamma$ . The crystalline phase as well as the electronic structure and its orientation with respect to the contacts of an organic electronic device is of crucial importance for the performance. Different types of substrates (Cu(110), Cu(110)-(2x1)O) were used as atomically clean and ordered templates for the growth of Quinacridone thick films in ultra high vacuum. The substrate temperature ( $T_S$ ) was either room temperature or 140 °C. The crystal structures were characterized with a combination of different x-ray diffraction techniques (specular diffraction, rocking curves, polefigures). The present crystalline phase, the preferred orientation of crystallites with respect to the substrate surface and the alignment of the molecules relative to the substrate surface were determined. Two different crystalline phases were found. The  $\alpha$  phase was detected at evaporation onto the Cu(110) substrate at substrate temperature 140 °C. The film growth at  $T_S=25$  °C onto the Cu(110)-(2x1)O reconstruction resulted in an  $\alpha$  phase as well. The long axis of the molecules in the  $\alpha$  phase was aligned close to the [001] azimuth of the substrate. The  $\beta$  phase could be observed by evaporation at  $T_S=25$  °C onto the Cu(110) substrate. In this case the long molecular axis was inclined to both substrate directions. Ultraviolet photoemission spectroscopy (UPS) measurements were performed on monolayer and multilayer films. Dosing series (consecutive UPS measurements at different film thickness) were carried out to determine the evolution of the electronic structure with film thickness. The thickness of the monolayer, the workfunction and the ionization potential of the monolayer and a multilayer film on both substrates were determined. The monolayer was 3.2 Å thick and the corresponding workfunction on a Cu(110) substrate was 3.8 eV. The ionization potential of the monolayer was 5.4 eV and it increased to 6.1 eV in multilayer films. The workfunction for a monolayer on the Cu(110)-(2x1)O reconstruction was 4.22 eV, the corresponding ionization potential was 5.8 eV and it increased in the bulk to 6.3 eV. Heating series (consecutive measurements after different heating steps) of thick films were performed to investigate the temperature stability of Quinacridone. It was stable up to 200 °C and the monolayer was even stable at 330 °C. Angle resolved UPS series were conducted to investigate the azimuthal and angular behavior (takeoff angle) of the electronic structure. The measurements showed that the HOMO-9 had a very strong angular and azimuthal behavior, as confirmed by density functional theory calculations. The combination of experiment and theoretical calculation made it possible to obtain the orientation of the molecules on the substrate. These results are in excellent agreement with x-ray diffraction investigations.

**Kurzfassung** Quinacridone ( $C_{20}H_{12}N_2O_2$ ) ist das Wasserstoffbrücken-bildende Analogon zu Pentacen, welches das weltweit am meisten untersuchte halbleitende Molekül ist. Es besitzt drei unterschiedliche, aber wohl definierte Kristallstrukturen  $\alpha$ ,  $\beta$  und  $\gamma$ . Die Leistung eines organischen elektronischen Bauteils hängt sehr stark von der elektronischen Struktur, der vorhandenen kristallinen Phase und ihrer Orientierung im Bezug auf die elektronischen Kontakte ab. Es wurden unterschiedliche Substrate (Cu(110), Cu(110)-(2x1)O) für atomar kontrolliertes Kristallwachstum von Quinacridone in Ultrahochvakuum verwendet. Die Substrattemperatur war während des Wachstumsprozesses entweder 140 °C oder 25 °C. Die kristallinen Strukturen wurden mit Hilfe einer Kombination von verschiedenen Röntgenstrahl-Beugungstechniken charakterisiert (spekulare Messung,  $\omega$  Messung und Polefiguren). Die vorhandene kristalline Phase, die bevorzugte Orientierung der Kristallite relativ zu der Substratoberfläche und die Ausrichtung der Moleküle im Bezug auf die Substratoberfläche konnten bestimmt werden. Es wurden zwei verschiedene kristalline Phasen gefunden. Bei erhöhter Substrattemperatur (140 °C) während des Filmwachstum-Prozesses auf der Cu(110) Oberfläche konnte die  $\alpha$  Phase bestimmt werden. Das Filmwachstum bei Raumtemperatur (25 °C) auf der Cu(110)-(2x1)O Rekonstruktion führte ebenfalls zu einer  $\alpha$  Phase. Die lange Molekülachse in der  $\alpha$  Phase zeigte in die Richtung des [001] Substrat Azimuts. Die  $\beta$  Phase konnte nach Filmwachstum bei Raumtemperatur auf der Cu(110) Oberfläche gemessen werden. In diesem Fall war die Richtung der langen Molekülachse stark geneigt zu beiden Substratrichtungen. Um Informationen über die elektronische Struktur von Quinacridone zu erhalten wurde Ultraviolette-Photoelektronen-Spektroskopie (UPS) an monomolekularen und multimolekularen Filmen durchgeführt. Zur Bestimmung der Evolution der elektronischen Struktur wurden Aufdampfserien (aneinanderfolgende UPS Messungen bei unterschiedlicher Filmdicke) durchgeführt. Die Dicke der monomolekularen Schicht, die Arbeitsfunktion und das Ionisierungspotential von monomolekularen und multimolekularen Schichten konnten bestimmt werden. Die monomolekulare Schicht hat eine Dicke von 3.2 Å und die entsprechende Arbeitsfunktion auf einer Cu(110) Oberfläche beträgt 3.8 eV. Das Ionisierungspotential der monomolekularen Schicht beträgt 5.4 eV und steigt in der multimolekularen Schicht auf 6.1 eV an. Die Arbeitsfunktion einer monomolekularen Schicht auf einer Cu(110)-(2x1)O Rekonstruktion beträgt 4.22 eV. Das dazugehörige Ionisierungspotential hat einen Wert von 5.8 eV und erhöht sich in der multimolekularen Schicht auf 6.3 eV. Thermale Desorptions Messungen (aufeinanderfolgende Messungen nach bestimmten Heizschritten) zeigten, dass Quinacridone stabil bis 200 °C ist. Die monomolekulare Schicht ist bei 330 °C noch stabil. Winkelaufgelöste UPS Messreihen wurden durchgeführt um das azimutale und das winkelabhängige Verhalten der elektronischen Struktur von Quinacridone zu untersuchen. Das HOMO-9 hat ein sehr stark ausgeprägtes winkelabhängiges und azimutales Verhalten, welches mit Hilfe von Dichtefunktionalrechnungen bestätigt wurde. Durch die Kombination von Messung mit Simulation konnte die Orientierung der Moleküle auf dem Cu(110)-(2x1)O Substrat bestimmt werden. Die gefundene Ausrichtung der langen molekularen Achse stimmt sehr gut mit den Röntgenbeugungsmessungen überein.

# 1 Introduction

Over the years the importance of the organic electronics branch grew bigger and bigger. One of the main aspects was to create low cost devices as easy and stable as possible. Nowadays there is a wide variety of products and future applications. Organic solar cells, organic light emitting devices (OLEDs) and organic field effect transistors (OFET) are the most important examples. Mobile phones have an increasing percentage of organic displays. There are also bendable and curved displays available. A huge benefit of organic electronics is the possibility to print devices which reduces the costs significantly. In order to get organic electronics more competitive the performance of the devices has to be increased. Pentacene is the worlds most studied organic semiconducting molecule. Devices based on pentacene have a very strong initial performance but they degrade rather quickly under environmental conditions. The performance of these devices decrease significantly over time [11]. Alternative molecules have to be found, and they have to provide the necessary long time stability under environmental conditions. A more stable molecule is Quinacridone. It is a organic semiconductor with a HOMO-LUMO gap of 2 eV in a film and 3 eV in solution [7]. It is a reddish to violet pigment and is mainly used in the automobile and the coloring industry. It creates high performance paints and car coatings or more general industrial coatings with an exceptional color and weather fastness. Quinacridone is very similar to pentacene, however there is one major difference: Quinacridone forms hydrogen bonds. Hydrogen bonding is well known from nature e.g. DNA and cellulose form hydrogen bonds. They essentially stabilize the structure of the molecular system, which is very important for the device's performance in environmental conditions. Figure 1 shows pentacene on the left side and its hydrogen bonding analogon Quinacridone on the right side.

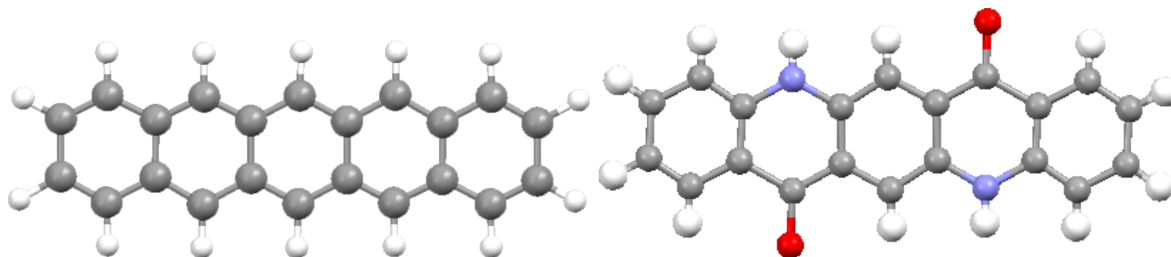


**Figure 1:** The left side shows pentacene ( $C_{22}H_{14}$ ). It has a full intramolecular  $\pi$ -conjugation. This conjugation is broken in Quinacridone due to the change of atoms. The right side displays a single Quinacridone ( $C_{20}H_{12}N_2O_2$ ) molecule. The coloring is as follows: grey... carbon, white... hydrogen, red... oxygen, blue... nitrogen

Quinacridone is industrially harvested with a volume of several thousand tons a year which leads to a very low price. It has three different well known crystalline phases  $\alpha$ ,  $\beta$  and  $\gamma$ . The present crystalline phase and its orientation with respect to the electronic contacts of the device will be of crucial influence for the device performance. Studies showed that Quinacridone based organic devices have nearly no degradation after 140 days. Pentacene devices show significant performance loss after 30 days [11]. That makes Quinacridone very interesting for further investigations. A unique combination of x-ray diffraction and ultraviolet photoemission spectroscopy techniques was applied. Together they provide spatial and electronic information about the sample. These techniques complement each other very well. Clean and atomically controlled samples were prepared at an Ultra-High-Vacuum system. They were investigated at the ADES 400 spectrometer via ultraviolet photoemission spectroscopy. Electronic properties like the workfunction and the ionization potential were determined as well as the angle resolved behavior of the electronic orbitals itself. Samples for x-ray diffraction experiments were characterized at the Philips

X'Pert four circle texture goniometer. Information about the crystalline phase, the orientation of the crystallites with respect to the substrate, as well as the alignment of the molecules relative to the substrate surface was determined.

## 2 Acknowledgements

First I want to thank both of my supervisors Prof. Roland Resel and Prof. Michael Ramsey for giving me the chance to do my master thesis in an interdisciplinary working environment. I also want to thank them for their never ending support, their guidance, their patience and their constructive ideas.

I want to show my gratitude towards Dr. Thomas Ules for his many hours at the ADES system and the countless delightful discussions.

I also want to thank MSc. Sascha Pomp for being such a great office mate.

Prof. Peter Puschnig and DI. Daniel Lueftner performed theoretical calculations for me and therefore I am very grateful.

I would also like to thank the k-room, and the working group of the surface science division for all the help that was provided.

And finally I want to thank my family, my closest friends and my girlfriend Angelina for everything they did for me. You always had my back! I couldn't have done it without you.

## 3 Theory

### 3.1 Forces in molecular crystals

The reason for the formation of molecular crystals are intermolecular forces. Table 1 gives an overview of the different types of forces, their range, strength and directionality [13, 16, 17, 25]. Usually a good first approximation for the crystalline structure of molecules is given by the close packing principle. The latter is not valid for Quinacridone since it has directional bonds (hydrogen bonds). The most important forces for the crystal formation of Quinacridone are van der Waals interactions (vdW) and hydrogen bonds. Van der Waals interactions are attractive or repulsive and non directional. Dispersion forces bring molecules together, they also try to align them but their alignment qualities are rather weak. That is the point where the hydrogen bonds come in. They are highly directional and responsible for the three crystalline phases of Quinacridone. In the next two chapters these two forces are discussed briefly.

**Table 1:** Summary of the intermolecular forces responsible for crystal formation.[25]

Interaction Type	Range	Directional	Energy [kJ/mol]	Energy [ $k_b T$ ]
Covalent	very short	yes	100-900	40-360
Hydrogen bond	very short	yes	10-170	4-68
Charge-charge	$r^{-1}$	no	503	200
Charge-dipole	$r^{-2}$	yes	97	39
Dipole-dipole	$r^{-3}$	yes	19	7.5
van der Waals	$r^{-6}$	no	0.5-5	0.2-2

#### 3.1.1 Van der Waals force

The van der Waals interaction consists of three components [13, 16]:

- Dispersion force (London force)
- Keesom interaction (permanent dipole force)
- Debye interaction (induced dipole force)

**Keesom force** The Keesom force describes the electrostatic interaction energy between two permanent dipoles. This force can be attractive or repulsive and decreases with  $\frac{1}{r^6}$ .

**Debye force** The Debye force accounts for the electrostatic energy between a permanent dipole and an induced dipole. This force decreases with  $\frac{1}{r^6}$ .

The most important force concerning Quinacridone is the dispersion force. Quinacridone is a non polar molecule with no dipole-dipole interaction between neighboring molecules (no Keesom interaction). There is also no dipole-induced dipole interaction (Debye) which leaves just the the London dispersion force.

**Dispersion force** Gravitational force is in a way very similar to the dispersion force. Gravity works on all atoms and molecules, it does not matter if they are neutral like e.g. helium. Dispersion forces are always present between atoms. They work on neutral atoms and molecules and do not need charged molecules or permanent dipoles. The origin are quantum mechanical charge fluctuations. One possible example for this effect is helium. The time average of the dipole moment is zero but at any instant time there is a finite dipole moment present, given by the instantaneous position of the electrons respective to the protons. This dipole generates a electric field, and polarizes neighboring atoms. The resulting interaction between these two dipoles is an attractive force, non vanishing over time. This phenomenon was described by London in 1937. Equation 1 describes the interaction energy between two identical atoms or molecules.

$$w(r) = -\frac{C_{disp}}{r^6} = -\frac{3}{4} \frac{\alpha_0^2 h\nu}{(4\pi\epsilon_0)^2 r^6} \quad (1)$$

The polarizability of the molecule is described by  $\alpha_0$  and  $h\nu$  stands for the first ionization potential (I). Although the origin of the dispersion force is quantum mechanical, the force itself is essentially electrostatic. It has a  $\frac{1}{r^6}$  dependence, just like the Keesom and the Debye effect. As good as the London equation looks it also has its faults. It assumes that molecules only have one ionization potential. Additionally it cannot handle interactions of molecules in a solvent. Mc Lachlan presented a generalized theory of the van der Waals forces in 1963. Which included the Keesom, the Debye and the Dispersion effect in one equation.[13]

Equation 2 describes the vdW energy of two molecules in a medium according to the general theory of vdW forces between molecules.

$$w(r) = -\frac{C_{vdW}}{r^6} = -\frac{6kT}{(4\pi\epsilon_0)^2 r^6} \sum_{n=0,1,\dots}^{\infty} \frac{\alpha_1(i\nu_n)\alpha_2(i\nu_n)}{\epsilon_3^2(i\nu_n)} \quad (2)$$

Where  $\alpha_1(i\nu_n)$  and  $\alpha_2(i\nu_n)$  describe the polarizabilities of the molecules and  $\epsilon_3^2(i\nu_n)$  stands for the permittivity of the medium.  $\nu_n$  are the different absorption frequencys ( $n= 0,1,2,\dots$ ) according to equation 3.

$$\nu_n = \frac{2\pi kT}{h} n \quad (3)$$

### 3.1.2 Hydrogen Bonds

Hydrogen bonds are one of the most common interactions in chemistry. They occur in nature, and can be found e.g in water, proteins, cellulose and DNA. The high melting point of water and the shapes of folded proteins are a result of hydrogen bonding. They are a key factor in the shape determination of a structure and have a crucial influence on the stability of the system (they stabilize DNA). There are many different kinds of hydrogen bonds. Strong hydrogen bonds have a strength up to covalent bonds, whereas weak hydrogen bonds are very little stronger than van der Waal's interactions. Most of the hydrogen bonds have a strength in between these two types. A hydrogen bond is an attractive highly directional interaction. A hydrogen atom is covalently bonded to a donor atom D, interacting with an acceptor atom A. [8, 15] The donor atom has a higher electronegativity than the hydrogen atom. It consequently attracts the electron cloud of the hydrogen atom, leaving it with a "positive" partial charge. This partial unshielded

hydrogen atom interacts with the acceptor atom (e.g. polarisable  $\pi$  electrons). These circumstances are displayed in figure 2. A definition for the hydrogen bonds is given by the IUPAC and is as follows: "A typical hydrogen bond may be depicted as  $X-H \cdots Y-Z$ , where the three dots denote the bond.  $X-H$  represents the hydrogen-bond donor. The acceptor may be an atom or an anion  $Y$ , or a fragment or a molecule  $Y-Z$ , where  $Y$  is bonded to  $Z$ . In specific cases  $X$  and  $Y$  can be the same with both  $X-H$  and  $Y-H$  bonds being equal. In any event, the acceptor is an electron rich region such as, but not limited to, a lone pair in  $Y$  or a  $\pi$ -bonded pair in  $Y-Z$ ." [1] Table 2 gives an overview of the different types of hydrogen bonds. It shows their type of interaction, expected bond lengths, bond angles and the corresponding energies.

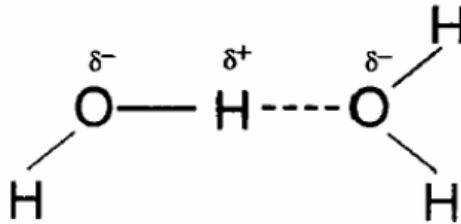


**Figure 2:** Schematic of hydrogen bonding in water. O... oxygen, H... hydrogen and  $\delta^\pm$  describes the partial charge of the atom. [25]

**Table 2:** The classification of hydrogen bonds into strong, moderate and weak bonds. [8]

Parameters	Strong	Moderate	Weak
D-H... A interaction	Mostly covalent	Mostly electrostatic	Electrostatic
Bond lengths	D-H $\approx$ H... A	D-H < H... A	D-H $\ll$ H... A
H... A [ $\text{\AA}$ ]	$\sim 1.2 - 1.5$	$\sim 1.5 - 2.2$	$2.2 - 3.2$
D-H... A [ $\text{\AA}$ ]	$2.2 - 2.5$	$2.5 - 3.2$	$3.2 - 4.0$
Bond angles [ $^\circ$ ]	$170 - 180$	$130 - 180$	$90 - 150$
Bond energy [ $\frac{kJ}{mol}$ ]	$60 - 170$	$15 - 60$	$< 15$

## 3.2 X-ray Diffraction

### 3.2.1 Crystal

A basic principle to describe a crystal in solid state physics is the combination of the Bravais lattice with a certain group also called the basis.

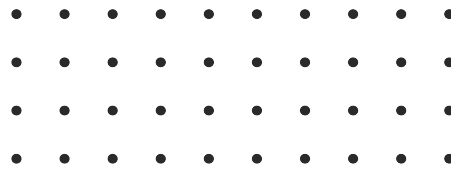
**Bravais lattice** The Bravais lattice is an infinite periodic arrangement of points and is shown in figure 3 part (a). In this case it is a two dimensional squared lattice and it reproduces the periodicities in the crystal. Figure 4 illustrates a two dimensional Bravais lattice with different choices for the translational lattice vectors  $\vec{a}_1$ ,  $\vec{a}_2$  and  $\vec{a}_3$ . The real space lattice is spanned up by Equation 4. Every point  $\vec{r}$  will be a point of the real space lattice, with the integers  $u_1$ ,  $u_2$  and  $u_3$  and the translational vectors  $\vec{a}_1$ ,  $\vec{a}_2$  and  $\vec{a}_3$ . The Bravais lattice looks identical from every point of the lattice. Mathematically expressed nothing else than equation 5 where  $\vec{r}'$  stands for any new point of the lattice. The lattice is called primitive if equation 5 holds for any two points of the lattice. This also defines the primitive translation vectors  $\vec{a}_i$ . The volume of the primitive unit cell can be calculated by the triple product stated in equation 6. There

is no cell with a smaller volume than the primitive unit cell, and it can serve as a building block for the crystal structure. [12, 18, 22]

$$\vec{r} = u_1 \vec{a}_1 + u_2 \vec{a}_2 + u_3 \vec{a}_3 \quad (4)$$

$$\vec{r}' = \vec{r} + u_1 \vec{a}_1 + u_2 \vec{a}_2 + u_3 \vec{a}_3 \quad (5)$$

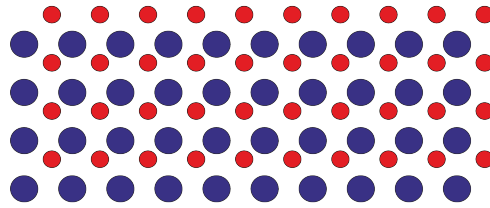
$$V = |\vec{a}_1 \cdot \vec{a}_2 \times \vec{a}_3| \quad (6)$$



(a) Space lattice



(b) Basis with two different atoms



(c) Crystal structure

**Figure 3:** The crystal structure is built by a convolution of the basis with the Bravais lattice. (a) shows a squared Bravais lattice. (b) is a basis with two different atoms, and the resulting crystal structure is depicted in (c).

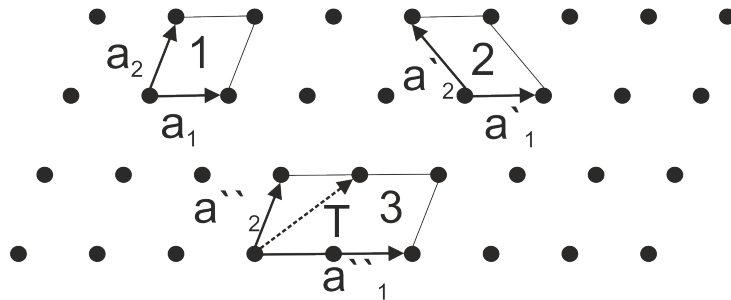


**Figure 4:** A two dimensional Bravais lattice with three different choices for the translation vectors  $\vec{a}_i$  of the lattice. The vectors  $\vec{a}_1, \vec{a}_2, \vec{a}'_1$  and  $\vec{a}'_2$  are primitive lattice vectors. Any point of the lattice fulfills equation 5 with these vectors. The area of the parallelograms 1 and 2 are the same and they could be taken as a primitive cell. The lattice vectors  $\vec{a}''_1$  and  $\vec{a}''_2$  are no primitive translation vectors and therefore the area of the parallelogram 3 differs from the area of the parallelograms 1 and 2.

**Basis** A basis can consist out of atoms, ions, molecules etc... An example of a two atomic basis is given in figure 3 (b). As mentioned earlier a basis is the unit which is put on every single lattice point to obtain the crystal structure. Every component of the basis has a certain distance to the associated lattice point. This fact is given by equation 7 with  $0 \leq x_j, y_j, z_j \leq 1$ .  $x_j$ ,  $y_j$  and  $z_j$  are the fractional coordinates. The index  $j$  denotes to different atoms and therefore  $r_j$  is the position of the atom  $j$  in real space. [18]

$$r_j = x_j \vec{a}_1 + y_j \vec{a}_2 + z_j \vec{a}_3 \quad (7)$$

### 3.2.2 Miller Indices

The orientation of a crystal plane and its normal vector is given by the Miller indices  $hkl$ . They are determined in the following way:

- Find the intercepts of the three crystal axes  $\vec{a}_1$ ,  $\vec{a}_2$  and  $\vec{a}_3$  with the plane of interest. It does not matter whether primitive lattice vectors are used or not.
- Build the inverse value of  $\frac{1}{\text{interceptvalue}}$
- Multiply with the least common multiple. The resulting numbers are integer values with the same ratio as before. They are called the index of the plane or Miller indices  $hkl$ .

If a plane cut a crystal axis in infinity, the corresponding value will be zero. Figure 5 shows an example of the Miller indices. The plane intercepts the crystal axis at the points 4, 5 and 7. The reciprocal value times the least common multiple leads to a Miller indices  $(hkl)$  of  $(35\ 28\ 20)$ . The indices are going to have a bar over a integer value if the intercept is on the negativ side of the crystal axis. [18, 22]

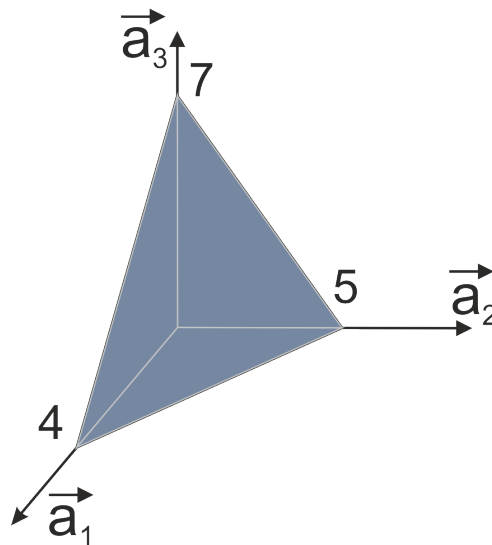


**Figure 5:** Schematic for the derivation of the Miller indices.

The use of the brackets around the Miller indices:

- $( hkl )$  represents a plane
- $\{hkl\}$  represents a family of equivalent planes

The indices u, v and w are used in real space (they are no Miller indices) and the notation is as follows:

- $[ uvw ]$  represents a crystallographic direction
- $\langle uvw \rangle$  represents a family of equivalent crystallographic directions

### 3.2.3 Symmetry

Symmetry is the invariance of an object to some operations. If a crystal is considered, lattice symmetry in the geometrical meaning is the invariance of a crystal under a certain transformation. This means the symmetry operation reproduces the crystal. There are different kinds of symmetry groups. For example the linear translation  $\vec{T}$  which is defined by equation 8 leads to an infinite lattice. [5, 18, 22]

$$\vec{T} = u_1\vec{a}_1 + u_2\vec{a}_2 + u_3\vec{a}_3 \quad (8)$$

Other transformations form the group of rotational symmetries. This group consist of rotations and rotoinversions. Rotations are rotations around a specific axis which map the crystal back onto itself. Rotoinversions are transformations which rotate the crystal first and invert it afterward around a center of symmetry (point symmetry). The combined amount of translational and rotational symmetries for a given Bravais lattice or a given crystal structure lead to the space group. Table 3 shows the point and space groups for a Bravais lattices with a highly symmetric basis (spheres) and for general crystal structures with an arbitrary basis.

**Table 3:** Point and space groups of Bravais lattices and crystal structures. [22]

	Bravais lattice (spherical symmetric base)	crystal structure (arbitrary base)
number of point groups	7 crystal systems	32 crystallographic point groups
number of space groups	14 bravais lattices	230 space groups

### 3.2.4 Infinite Grids and Finite Crystals

A Bravais lattice is an infinite repetition of points with a certain periodicity. In contrast to that a real crystal has a finite size. How is it possible to use something infinite big to describe something finite? If a real crystal is big enough, so that the majority of points is far away from the surface, the surfaces presence can be neglected. Therefore the assumption of an infinite crystal is very helpful.[22]

### 3.2.5 Interaction of X-rays with Matter

This section will give a very brief overview of the different types of interactions between x-rays and matter in the energy range of interest. [5, 14]

- Photoionization: An incident photon knocks a bound electron away from its atom. Energy and momentum are transferred in the process. Photoionization is an inelastic scattering process (incoherent).
- Compton scattering: A photon exchanges energy and momentum with an approximately free electron (low binding energy). The resulting photon has less energy than before. Compton scattering is an inelastic scattering process (incoherent).
- Thomson scattering: The incoming radiation induces oscillations of the electrons of the atoms with the same frequency (Hertz dipole), resulting in coherent dipole radiation with the wavelength of the incident x-rays. This effect leads to elastic scattering and is the important effect for x-ray diffraction experiments.

### 3.2.6 Braggs Law

X-ray diffraction is an extremely important tool to study crystal structures. A very simple approach to this rather complex phenom is Braggs law. It treats the elastic scattering of x-ray photons from the atomic planes. Figure 6 shows atomic planes parallel to each other with a certain netplane distance  $d$ . The incident radiation is diffracted specularly. This means the incident angle  $\theta$  between the incoming wave and the atomic plane equals the angle between the outgoing wave and the atomic plane. The geometrical path difference of the outgoing waves equals  $2d \sin \theta$ . Constructive interference is obtained when the path difference between the different outgoing waves equals an integer ( $n$ ) times the wavelength  $\lambda$  of the x-rays (equation 9).

Only a small part of the incoming radiation will be diffracted from the first atomic plane. The rest is going to be diffracted by following planes. Each atomic plane diffracts  $10^{-3}$  to  $10^{-5}$  % of the incident radiation. The amount of planes that contribute to a Bragg reflection is of the order  $10^2$ . The more slits an optical grid has, the better defined the peaks are. The situation is similar here. The more atomic planes are contributing the better the peak is going to be defined. There is just one major difference, the only thing one really notices if there are just a few planes contributing: The peak will broaden. This effect is described by the Scherrer equation. Bragg's law considers only the periodicity of a lattice and just describes the position of the peaks. It contains no information about the basis of the lattice points and consequently no information about the intensity of the peaks. [14, 18]

$$2d \sin \theta = n\lambda \tag{9}$$

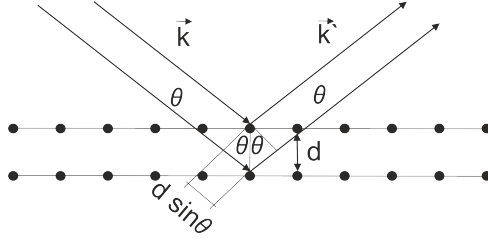


**Figure 6:** Bragg diffraction on a set of parallel atomic planes.  $\vec{k}$  is the wavevector of the incoming x-ray radiation,  $\vec{k}'$  is the wavevector of the outgoing radiation.  $\theta$  is the angle between the wavevector and the net planes.  $d$  is the netplane distance and  $2d \sin \theta$  is the path difference.

### 3.2.7 The Reciprocal Lattice

The reciprocal lattice or the so called momentum space is spanned by the reciprocal lattice vectors. They can be calculated straight forward by Equations 10, 11 and 12 if the real space lattice vectors are known. If the real space lattice vectors are primitive so are their reciprocal lattice vectors. [18, 22]

$$\vec{b}_1 = 2\pi \frac{\vec{a}_2 \times \vec{a}_3}{\vec{a}_1 \cdot \vec{a}_2 \times \vec{a}_3} \quad (10)$$

$$\vec{b}_2 = 2\pi \frac{\vec{a}_3 \times \vec{a}_1}{\vec{a}_1 \cdot \vec{a}_2 \times \vec{a}_3} \quad (11)$$

$$\vec{b}_3 = 2\pi \frac{\vec{a}_1 \times \vec{a}_2}{\vec{a}_1 \cdot \vec{a}_2 \times \vec{a}_3} \quad (12)$$

A vector  $\vec{G}$  in the momentum space is constructed similar to realspace and has the following form:

$$\vec{G} = v_1 \vec{b}_1 + v_2 \vec{b}_2 + v_3 \vec{b}_3 \quad (13)$$

The major difference compared to a real space vector is that they have units in terms of  $\frac{1}{length}$ . Later chapters will show that the reciprocal space and its vectors  $\vec{G}$  are of extreme importance for diffraction.

### 3.2.8 General Theory of Diffraction

Since x-rays are electromagnetic waves it is possible to describe the amplitude of the wave at a certain point in space at a specific time with equation 14. By diffracting a wave like that of a solid some assumptions have to be made in order to treat it mathematically in an easier way. The incoming wave  $\vec{k}_0$  hits a lattice and induces wavelets at every scattering point. These wavelets are spherical waves and do not interact with the incoming wave. This means the speed of the incoming wave is not modified. Additionally these scattered wavelets do not scatter with other lattice points. They go right through the crystal. A fixed phase relation between the incoming waves and the scattered wavelets is assumed and there is also no absorption. The general scattering problem is displayed in figure 7. The radiation source is at point Q. The distance from the source to the target  $\vec{R}$  is far enough so that the emitted spherical waves nearly becomes a plane wave (Frauenhofer limit). Every point of the target emits  $\vec{r}$  spherical

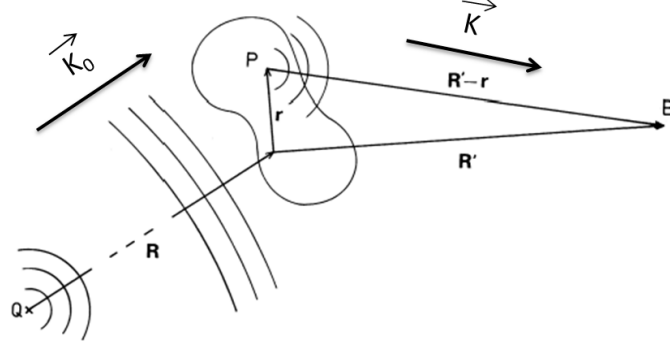


**Figure 7:** Schematic for the derivation of the scattered radiation from the target to a point of interest B. Q is the position of the radiation source. P is the point where the scattering happens and B is the point of interest.[12]

wavelets. One is interested in the combined effect of all the wavelets in point B. The electromagnetic wave described by equation 14 has a well defined phase at any time and therefore we can derive the resulting phase in point B geometrically (equation 19). [12, 14]

$$A(\vec{r}, t) = A_0 e^{i(\vec{k}_0 \vec{r} - \omega_0 t)} \quad (14)$$

The amplitude in point P (defined due to the vector  $\vec{r}$ ) is given by equation 15. This wave gets scattered in point P and has the following amplitude at point B (equation 16).

$$A_P(\vec{r}, t) = A_0 e^{i(\vec{k}_0(\vec{R} + \vec{r}) - \omega_0 t)} \quad (15)$$

$$A_B(\vec{B}) = A_P(\vec{r}, t) \rho(\vec{r}) \frac{e^{i\vec{k}|\vec{R}' - \vec{r}|}}{|\vec{R}' - \vec{r}|} \quad (16)$$

The scattering event itself is described by the complex scattering density  $\rho(\vec{r})$ . Equation 16 simply states that the amplitude in point B after one scattering event in point P is given by the amplitude of the undisturbed radiation times the scattering density times the characteristic radiation of a spherical wavelet. The wave vector  $\vec{k}$  has the same direction as  $\vec{R}' - \vec{r}$  and therefore equation 16 simplifies to equation 17.

$$A_B(\vec{B}) = A_P(\vec{r}, t) \rho(\vec{r}) \frac{e^{i\vec{k}(\vec{R}' - \vec{r})}}{|\vec{R}' - \vec{r}|} \quad (17)$$

Since the point of Interest B is far away from the target the distance  $\vec{R}'$  is much greater then the distance  $\vec{r}'$  ( $\vec{R}' \geq \vec{r}'$ ) and equation 17 turns into equation 18.

$$A_B(\vec{B}) = A_P(\vec{r}, t) \rho(\vec{r}) \frac{e^{i\vec{k}(\vec{R}' - \vec{r})}}{\vec{R}'} \quad (18)$$

Inserting equation 15 into equation 18 leads to the final form for the amplitude in point B of a single

scatterer (equation 19).

$$A_B(\vec{\mathbf{B}}) = A_0 e^{i(\vec{\mathbf{k}}_0(\vec{\mathbf{R}}+\vec{\mathbf{r}})-\omega_0 t)} \rho(\vec{\mathbf{r}}) \frac{e^{i\vec{\mathbf{k}}(\vec{\mathbf{R}}'-\vec{\mathbf{r}})}}{\vec{\mathbf{R}}'} \quad (19)$$

To take into account the scattering from every point in the target material one has to integrate over the whole target volume. This leads to the total scattering amplitude in point B which is illustrated in equation 20 and 21 .

$$A_B(\vec{\mathbf{B}}) = \int A_0 e^{i(\vec{\mathbf{k}}_0(\vec{\mathbf{R}}+\vec{\mathbf{r}})-\omega_0 t)} \rho(\vec{\mathbf{r}}) \frac{e^{i\vec{\mathbf{k}}(\vec{\mathbf{R}}'-\vec{\mathbf{r}})}}{\vec{\mathbf{R}}'} d\vec{\mathbf{r}} \quad (20)$$

$$A_B(\vec{\mathbf{B}}) \propto e^{-i\omega_0 t} \int \rho(\vec{\mathbf{r}}) \frac{e^{i\vec{\mathbf{r}}(\vec{\mathbf{k}}_0-\vec{\mathbf{k}})}}{\vec{\mathbf{R}}'} d\vec{\mathbf{r}} \quad (21)$$

By scattering due to a rigid lattice  $\rho(\vec{\mathbf{r}})$  is time independent and therefore the only time dependence is in  $e^{-i\omega_0 t}$  with the frequency  $\omega_0$  which corresponds to the initial frequency. The result is energy conservation which implies only elastic scattering. As mentioned earlier the wavelength has to be approximately the netplane distance of the crystal in order to get diffraction to work. That's why it is not possible to measure the amplitude of the wave as a function of space and time. Only the intensity will be detected in a x-ray measurement. The intensity is proportional to the absolute square of the amplitude. Using the definition of the scattering vector  $\vec{\mathbf{K}} = \vec{\mathbf{k}} - \vec{\mathbf{k}}_0$  equation 22 can be obtained.

$$I(\vec{\mathbf{K}}) \propto |A_B(\vec{\mathbf{B}})|^2 \propto \left| \int \rho(\vec{\mathbf{r}}) e^{-i\vec{\mathbf{K}}\vec{\mathbf{r}}} d\vec{\mathbf{r}} \right|^2 \quad (22)$$

The scattering intensity is proportional to the absolute square of the Fourier transform of the scattering density. Since we cannot measure the amplitude a direct calculation of the scattering density is impossible. The information about the phase is lost. However the other way around works. One can start with guessing a crystal structure, calculate the diffraction pattern and compare it to the measured pattern. If it fits the correct crystal structure is determined, otherwise adjusting the model parameters is necessary.  $n(\vec{\mathbf{r}})$  is the electron density for a crystal. The electron density is a periodic function in real space and fulfills any translation  $\vec{\mathbf{T}}$  (equation 24). As a result of that  $n(\vec{\mathbf{r}})$  has to obey equation 23. Every periodic function in real space can be expanded in a Fourier series. The vectors used in the expansion have to preserve  $n(\vec{\mathbf{r}})$  translational invariance. The only vectors that are able to do this are the reciprocal lattice vectors  $\vec{\mathbf{G}}$ . The Fourier expansion of the electron density can be seen in equation 25.

$$n(\vec{\mathbf{r}} + \vec{\mathbf{T}}) = n(\vec{\mathbf{r}}) \quad (23)$$

$$\vec{\mathbf{T}} = u_1 \vec{\mathbf{a}}_1 + u_2 \vec{\mathbf{a}}_2 + u_3 \vec{\mathbf{a}}_3 \quad (24)$$

$$\rho(\vec{\mathbf{r}}) = n(\vec{\mathbf{r}}) = \sum_{\vec{\mathbf{G}}} n_{\vec{\mathbf{G}}} e^{i\vec{\mathbf{G}}\vec{\mathbf{r}}} \quad (25)$$

Inserting this expansion into the formula for the intensity (equation 22) leads to the scattering conditions for periodic structures (equation 26).

$$I(\vec{\mathbf{K}}) \propto \frac{|A_B(\vec{\mathbf{B}})|^2}{\vec{\mathbf{R}}'} \left| \int \sum_{\vec{\mathbf{G}}} n_{\vec{\mathbf{G}}} e^{i(\vec{\mathbf{G}}-\vec{\mathbf{K}})\vec{\mathbf{r}}} d\vec{\mathbf{r}} \right|^2 \quad (26)$$

Most of the contributes in equation 26 will cancel out. The reason is simple: A crystal is build of a lot of identical unit cells. For example one at point  $\vec{\mathbf{r}}$  and one at point  $-\vec{\mathbf{r}}$ . The major difference there is a minus sign and they are going to cancel out. The only non canceling contributions arise when  $\vec{\mathbf{G}} = \vec{\mathbf{K}}$ . Equation 27 illustrates these circumstance.

$$\int e^{i(\vec{\mathbf{G}}-\vec{\mathbf{K}})\vec{\mathbf{r}}} d\vec{\mathbf{r}} = V \quad (27)$$

A diffracted beam will only occur when the scattering vector  $\vec{\mathbf{K}}$  equals a reciprocal lattice vector  $\vec{\mathbf{G}}$ . This condition is called the Laue condition and the resulting intensity has the form of equation 28.

$$I(\vec{\mathbf{K}} = \vec{\mathbf{G}}) \propto \frac{|A_0|^2}{\vec{\mathbf{R}}'^2} |n_{\vec{\mathbf{G}}}|^2 V^2 \quad (28)$$

As expected the intensity is volume depended. The Intensity distribution decreases with  $V^{-1}$  around a maximum. Another interesting fact is that the electron density is real and as a result of that every intensity pattern shows a center of inversion. This is valid as long as no absorption occurs and the scattering density stays a real quantity. The intensity spot can be labeled in terms of the reciprocal lattice vectors. Equation 13 reminds of the definition of a reciprocal lattice vector. It's integers  $v_1$ ,  $v_2$  and  $v_3$  can be used for labeling since the intensity is directly proportional to a specific reciprocal lattice vector. [12, 14]

$$I_{v_1 v_2 v_3} \propto |n_{v_1 v_2 v_3}|^2 \quad (29)$$

### 3.2.9 The Laue condition and the Ewald sphere

The Laue condition is one of the most fundamental diffraction conditions. It is valid for the diffraction of any kind of radiation as long as there is a periodic structure involved.

Figure 8 shows the Ewald construction for elastic scattering. Starting point is the reciprocal lattice, where the incoming wave vector gets attached towards a reciprocal lattice point. This point will be the origin. Every cross in the figure indicates a reciprocal lattice point. Since we are treating elastic scattering  $\vec{\mathbf{k}}_0$  and  $\vec{\mathbf{k}}$  have the same magnitude namely  $\frac{2\pi}{\lambda}$  with  $\lambda$  the wavelength of the incoming radiation. Now one has to draw a circle centered around the starting point of  $\vec{\mathbf{k}}_0$  with the radius of  $\frac{2\pi}{\lambda}$ . Every point on the circle fulfills the condition of the scattering vector  $\vec{\mathbf{K}} = \vec{\mathbf{k}} - \vec{\mathbf{k}}_0$ . The Laue condition  $\vec{\mathbf{K}} = \vec{\mathbf{G}}$  will be satisfied when the sphere cuts through a reciprocal lattice point. This means every time the Ewald sphere coincides with a reciprocal lattice point diffraction will occur. The diffraction peak is directly related to its  $\vec{\mathbf{G}}$  vector

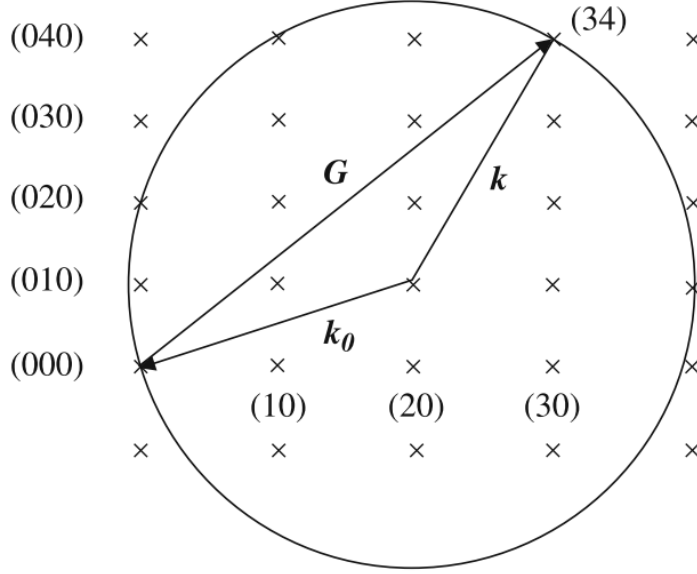


**Figure 8:** Ewald construction for elastic scattering with the incoming wavevector  $\vec{k}_0$ , the outgoing wavevector  $\vec{k}$  and the reciprocal lattice vectors  $\vec{G}$

and will, as mentioned earlier, be labeled with the integers  $(v_1 v_2 v_3)$ . [12, 18]

### 3.2.10 The Structure Factor and The Atomic Formfactor

Equation 27 only gives information about the position of the diffraction maximum. To obtain information about the intensity of a peak equation 26 has to be solved and therefore the Fourier coefficients of the scattering density must be calculated. They can be obtained out of the inversion of the fourier series. In the case of a crystal we assume again the electron density as the scattering density and the inversion of the fourier series is shown in equation 30. [12, 14, 18]

$$n_{\vec{G}} = \frac{1}{V_c} \int_{cell} n(\vec{r}) e^{-i\vec{G}\vec{r}} \quad (30)$$

The integral extends over the volume of a unit cell. Assuming a crystal is build up of N identical cells makes it possible to rewrite the equation for the scattering amplitude into equation 31.

$$A_{\vec{G}} = N \int_{cell} n(\vec{r}) e^{-i\vec{G}\vec{r}} dV = N S_{\vec{G}} \quad (31)$$

The scattering intensity from a certain lattice vector  $\vec{G}$  (since  $\vec{K} = \vec{G}$ ) is the product of the number of crystal cells times the structure factor  $S_{\vec{G}}$ . The x-rays get scattered due to the electrons. Most of the electrons are located in a rather narrow region around the atom. x-rays undergo elastic Thomson scattering with those electrons. They are also scattered by the spread out valence electrons but this contribution is rather small and can be neglected. It is very common to rewrite the electron density as it is stated in equation 32. Where s stands for the total number of atoms in the cell,  $r_j$  is the vector pointing at atom j and  $n_j$  is the electron density.  $n_j$  takes account for the local electron density of the

atom  $j$ .

$$n(\vec{\mathbf{r}}) = \sum_{j=1}^s n_j(\vec{\mathbf{r}} - \vec{\mathbf{r}}_j) \quad (32)$$

Using equation 32 allows to rewrite the structure factor defined in equation 31 with integrals over the individual atoms in the unit cell.  $S_{\vec{\mathbf{G}}}$  turns into equation 33. In the last step the coordinate transformation  $\vec{\mathbf{r}}' = \vec{\mathbf{r}} - \vec{\mathbf{r}}_j$  was used.

$$S_{\vec{\mathbf{G}}} = \sum_{j=1}^s \int_{atom} n_j(\vec{\mathbf{r}} - \vec{\mathbf{r}}_j) e^{-i\vec{\mathbf{G}}\vec{\mathbf{r}}} dV = \sum_{j=1}^s e^{-i\vec{\mathbf{G}}\vec{\mathbf{r}}_j} \int_{atom} n(\vec{\mathbf{r}}') e^{-i\vec{\mathbf{G}}\vec{\mathbf{r}}'} dV \quad (33)$$

The integral in equation 33 describes the scattering power of a single atom. It is called the atomic form factor and it is defined in equation 34.

$$f_j = \int n(\vec{\mathbf{r}}') e^{-i\vec{\mathbf{G}}\vec{\mathbf{r}}'} dV \quad (34)$$

The integration extends over the hole space. Since the electron density of a specific atom is located in space only a small part of the integration region is going to contribute to  $f_j$ . Equation 33 and 34 can be used to write the structure factor in its final form.

$$S_{\vec{\mathbf{G}}} = \sum_j f_j e^{-i\vec{\mathbf{G}}\vec{\mathbf{r}}_j} \quad (35)$$

Applying the structure factor to a certain lattice will always result in the following:

$$S_{\vec{\mathbf{G}}}(v_1 v_2 v_3) = \sum_j f_j e^{-i2\pi(v_1 x_j + v_2 y_j + v_3 z_j)} \quad (36)$$

To obtain equation 36 equation 37 was used.  $v_1$ ,  $v_2$  and  $v_3$  are the integers of the reciprocal lattice vector  $\vec{\mathbf{G}}$  whereas  $x_j$ ,  $y_j$  and  $z_j$  stand for the integers describing the atomic position in real space in a cell.

$$\vec{\mathbf{G}} \cdot \vec{\mathbf{r}} = 2\pi(v_1 x_j + v_2 y_j + v_3 z_j) \quad (37)$$

The structure factor describes the interference between the waves scattered from different atoms inside the cell and the atomic form factor stands for the interference effects inside a single atom.[12]

### 3.3 Different types of X-ray scans

Three different types of x-ray measurement techniques were used during this master thesis. Together with additional simulations these measurement techniques provide an extremely powerful toolkit for determining the present crystalline structure, the orientation of the crystallites, general order and the alignment of the molecules.

### 3.3.1 Specular Scan or $\theta/2\theta$

In a specular scan the angle of incidence between the incoming radiation and the substrate surface has to equal the outgoing angle between the scattered waves and the substrate surface. Figure 10 illustrates this circumstance. It also shows the angle  $2\theta$  which is the only accessible quantity in the experiment. The wavelength is fixed by the x-ray source and the netplane distance is given by the specimen. Figure 9 is a close up picture of the measurement system. The red arrow on the left side marks the detector. It is mounted on the Goniometer circle and is able to move along the scope of the circle. The sample holder is shown in the middle of the picture. It has three degrees of freedom. Rotations of the sample around the angles  $\phi$  and  $\psi$  are possible as well as the tilting of the hole stage. The arrow on the right side marks the x-ray source which is fixed in space. To achieve the wanted geometry during the measurement the detector has to be rotated with twice the angular speed of the specimen. That way the condition for specular diffraction is fulfilled at any time. It is nothing else than the condition for specular diffraction. The position of the detector and the position of the x-ray source combined with the used apertures leave a very narrow window for the radiation to get through the geometry. One could say  $\vec{k}_0$  is fixed by the position of the radiation source and the scattered wave  $\vec{k}'$  is given by the detector position at a specific time. Constructive interference will be detected at certain  $2\theta$  angles. [2]

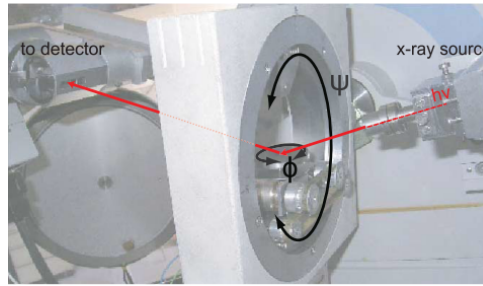


**Figure 9:** The Philips XPERT four circle texture goniometer [26]. It was used in this work for specular scans, rocking curves and polefigure measurements.

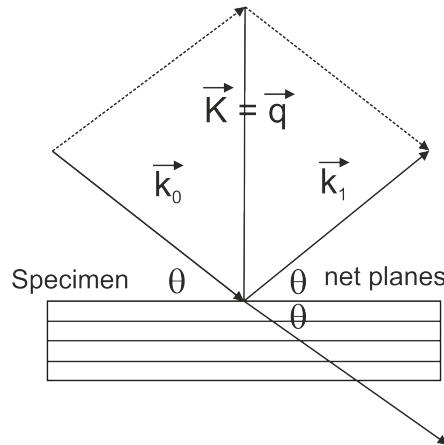


**Figure 10:** Schematic of the diffraction geometry in a specular scan.  $\vec{k}_0$  is the incoming wavevector,  $\vec{k}_1$  is the outgoing wavevector and  $\vec{q}$  accounts for the scattering vector.

A peak will be obtained if Braggs law (equation 9) and the parallelism condition (equation 38) are satisfied simultaneously. The parallelism conditions states that the normal vector of a specimen plane has to be

parallel to the scattering vector  $\vec{q}$ .

$$\vec{n} \parallel (\vec{k} - \vec{k}_0) = \vec{q} = \vec{K} \quad (38)$$

As mentioned earlier the measurement system leaves a narrow window for the radiation to reach the detector. A peak will only have intensity if the structure factor does not equal zero (equation 35). In a specular scan only planes parallel to the substrate surface are detected. These planes have different netplane distances  $d$ . In the case of a copper(110) crystal only the family of planes parallel to the surface will lead to diffraction peaks. Figure 11 describes the same situation but in reciprocal space. The Ewald construction shows that in a  $\theta/2\theta$  scan the scattering vector  $\vec{q}$  consist only of a  $z$  component. It is a scan along the direction of the scattering vector  $\vec{q}$  in reciprocal space. Since the magnitude of the scattering vector changes different netplane distances are detected.[2]

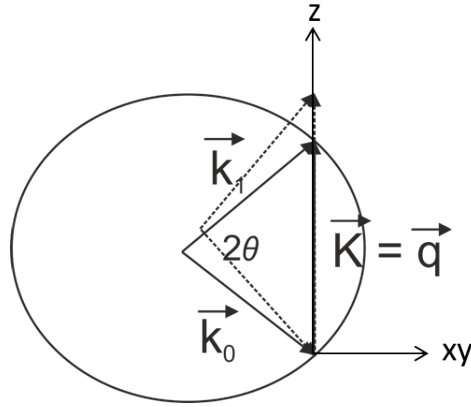


**Figure 11:** Ewald construction for the  $\theta/2\theta$  scan geometry.  $\vec{k}_0$  and  $\vec{k}_1$  are the wavevectors of the incoming and outgoing radiation.  $\vec{k}_0$  is pointing towards the origin in reciprocal space and the dotted lines display the situation after some steps in a  $\theta/2\theta$  scan. As one can see  $\vec{q}$  changes only in magnitude not in direction.

### 3.3.2 Rocking curve

A rocking curve is performed at an already known peak. The detector is set to an angle of  $2\theta$  corresponding to the netplane distance of interest. Since the position of the detector and the x-ray source is fixed a specific scattering vector  $\vec{q}$  is selected. According to Braggs law only the selected netplane distance contributes to the detected signal. Figure 12 shows the specimen with different crystallite orientations on top of the substrate and their normalvectors  $\vec{n}$ .

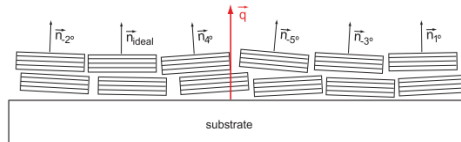


**Figure 12:** Specimen: different crystallite orientations on top of the substrate. The normal vector of each crystallite is given by  $\vec{n}$ .  $\vec{q}$  stands for the scattering vector. [2]

By tilting the sample the parallelism condition is going to be probed. Every normal vector of the different crystallites will once satisfy the parallelism condition 38. A rocking curve reveals the spatial distribution

of the crystallites. The rocking curve of a copper(110) single crystal would result in a very sharp peak at a defined position by Bragg's law. This is clear since a single crystal basically is one big crystallite and as a result of that only very little broadening of the rocking curve occurs (due to the mosaicity of the crystal). In contrast to that a rocking curve over a powder of the material of interest would result in a rather flat line. Because in a powder all crystallites are orientated randomly, there will be always a crystallite satisfying the parallelism condition and Bragg's law at every tilt step. As a result of that a rocking curve measurement probes the spatial orientation of the crystallites (mosaicity). A rocking curve in reciprocal space is shown in figure 13. The geometry between  $\vec{k}_0$  and  $\vec{k}_1$  stays the same after the tilt. The only thing that is changing is the angle of incidence relative to the netplanes of the sample. As a consequence the wavevectors behave as shown in figure 13. They are both tilted relative to each other by the same angle and the change in the scattering vector  $\vec{K} = \vec{q}$  is perpendicular to the direction in a specular scan. Its magnitude stays the same. In this case the vector component  $\vec{q}_z$  will get lowered and  $\vec{q}_{xy}$  increases. (equation 39).[2]

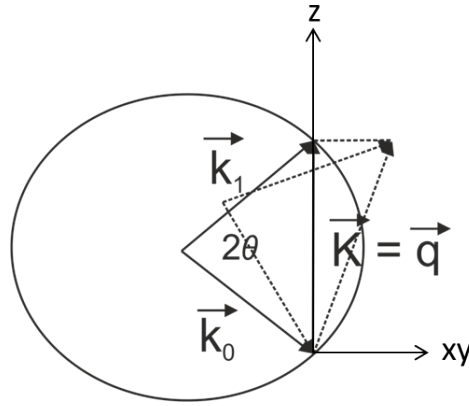


**Figure 13:** Basic principal of a rocking curve measurement in reciprocal space by making use of the Ewald construction.  $\vec{k}_0$  is the incoming radiation and  $\vec{k}_1$  are the diffracted x-rays.  $\vec{k}_0$  is pointing towards the origin in reciprocal space. The scattered lines display the situation after a couple of tilts. The scattering vector changes perpendicularly to the direction of change in a specular scan.

$$\vec{q} = \vec{q}_z + \vec{q}_{xy} \quad (39)$$

### 3.3.3 Polefigures

A polefigure is an extremely efficient tool to determine the orientation of a crystal and the orientations of the crystallites with respect to each other. Figure 14 displays the principle of making a polefigure. The angles  $\phi$  and  $\psi$  are the angles to the rotational axis of our system, also shown in figure 9. Every polefigure is performed around a specific angle  $2\theta$  and according to Bragg's law only a specific netplane distance  $d_{hkl}$  is going to contribute. One starts with zero rotation ( $\phi = 0$ ) and zero tilt angle ( $\psi = 0$ ). After detecting the signal for a defined amount of time  $\phi$  gets rotated from  $0^\circ$  to  $360^\circ$  with a certain step width  $\Delta\psi$ . Followed by a tilt  $\Delta\psi$  and again a rotation of  $\phi$  from  $0^\circ$  to  $360^\circ$  with the same step width. This is done until the whole upper hemisphere is probed. Meaning all possible combinations of the tuples  $(\psi, \phi)$  with  $\psi = (0 : \Delta\psi : 90)^\circ$  and  $\phi = (0 : \Delta\phi : 360)^\circ$  were reached following the scheme above. This is essentially a stereographic projection. However, there is one major difference. Everything from a polefigure is from a single net plane distance  $d_{hkl}$  where as in a normal stereographic projection every

netplane distance contributes. A peak in a polefigure is called enhanced pole density (EPD) and thanks to the way a polefigure measurement proceeds every single EPD has its own tuple of angles  $(\psi, \phi)$ . A measurement at a specific angle covers more than just the scattering angle  $2\theta$ . It detects  $2\theta \pm \frac{1}{2}\Delta 2\theta$ .  $\Delta 2\theta$  is given mainly due to the acceptance angle of the detector, which is mostly determined by the receiving slit. This can be seen in figure 15. The grey oval is the probed volume instead of just a point. The mapped volume of a single polefigure in reciprocal space is the volume of a half sphere shell and it is illustrated in figure 16. To obtain poles from different netplane distances  $d_{hkl}$  the angle  $2\theta$  has to be adjusted. Wide range mapping of the reciprocal space is also easily possible with this technique. The stepwidth in  $2\theta$  has to be adjusted carefully. One of its many applications would be the determination of the crystal symmetries [2]. A polefigure can be seen in figure 17. This image should demonstrate the geometrical look of the stereographic projection from the polar net behind a polefigure. There are always  $10^\circ$  between the circles even if the spacing between the circles is not equally distributed. The distance between the circle gets bigger due to the nature of a stereographic projection at higher tilt angles. The radial direction corresponds to the angle  $\psi$  and the direction along the circumference is the angle  $\phi$ .

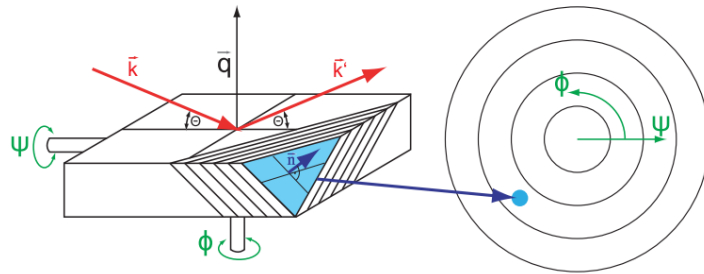


**Figure 14:** Scheme of a polefigure measurement. Every point in the polefigure has its own unique tuple  $(\psi, \phi)$ . [2]

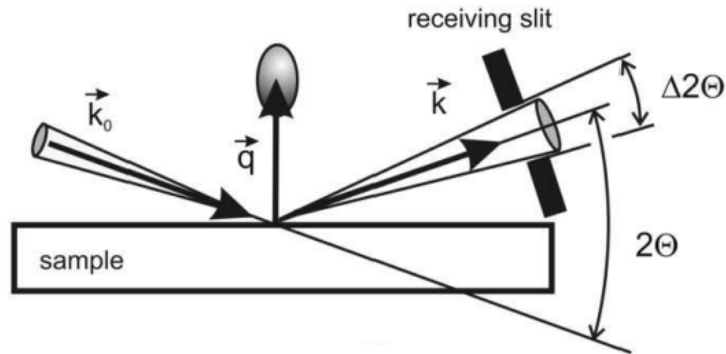


**Figure 15:** Diffraction geometry for a polefigure measurement at a specific  $2\theta$  peak. A clear view of the limiting aperture in front of the detector is given. The grey oval is the probed volume at specific point in reciprocal space. [26]

### 3.3.4 Powder Diffraction and the $\theta/2\theta$ scan

As mentioned earlier a  $\theta/2\theta$  scan only measures intensity when Bragg's law is fulfilled and the scattering vector is parallel to the normal vector of the substrate surface. The crystallites in a powder are statistically distributed and therefore the conditions above will always be fulfilled. A powder scan looks like an overlay of  $\theta/2\theta$  scans in a rotational crystal experiment where additionally all possible rotational axes

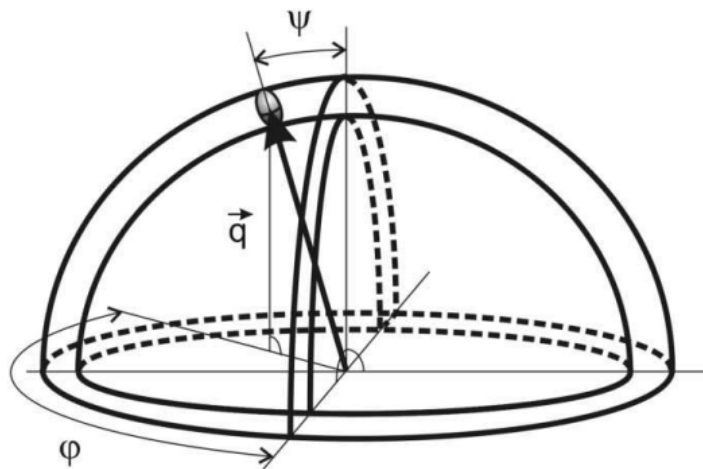


**Figure 16:** The volume mapped in reciprocal space by a single polefigure is a half sphere shell. The thickness of the shell is defined by the beam broadening and the acceptance angle of the detector (defined by the receiving slit)[26]

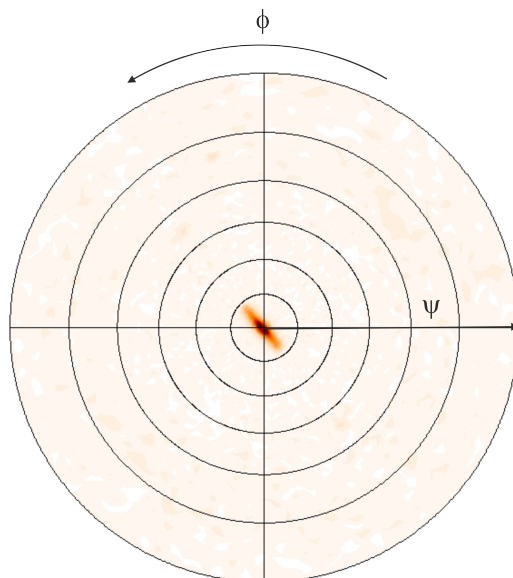


**Figure 17:** Example of a polefigure measured at  $2\theta = 41.197$  which corresponds to the (1-12) plane of the  $\alpha$  phase. The angle  $\psi$  goes into the radial direction. From one circle to another there are always  $10^\circ$  steps even if the spacing gets wider with increasing radius.  $\phi$  goes along the circumference from  $0^\circ$  to  $360^\circ$ .

are present.

### 3.4 Ultraviolet Photoemission Spectroscopy

The most important experimental technique to obtain information about the occupied electronic states is photoemission spectroscopy. Photoemission spectroscopy is based on the famous photoelectric effect, which was postulated in a paper by Einstein in 1905.

$$E_k(max) = h\nu - e\varphi \quad (40)$$

Equation 40 correlates the maximum obtainable kinetic energy  $E_k(max)$  of the photo electrons, which were emitted during irradiation of a solid with photons of the frequency  $\nu$ . The potential  $e\varphi$  is in the case of a solid metal nothing less than the workfunction. ([4, 10, 21])

A solid surface is irradiated by mono-energetic photons. As a consequence electrons will be emitted from the target. Those electrons are analyzed with respect to their kinetic energy. If the exciting radiation is from the ultraviolet spectral regime one talks about ultraviolet photoemission spectroscopy (UPS). In the case of x-rays its called x-ray photoemission spectroscopy (XPS). XPS is mostly used for chemical analysis whereas UPS is used for the investigation of the electronic structure of the valence levels. UPS measures the density of states. If one is interested in the dispersion of the electronic bands  $E(\vec{k})$  or  $E(\vec{k}_{||})$  additional information is required. The emission direction of the electrons has to be determined. Therefore a electron energy analyzer with a very small angular aperture is useful. This method is known as angle resolved photoemission spectroscopy (ARUPS). ARUPS no longer measures the density of states. The geometry of ARUPS is shown in figure 18.

The incidence angle of the electromagnetic radiation is called  $\alpha$ , and  $\theta$  specifies the take off angle.  $\phi$  is the in plane angle. In contrast to x-ray diffraction the take off angle in UPS is measured with respect to the plane normal and not with the netplane itself. The direction of the emitted electron can be described with the tuple  $(\theta, \phi)$ . The momentum vector of the electron outside the solid ( $\vec{k}^{ex}$ ) can be split up into its two components  $\vec{k}_{||}^{ex}$  and  $\vec{k}_{\perp}^{ex}$ . It is possible to split the parallel component of the emitted electron  $\vec{k}_{||}^{ex}$  further up into  $\vec{k}_x^{ex}$  and  $\vec{k}_y^{ex}$ . All this splitting up is valid since the equations 41 and 42 have to be fulfilled at all times. It is also important to mention that  $\vec{k}_{||}^{ex}$  means nothing else than the k vector parallel to the surface of the solid. Therefore x and y are the in plane coordinates of the surface. The direction of the electromagnetic field of the incoming photons and its vector potential  $\vec{A}$  are essentially determined by the incidence angle of the photon, the polarization of the light, and the plane of incidence.

$$\vec{k}^{ex} = \vec{k}_{||}^{ex} + \vec{k}_{\perp}^{ex} \quad (41)$$

$$\vec{k}_{||}^{ex} = \vec{k}_x^{ex} + \vec{k}_y^{ex} \quad (42)$$

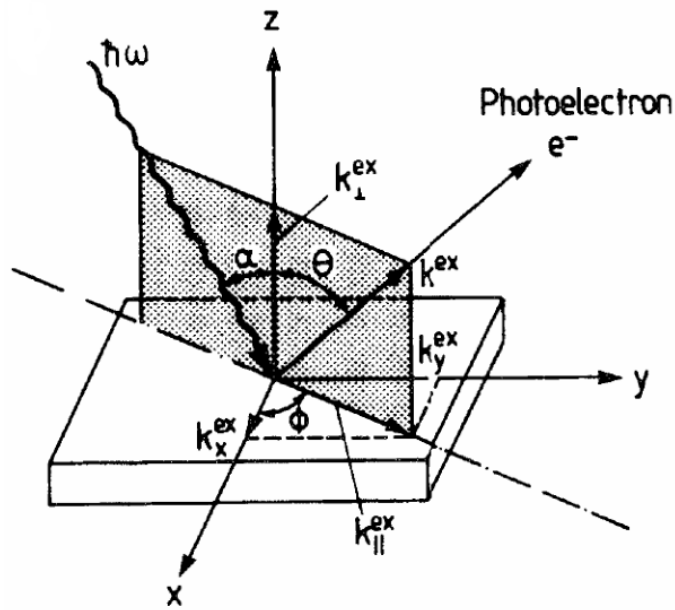


**Figure 18:** Geometry of an ARUPS experiment. The incoming radiation has the energy  $\hbar\omega$ .  $\alpha$  determines the angle of incidence and  $\theta$  is the the takeoff angle.  $\phi$  describes the inplane rotation. The gray shaded area is the scattering plane defined by the incoming wavevector, the outgoing wavevector and the scattering vector. [21]

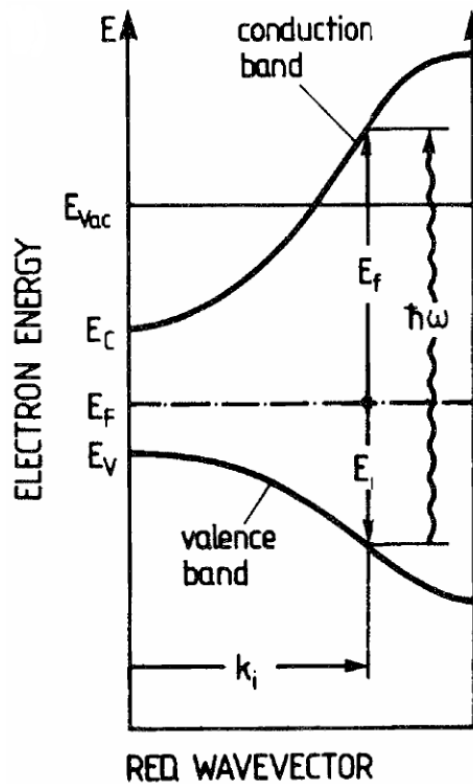


**Figure 19:** Schematic of the electronic excitation process in a semiconductor. Only vertical transitions are taken into account.  $E_F$  is the energy reference level (Fermi energy). The energy of the final state  $E_f$  and the initial state  $E_i$  are given with respect to  $E_F$ . [21]

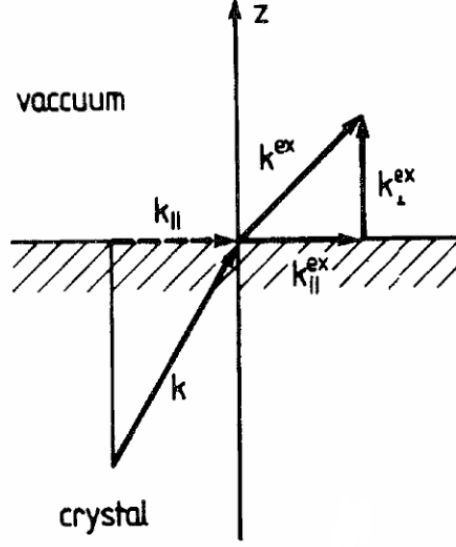


**Figure 20:** Schematic for the transmission of the emitted electron through the surface and conservation of the momentum parallel to the surface. [21]

### 3.4.1 The Three Step Model

A theoretical approach for the process of removing an electron from the solid and depositing it at the detector is the three step model. The Photoemission process is split up into three parts, which are assumed to be independent.[21]

1. Optical excitation from an initial state  $k_i$  to an final state  $k_f$  in the solid (figure 19)
2. Propagation of excited electron to the surface
3. Emission of the electron from the solid into vacuum (figure 20)

Of course these three parts are not independent of each other. But that is an important assumption and it brings simplicity. Every step of the model is treated independently, resulting in a factorization of the total probability of the emission current. The transition probability of an optical excitation process is described by Fermi's golden rule (equation 43 and 44).

$$W_{fi} = \frac{2\pi}{\hbar} \left| \langle f, \vec{k} | H, i, \vec{k} \rangle \right|^2 \delta(E_f(\vec{k}) - E_i(\vec{k}) - \hbar\omega) \quad (43)$$

$$W_{fi} = \frac{2\pi}{\hbar} m_{fi} \delta(E_f(\vec{k}) - E_i(\vec{k}) - \hbar\omega) \quad (44)$$

The Hamiltonian in the dipole approximation is given as follows

$$H = \frac{e}{2m} (\vec{A} \cdot \vec{p} + \vec{p} \cdot \vec{A}) \cong \frac{e}{m} \vec{A} \cdot \vec{p} \quad (45)$$

In the limit of long wavelengths  $\lambda > 100\text{\AA}$   $\vec{A}$  is nearly constant and therefore  $\vec{p}$  and  $\vec{A}$  commute. The delta function in equation 43 takes account for the energy conservation of the excitation process. It essentially means that the energy of the final state  $E_f(\vec{k})$  has to equal the energy of the initial state

$E_i(\vec{\mathbf{k}})$  plus the energy of the photon  $\hbar\omega$  (figure 19). Electrons can only be detected when their kinetic energy is higher than the energy of the vacuum level and the  $\vec{\mathbf{k}}$  vector of the final state is pointing outwards of the surface. This means that  $\vec{\mathbf{k}}_{\perp} > 0$ . The internal electron current density directed towards the surface with energy  $E$  and wave vector  $\vec{\mathbf{k}}$  is described by equation 46.

$$I^{int}(E, \hbar\omega, \vec{\mathbf{k}}) \propto \sum_{f,i} m_{fi} f(E_i) \delta(E_f(\vec{\mathbf{k}}) - E_i(\vec{\mathbf{k}}) - \hbar\omega) \delta(E - E_f(\vec{\mathbf{k}})) \quad (46)$$

$f(E_i)$  is the Fermi function. To detect an electron of kinetic energy  $E$ ,  $E$  has to equal  $E_f$  (last delta function in 46). The next step is the propagation of the electrons described by equation 46 to the surface. A big fraction of electrons undergoes inelastic scattering. They change their energy depending on the kind of interaction (for example phonon scattering, plasmon scattering,..). Therefore all the information about the initial electronic position of the electron is lost. The electrons which don't undergo inelastic scattering still have this information. The transition probability to the surface (D) can be described with the mean free path length  $\lambda$ .  $\lambda$  is a function of the crystallographic orientation, the Energy and the  $\vec{\mathbf{k}}$  vector.

$$D(E, \vec{\mathbf{k}}) \propto \lambda(E, \vec{\mathbf{k}}) \quad (47)$$

The mean free path length is the reason why UPS is so surface sensitive. All the inelastically scattered electrons contribute to the secondary electron background. The third step describes the transmission of the electrons through the surface (figure 20). One can imagine it as the scattering process of the electron wave function with the potential of the surface atoms. This potential has a translational symmetry parallel to the surface (2D symmetry) and no symmetry perpendicular to the surface. As a consequence, only  $\vec{\mathbf{k}}_{\parallel}$  is conserved.  $\vec{\mathbf{k}}_{\parallel}^{\text{ex}}$  outside the crystal equals  $\vec{\mathbf{k}}_{\parallel}$  inside the crystal plus a reciprocal lattice vector of the surface.

$$\vec{\mathbf{k}}_{\parallel}^{\text{ex}} = \vec{\mathbf{k}}_{\parallel} + \vec{\mathbf{G}}_{\parallel} \quad (48)$$

The kinetic energy of the electron on the vacuum side is described with the energy of a free electron (equation 49).

$$E_{kin} = \frac{\hbar^2 \vec{\mathbf{k}}^{\text{ex}2}}{2m} = \frac{\hbar^2}{2m} (\vec{\mathbf{k}}_{\parallel}^{\text{ex}2} + \vec{\mathbf{k}}_{\perp}^{\text{ex}2}) = E_f - E_{vac} \quad (49)$$

$$\hbar\omega = E_f - E_i = E_{kin} + \phi + E_B \quad (50)$$

By combining equation 49 and 50 the following expression for  $\vec{\mathbf{k}}_{\parallel}^{\text{ex}}$  is obtained:

$$\vec{\mathbf{k}}_{\parallel}^{\text{ex}} = \sqrt{\frac{2m}{\hbar^2}} \sqrt{\hbar\omega - E_B - \phi \sin \Theta} \quad (51)$$

After a few more mathematical transformations equation 52 is reached. The parallel momentum of the  $\mathbf{k}$  vector is entirely determined by experimental parameters. This equation can be used to compare an experiment with a simulation.

$$\mathbf{k}_{\parallel}^{\vec{e}x} = \sqrt{\frac{2m}{\hbar^2}} \sqrt{E_k \sin \Theta} \quad (52)$$

The transmission through the surface is described by the transmission rate multiplied with the delta function for the conservation of parallel momentum. Equation 53 shows that fact. The definition of  $T$  is shown in equation 54 and 55 . It takes into account that only electrons with positive  $\mathbf{k}_{\perp}^{\vec{e}x}$  can be observed.

$$T(E, \vec{\mathbf{k}}) \cdot \delta(\mathbf{k}_{\parallel} + \vec{\mathbf{G}}_{\parallel} - \mathbf{k}_{\parallel}^{\vec{e}x}) \quad (53)$$

$R$  is a constant with  $R \leq 1$ !

$$T(E, \vec{\mathbf{k}}) = 0 \text{ for } \mathbf{k}_{\perp}^{\vec{e}x2} = \frac{2m}{\hbar^2} (E_f - E_{vac}) - (\mathbf{k}_{\parallel} + \vec{\mathbf{G}}_{\parallel})^2 < 0 \quad (54)$$

$$T(E, \vec{\mathbf{k}}) = R \text{ for } \mathbf{k}_{\perp}^{\vec{e}x2} = \frac{2m}{\hbar^2} (E_f - E_{vac}) - (\mathbf{k}_{\parallel} + \vec{\mathbf{G}}_{\parallel})^2 > 0 \quad (55)$$

As mentioned earlier the total emission current in the three step model is nothing else then the product of its three components.

$$I^{ex}(E, \hbar\omega, \mathbf{k}_{\parallel}^{\vec{e}x}) = I^{int}(E, \hbar\omega, \vec{\mathbf{k}}) D(E, \vec{\mathbf{k}}) T(E, \vec{\mathbf{k}}) \delta(\mathbf{k}_{\parallel} + \vec{\mathbf{G}}_{\parallel} - \mathbf{k}_{\parallel}^{\vec{e}x}) \quad (56)$$

$$\propto \sum_{f,i} m_{fi} f(E_i(\vec{\mathbf{k}})) \delta(E_f(\vec{\mathbf{k}}) - E_i(\vec{\mathbf{k}}) - \hbar\omega) \delta(E - E_f(\vec{\mathbf{k}})) \quad (57)$$

$$\cdot \delta(\mathbf{k}_{\parallel} + \vec{\mathbf{G}}_{\parallel} - \mathbf{k}_{\parallel}^{\vec{e}x}) D(E, \vec{\mathbf{k}}) T(E, \vec{\mathbf{k}}) \quad (58)$$

So far many body aspects were excluded. Non interacting electrons were assumed. A system of  $N$  non interacting electrons is described by the following wave function (equation 59).

$$\psi = \phi_1(\vec{\mathbf{r}}_1) \phi_2(\vec{\mathbf{r}}_2) \cdots \phi_N(\vec{\mathbf{r}}_N) \quad (59)$$

$\phi_1(\vec{\mathbf{r}}_1)$  stands for the single electron wave function of electron 1 at place  $r_1$ . Since the electrons are not interacting with each other the Hamiltonian can be written as a sum of one particle operators. Application of those wave functions on the Hamiltonian  $H$  leads to equations 63.

$$H\psi = H \cdot (\phi_1(\vec{\mathbf{r}}_1)\phi_2(\vec{\mathbf{r}}_2) + \cdots \phi_N(\vec{\mathbf{r}}_N)) \quad (60)$$

$$H\psi = H_1\phi_1(\vec{\mathbf{r}}_1) + H_2\phi_2(\vec{\mathbf{r}}_2) + \cdots + H_N\phi_N(\vec{\mathbf{r}}_N) \quad (61)$$

$$E\psi = E_1\phi_1(\vec{\mathbf{r}}_1) + E_2\phi_2(\vec{\mathbf{r}}_2) + \cdots + E_N\phi_N(\vec{\mathbf{r}}_N) \quad (62)$$

$$E\psi = (E_1 + E_2 \cdots + E_N)\psi \quad (63)$$

One can immediately see that the total Energy  $E_N$  of the non interacting system can be described by equation 64.  $E_i$  stands for the energy of the  $i$  th electron in a particular state.

$$E_N = E_1 + E_2 + \cdots + E_N \quad (64)$$

The energy of a system with  $N$  electrons would be  $E_N$ . If the system has  $N-1$  electrons the energy has to be  $E_{N-1}$ . In an photoemission experiment where an electron is emitted from the  $i$  th level the total Energy has to change by  $E_i$  according to equation 65

$$\delta E = E_N - E_{N-1} \quad (65)$$

$\delta E$  is nothing else than the measured binding energy  $E_B$  in an UPS experiment. It also gives the energy of the  $i$  th electron in its particular state assuming non interacting electrons. This is called the frozen orbital approximation. Sadly the electron - electron interaction cannot be neglected. This is going to cause a lot of trouble. The many particle wave function can no longer be described with equation 59 and the total energy is no longer a sum of the single electron energies (equation 65). An answer to this problem is the Hartree Fock theory. Without going into to much detail, single electron energy levels are defined  $E'_i$ , but now they are dependent on all the other electrons. If an electron is emitted a positive hole is left. In an interacting system the electrons are going to rearrange, caused by the change of the potential. The electrons will relax to a many body state of optimal (minimal) total Energy  $E'_{N-1}$ . The Energy difference between the relaxed  $E'_{N-1}$  and the non relaxed state  $E_{N-1}$  is the relaxation energy  $E_R$ . This energy is passed onto the photoelectron. Therefore the measured binding energy is not only the electron energy given by the Hartree Fock theory, it has an additional component  $E_R$ . It might also include a component which originates from shielding of the hole (screening). Equation 66 describes those facts. The previously discussed interactions are called intraatomic interactions.

$$E_B = E'_i - E_R \quad (66)$$

The Hartree Fock Energy  $E'_i$  is an approximation of the binding energy. How good this approximation is depends on the influence of the occupation by other electrons. If this effect is negligibly small Koopmans theorem holds, which results in a binding energy describable by the one electron energy of the Hartree Fock theory. It can also happen that the relaxation process is incomplete. This means that the "relaxed" state is not the ground state of the new  $N - 1$  electron system. It can be an excited state. Collective interactions like phonons and plasmons can appear. The emitted electron is going to get only a part of the relaxation energy and it will be detected at a different binding energy (satellite peak). If a satellite is identified as a satellite then there will be no problem in the evaluation of the spectra. However if one

does not know that it is an satellite it can lead to severe problems. Additional effects occur when an atom or molecule is adsorbed on a solid. One can easily imagine there has to be a difference between a photo excitation on an isolated atom and a photo excitation on an atom adsorbed onto a substrate. The environment is different. The relaxation process involves now atoms which have a chemical bond with a substrate atom. It also involves the surface atoms of the substrate itself. Additional shifts of the emission line will occur. Electrons of neighboring atoms are going to screen the positive core hole. This leads to a interatomic relaxation shift  $E_{interatomic}$ . In a metal  $E_{interatomic}$  is dominated by the screening due to the mobile valence electrons. In case of molecular crystals  $E_{interatomic}$  can be divided into two parts. The first one is  $E_{intramolecular}$  which describes relaxation shifts due to electrons from the molecule itself. Whereas the second part  $E_{extramolecular}$  describes energy shifts due to neighboring molecules. [10, 21]

$$\hbar\omega = E_B + E_K + \phi - E_{intraatomic} - E_{intramolecular} - E_{extramolecular} \quad (67)$$

These effects are the reasons why the energy of Koopmans theorem is never observed in reality.

## 4 Experimental Setup

### 4.1 Siemens D501 Krystalloflex Goniometer

The Siemens D501 Krystalloflex Goniometer is designed for powder diffraction experiments (chapter 3.3.4). It uses Bragg Brentano focusing and has a graphite monochromator at the secondary side. Cu  $K_\alpha$  radiation is used. This measurement system can be seen in more detail in figure 21. The x-ray beam passes two apertures (2), (3) before it hits the sample (4) in the goniometer center under the angle  $\theta$ . The electromagnetic wave gets diffracted from the sample. It has to pass three more apertures (5), (7), (9) and a monochromator (8) at the secondary side before it is able to hit the detector.

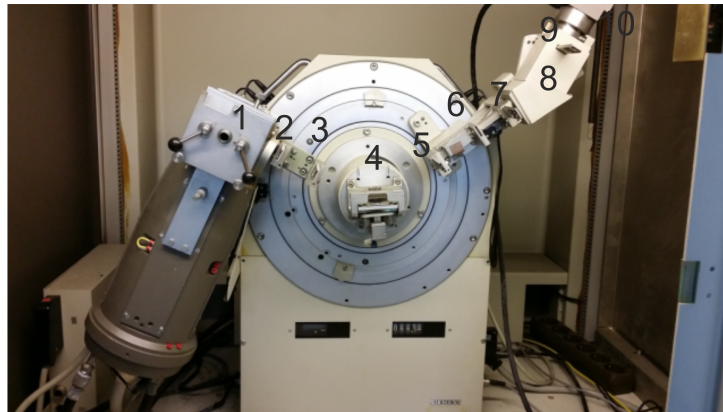


**Figure 21:** Siemens D501 Crystalloflex powder diffractometer. The x-ray tube is on the left side (1). It emits Cu  $K_\alpha$  radiation. (2) and (3) are the positions of the aperture at the primary side. The sample is mounted on (4). (5), (7) and (9) are the aperture at the secondary side. A filter can be used in position (6). The incoming beam from (1) gets diffracted at the sample (4) and passes the monochromator (8) which is in front of the detector (10). The whole systems uses Bragg-Brentano focusing.

### 4.2 Phillips X'Pert four circle Texture Goniometer

The Phillips X'Pert is a multifunctional measurement tool. It provides a couple of different types of scans.

- Specular Scans  $\theta/2\theta$  (chapter 3.3.1)
- Rocking Curves  $\omega$  (chapter 3.3.2)
- Polefigures (chapter 3.3.3)

The combination of these three scans is extremely powerful to determine the present crystalline phase and its epitaxial relationships. The Phillips X'Pert uses an ATC 3 Euler cradle and Bragg Brentano focusing. The radiation emitted by the x-ray tube is Cr  $K_\alpha$ . At the secondary side there is also a graphite monochromator. Figure 22 and 9 show the measurement equipment.

The incoming beam emitted from the source (1) passes the collimator at (2) and illuminates the sample at (3) which is mounted on the sample holder. The beam is diffracted and travels towards the detector

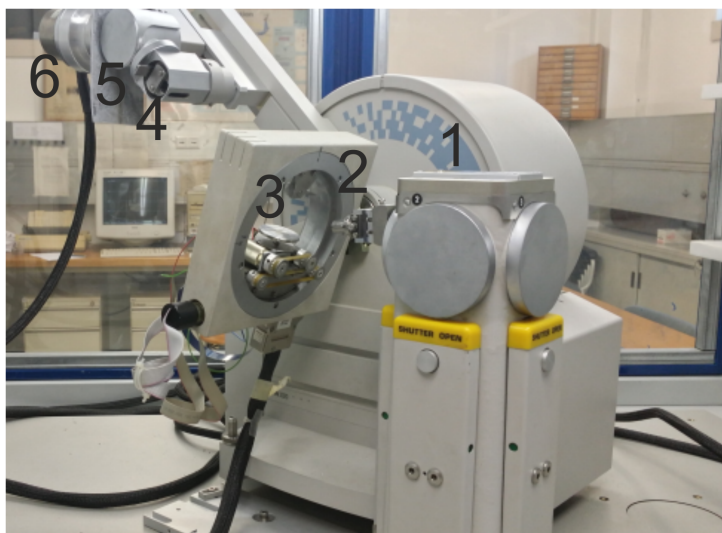


**Figure 22:** Phillips X'Pert four circle texture goniometer. On the primary side is the x-ray tube (1) emitting Cr  $K_{\alpha}$  radiation. (2) is the position of the collimator. The sample is mounted on the holder (3) which is able to rotate in three directions. The aperture on the secondary side is placed on (4), (5) is the monochromator and (6) is the detector.

at (6), passing the secondary aperture (4) and the monochromator (5).

### 4.3 UHV System: ADES 400 Spectrometer

The ADES 400 Spectrometer is a UHV System with a base pressure in the low  $10^{-10}$  mbar regime. To achieve pressures like that a combination of rotary pumps and liquid nitrogen cooled oil diffusion pumps is used. Main measurement tools in the ADES are:

- Angle resolved ultraviolet photoemission spectrometer ARUPS
- Auger electron spectroscopy
- Microbalance (quartz crystal) for deposition rate measurements

Thermocouple connections can be used to measure the substrate temperature. Additionally the sample is mounted on a manipulator with a rotatable head. This means the sample can be moved in the X,Y, and Z direction and can be rotated around the vertical axis. Due to the use of a wobble stick it can also be rotated along the azimuthal direction. Different types of evaporators were used during this work (triple evaporator and dual evaporator). For heating experiments and for the cleaning procedure direct heating and indirect heating of the substrate is possible. Of course there also exists a sputter gun and a mass spectrometer. Figure 23 shows a schematic of the ADES system. It gives a good overview of the the whole vacuum system. A side view of the ADES can be seen in figure 24. All important components are marked and named. The sample preparation is done in the upper region of the UHV chamber. This includes sputtering, evaporation of molecules onto the substrate surface, measurements of the deposition rate and the rotation of the substrate azimuth. The LEED optics is also placed in the upper region of the chamber. It is on the opposing side of the big window seen in figure 23. Ultraviolet photoemission spectroscopy (UPS) and Auger spectroscopy have to be performed in the bottom of the chamber. That is where the analyzer is placed. A helium discharge lamp is used as a light source. The

obtained light is unpolarized and has a energy of about 21.2eV. Which corresponds to the  $\alpha$ -I transition of Helium.



A close look at the manipulator head is given in figure 25.

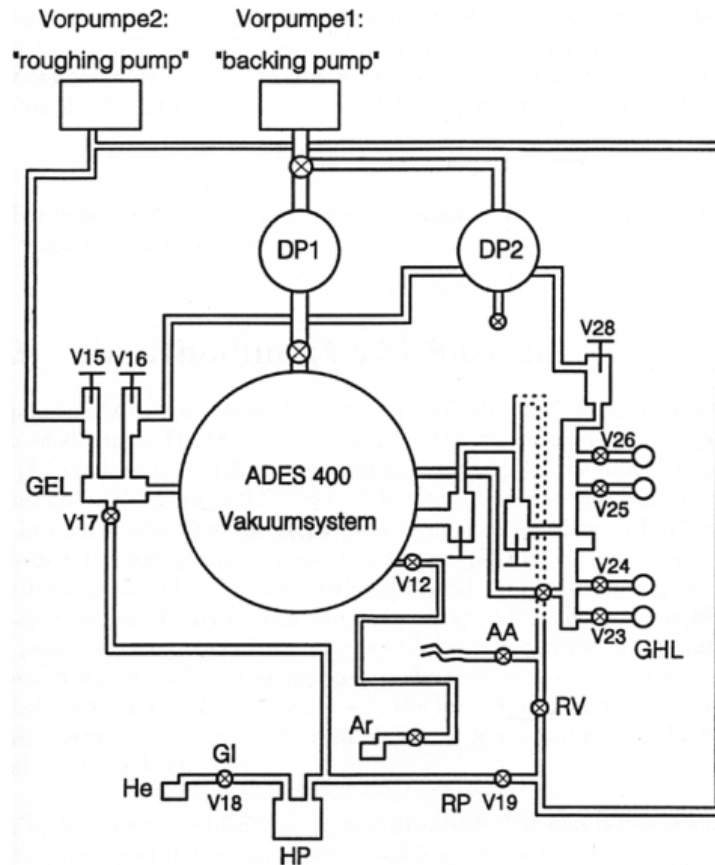


**Figure 23:** Schematic of the ADES 400 Spectrometer: DP... diffusion pump, V... valve, GEL... gas discharge lamp, AA... air admit, GHL... gas handling line, Gl... gas inlet (for HE lamp), HP... helium purifier, Ar... argon inlet, RV... roughing valve, RP... roughing purifier [28]

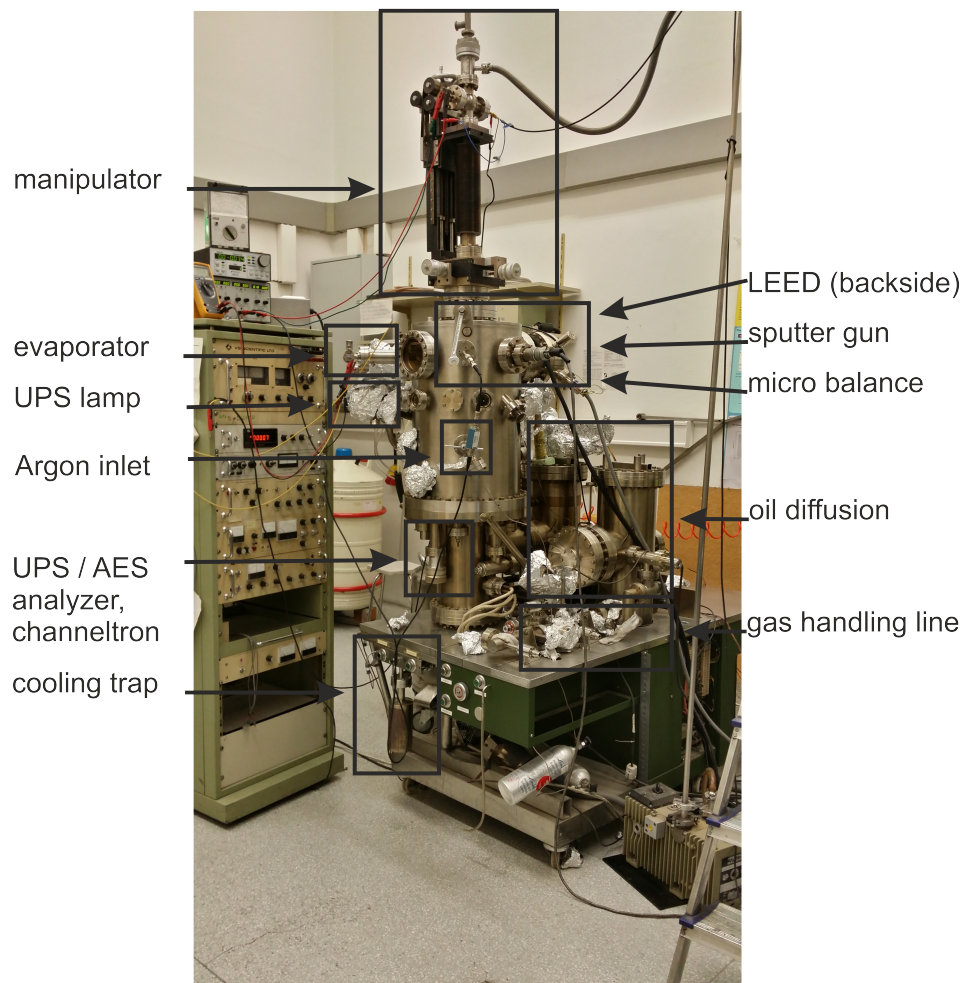


*Figure 24:* Side view of the ADES 400 Spectrometer

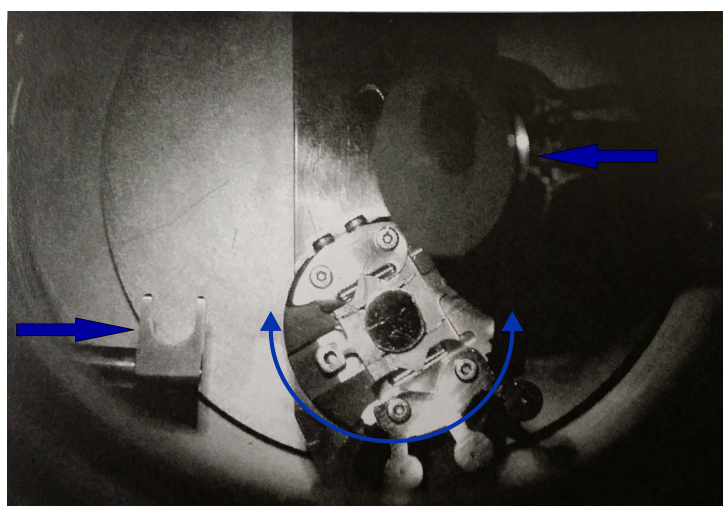


*Figure 25:* Manipulator head with a mounted crystal in the center. The handle bars are for the wobble stick to rotate the azimuth of the sample. The wobble stick can be seen on the left side and the microbalance on the right side. The shutter for the LEED optic can be seen in the background.[28]

## 5 Materials

### 5.1 Cu(110) and Cu(110)-(2x1)O

Copper is a transition metal with a very good thermal and electrical conductivity. Its electronic configuration is  $[Ar]3d^{10}4s^1$ . Copper crystallizes as a face centered cubic (fcc) lattice with a lattice constant a 3.6077 Å. In this work a copper(110) single crystal was used as an atomically controlled template for the growth of the molecules. Figure 26 shows the fcc lattice of copper. The surface of the crystal is illustrated in figure 27. One can immediately see its two fold rotational symmetry. The atomic rows are along the  $[1\bar{1}0]$  direction with a lattice constant of 2.55 Å (short axis). The long axis (in the  $[001]$  directions) has a length of 3.6 Å. The unit cell of the 110 surface is marked red and has dimensions of  $(3.6 \cdot 5.1) \text{ \AA}^2$  (figure 26) .

**Table 4:** Crystalline structure parameters of Cu(110) and important parameters.[3, 6, 24]

Parameters	Value / Structure
a [Å]	3.6077
b [Å]	3.6077
c [Å]	3.6077
$\alpha$ [°]	90
$\beta$ [°]	90
$\gamma$ [°]	90
Melting point	1084.62
Bravais lattice	fcc
Workfunction [eV]	4.4eV

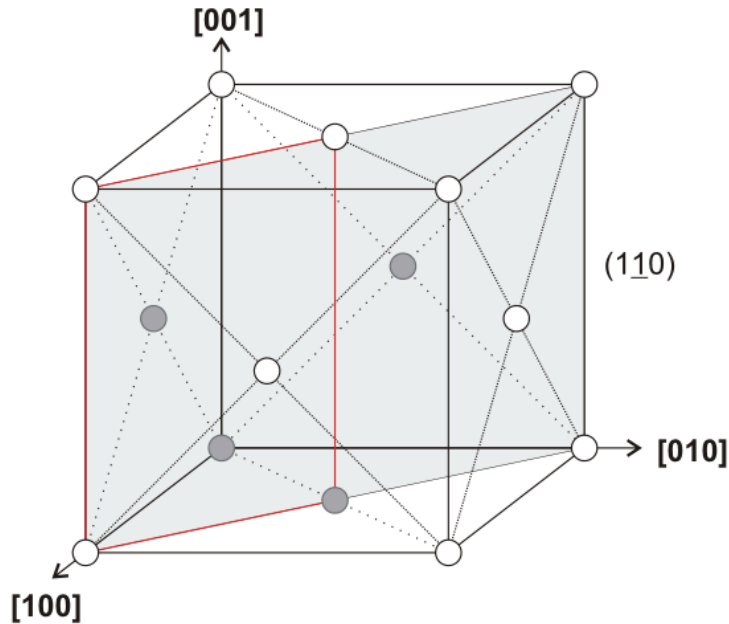


**Figure 26:** Face centered cubic lattice of copper [6]. The plane indicated in gray is the (110) plane.

Creating the Cu(110)-(2x1)O reconstruction is a straight forward procedure. The obtained structure can be seen in figure 27. One immediately notices the change in corrugation. The atomic rows are now in the  $[001]$  direction. The gray atoms are the copper atoms and the black ones are the oxygen atoms. There is always one lattice vector from gray to gray and black to black in the  $[001]$  direction. It's length is 3.6 Å.

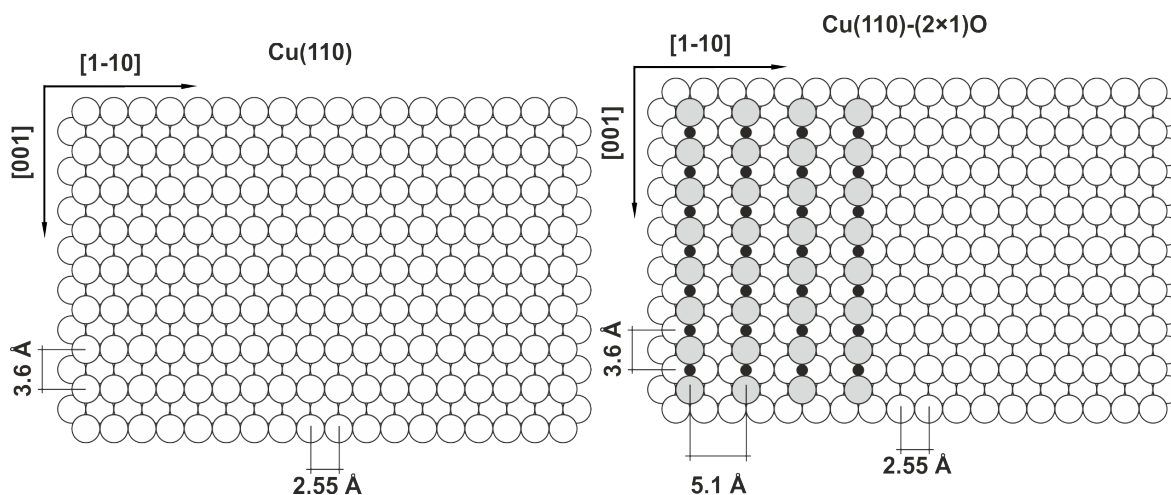


**Figure 27:** A clean Cu(110) surface is shown on the left side. The right side shows a partial Cu(110)-(2x1)O reconstruction. The grey atoms are copper atoms and the black dots are the oxygen atoms.

The repeating unit of the  $[1\bar{1}0]$  is two lattice vectors long and the distance in total is 5.1 Å. The copper atoms (gray) sit on hollow positions (between the copper atoms of the layer below) whereas the oxygen atoms sit on top positions (on top of two neighboring copper atoms).

### 5.1.1 Creating the Cu(110)-(2x1)O reconstruction

A clean Cu(110) template is necessary for the creation of a Cu(2x1)O reconstruction. The copper crystal is still on temperature after the last annealing process. (sample cleaning is described in section 5.1.2)

An exposure of roughly 50 Langmuir oxygen at about 150 °C will create a complete Cu(110)-(2x1)O reconstruction of the surface. This means half a monolayer of oxygen is on the copper(110) surface and it changed it in a way where also copper atoms are in the oxygen rows. That's why it is called reconstruction. Otherwise it would just be normal adsorption.

1 Langmuir correspond to a pressure of  $1.33 \cdot 10^{-6}$  mbar · s. Accordingly to that an exposure of 48 L would lead to a pressure of  $4 \cdot 10^{-7}$  mbar over 180 s. Oxygen is released into the chamber until the desired system pressure is reached. The reconstruction should be finished after the correct amount of time.

The most important thing about the Cu(110) and the Cu(110)-(2x1)O reconstruction is that they are both atomically controlled surfaces. A clear surface reconstruction is of crucial importance for the alignment of the molecules.

### 5.1.2 Substrate Cleaning

To clean a crystal in UHV one starts by flashing it. This means heating the substrate quickly up to a rather high temperature, but below the melting point. The flashing process is stopped at 23mV thermocouple

voltage, which corresponds to 595 °C. Since the reference of the thermocouple is the room temperature and therefore 0 mV correspond to room temperature. As a consequence of flashing most of the "dirt" on the surface will desorb. Some dirt will still stick to the surface and some dirt will move inside the bulk of the crystal. The next steps in the cleaning procedure are repeated cycles of sputtering and annealing. In the case of a copper(110) crystal three to four cycles are usually sufficient. Sputtering is the bombardment of a surface with noble gas ions under a certain angle with a specific acceleration voltage. The copper substrate was sputtered for 15 minutes with a system pressure of  $10^{-4}$  mbar. An acceleration voltage of 1 kV was used for the argon ions. The filament current of the argon gun was run with 25 mA. Annealing is the following heat treatment. The copper atoms are given thermal energy to rearrange. What essentially lets the crystal "heal". The copper crystal was annealed between 21 mV and 22 mV which corresponds to a temperature between 545 °C and 570 °C. Two minutes and 30 seconds seemed to be a reasonable annealing time. The cleanliness of the substrate can be checked with low energy electron diffraction (LEED) and UPS measurements of the workfunction. In this study the workfunction was checked via UPS measurements. Clean copper has a workfunction of about 4.4 eV.

## 5.2 Quinacridone

Quinacridone is an organic pigment and it is used for colors between red and violet. Its chemical formula is  $C_{20}H_{12}N_2O_2$  and it is listed as C.I. pigment violet 19 (C.I....color Index). With a total production volume of several thousands tons a year it is the most important pigment in this range.

Figure 1 shows pentacene on the left side and on the right side its hydrogen bonding analogon Quinacridone. Both molecules are organic molecules. They look very similar shape wise. Quinacridone has a length of 16.1 Å and its broadest part is 7.8 Å wide. All distances include the van der waals radi of the outer atoms. Pentacene has five benzene rings with fully spread out  $\pi$ -orbitals. Quinacridone has only three benzene rings and two modified benzene rings. The major difference are the two nitrogen atoms and the two oxygen atoms of Quinacridone. These two types of atoms have a crucial influence on the molecule itself. First of all one expects the intermolecular  $\pi$ -conjugation to be broken. Additionally nitrogen and oxygen are both highly electronegative (N...3.04, O... 3.44, Pauling scale). Usually organic molecules form van der Waals crystals. In this special case there is an additional attractive force originating from the hydrogen bonds. They are going to play a significant role in the crystal formation as well as in the stability of the molecular crystals. That is one of the main reasons of interest for Quinacridone. It is not so much about Quinacridone itself. It is more the hydrogen bonding which attracts a lot of attention. Another reason are the three well defined crystalline structures of Quinacridone (5Q). The crystallographic data for the three phases are given in table 5. To clear up possible confusions, the phases are labeled  $\alpha$ ,  $\beta$  and  $\gamma$ .

### 5.2.1 $\alpha$ phase

The  $\alpha$  phase of Quinacridone has only one molecule per unit cell. Its lattice parameters and the corresponding angles are given in table 5. Every molecule forms four hydrogen bonds with its neighboring molecules. The final bonds have the form  $N - H \dots O = C$  ([23]). It builds chains of molecules linked by hydrogen bonds. This can be seen in a front view in figure 29. The blue dotted line indicates a hydrogen bond. One can also see that neighboring molecules are slightly offset. Every molecule has the same direction of the long molecular axis. Lattice energy calculation showed that these steps are not

**Table 5:** The three well known crystalline structures of Quinacridone, namely the  $\alpha$ ,  $\beta$  and  $\gamma$  phase. a, b, and c are the length of the unit cell vectors and the corresponding angle are  $\alpha$ ,  $\beta$  and  $\gamma$ . Z is the amount of molecules in the unit cell.[9]

Crystal phase	$\alpha$	$\beta$	$\gamma$
Space group	$P\bar{1}$	$P2_1/c$	$P2_1/c$
Z	1	2	2
Unit cell dimensions			
a [ $\text{\AA}$ ]	3.802	5.692	13.697
b [ $\text{\AA}$ ]	6.612	3.975	3.881
c [ $\text{\AA}$ ]	14.485	30.02	13.4020
$\alpha$ [ $^\circ$ ]	100.68	90	90
$\beta$ [ $^\circ$ ]	94.40	96.76	100.44
$\gamma$ [ $^\circ$ ]	102.11	90	90
Volume [ $\frac{V}{\text{\AA}^3}$ ]	346.7	674.5	700.6

some kind of interaction in the chain, they are stacking effects. They occur due to the stacking in the "a" direction [23]. Figure 28 shows a top view of the  $(1\bar{1}2)$  plane. One essentially sees the top of three stacks of chains. In a stack every chain is parallel to the others. The stacking occurs purely due to van der Waals forces.

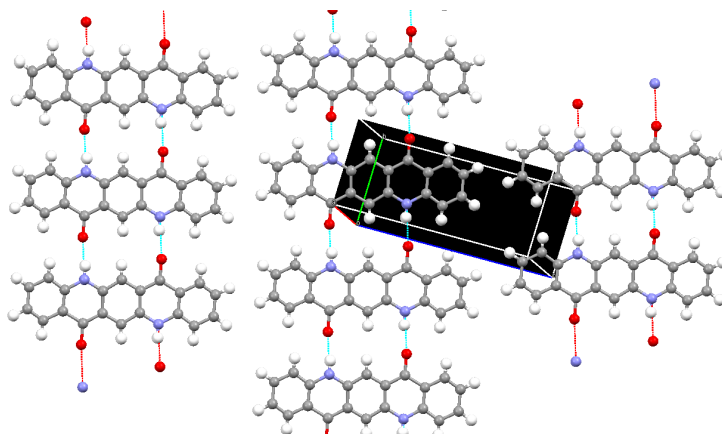


**Figure 28:** Model of the  $\alpha$  phase of Quinacridone with a view in the  $[1\bar{1}2]$  direction.

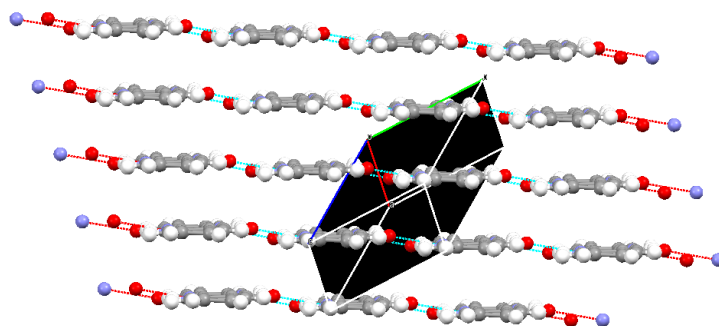


**Figure 29:** Model of the  $\alpha$  phase of Quinacridone with a view along the long molecular axis.

### 5.2.2 $\beta$ phase

The  $\beta$  phase consists of two molecules per unit cell and has the same hydrogen bonding pattern as the  $\alpha$  phase. Four bonds of the same type are made and every molecule is connected to two neighboring molecules with two bonds (figure 30 and 31, the blue and red dotted lines). Therefore it builds also chains. However there is one major difference. The  $\beta$  phase has two different orientations of the final chain stacks. Half of the chains run roughly in the  $[110]$  direction and half of the chains run approximately in the  $[1\bar{1}0]$  direction([23]). Whereas in the alpha phase there is only one orientation and all chains are parallel to each other. The chains in the stacks are again parallel to the others, but the two different stacks have a slightly different direction of the long molecular axis. Figure 30 and figure 31 show this behavior. Additionally it should be mentioned that the chains themselves are not 100% planar. The steps of the  $\beta$  phase are similar to the steps of the  $\alpha$  phase. They have a width of  $0.35 \text{ \AA}$  and are a result of stacking effects ([23]).

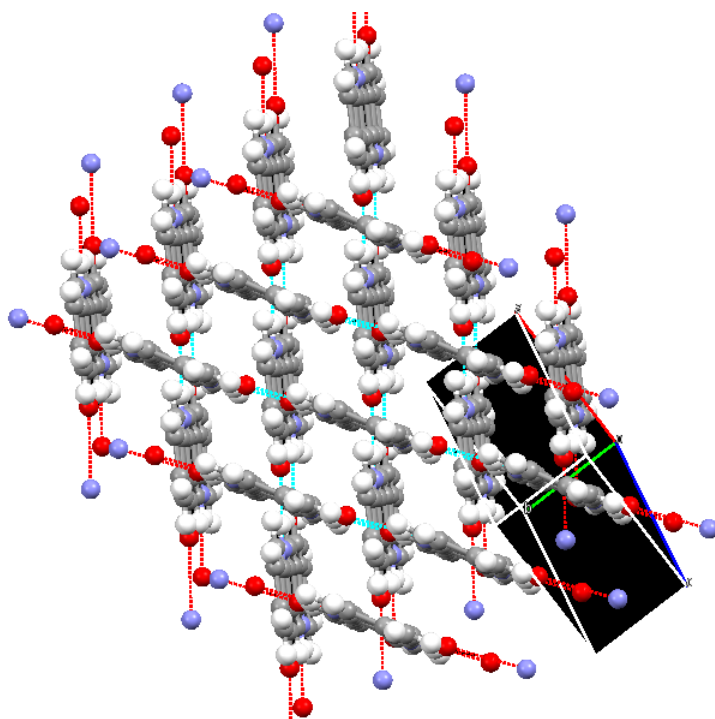


*Figure 30:* Model of the  $\beta$  phase of Quinacridone with a view close to the long molecular axis.

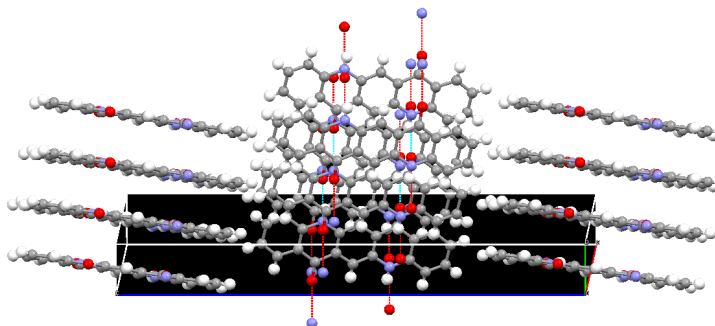


*Figure 31:* Model of the  $\beta$  phase of Quinacridone with a view parallel to the  $c$  axis.

### 5.2.3 $\gamma$ phase

The last crystal structure is the  $\gamma$  phase and its packing is quite different compared to the other two phases. Every molecule is connected to four different neighboring molecules via hydrogen bonds (figure 32). Since Quinacridone can only make four hydrogen bonds per molecule, it is now connected with one hydrogen bond for each neighbor. The chain building is no more approximately planar, as in the  $\alpha$  and  $\beta$  phase. The result is a criss cross pattern with parallel stacks of molecules in two different directions. Figure 33 shows a view in the direction of the c axis of the real space lattice. It gives a clear view of the resulting criss cross pattern and the parallel stacks. There essentially are two different directions of long molecular axis. It is also important to mention that there are two molecules in the unit cell.

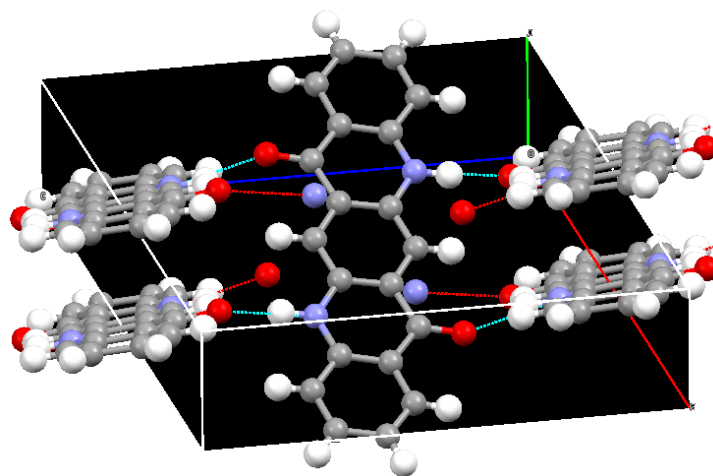


*Figure 32:* Model of the  $\gamma$  phase of Quinacridone with a view along the long molecular axis.

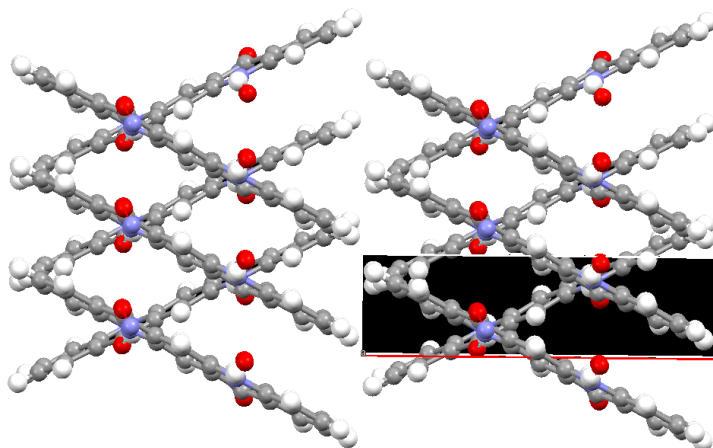


*Figure 33:* Model of the  $\gamma$  phase of Quinacridone with a view along the c axis. The horizontal axis is the a axis and the vertical axis is the b axis.

## 6 Experiments and Results

### 6.1 Powder Diffraction

Quinacridone is reddish as a powder. The very first experiment was a  $\theta/2\theta$  scan conducted on the Siemens D501 Krystalloflex powder diffractometer. The Quinacridone powder itself is chunky. Crushing the powder in a mortar before performing a measurement is essential. Once the powder is fine enough the experiment can be carried out. The Experimental parameters (acceleration voltage, slits,...) are given in table 6.

**Table 6:** Experimental parameters of the Siemens D501 Krystalloflex for the powder measurement of Quinacridone.

Parameters [units]	Value
Acceleration Voltage [kV]	40
Current [mA]	30
Cu $K_\alpha$ [ $\text{\AA}$ ]	1.54
Cu $K_\beta$ [ $\text{\AA}$ ]	1.39
aperture 1 [ $^\circ$ ]	1
aperture 2 [ $^\circ$ ]	1
aperture 3 [ $^\circ$ ]	1
aperture 4 [ $^\circ$ ]	0.15

Figure 34 represents the measured diffraction pattern of the powder sample. The vertical axis stands for the counts obtained at the detector after acquiring for a specific time (dwell time) at an specific scattering angle  $2\theta$ .

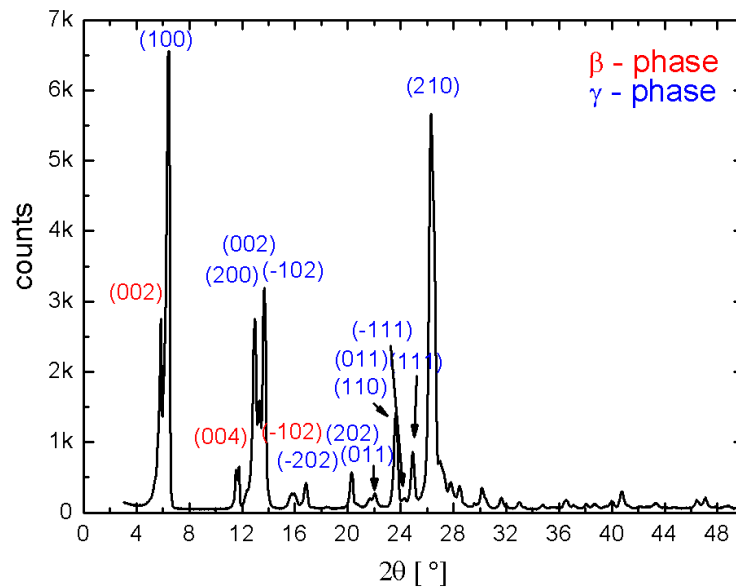


**Figure 34:**  $\theta/2\theta$  scan of the finely grinded Quinacridone powder

Red stands for contributions from the  $\beta$  phase to the detected signal and blue takes the  $\gamma$  phase into account.

The presence of an  $\alpha$  phase cannot be completely excluded because, the assignment of peaks is not straight forward. The diffraction patterns of the three phases look quite similar and additional experimental peak shifts are present. They appear due to the fact that the Quinacridone powder does not have a high electron density and that the primary radiation penetrates deeper inside the specimen. This radiation is no longer diffracted at the center of the goniometer circle and as a consequence peak shifts to lower  $2\theta$  angles occur. These shifts are a function of  $2\theta$  and their influence is going to be stronger at lower angles. These circumstances are displayed in figure 35.

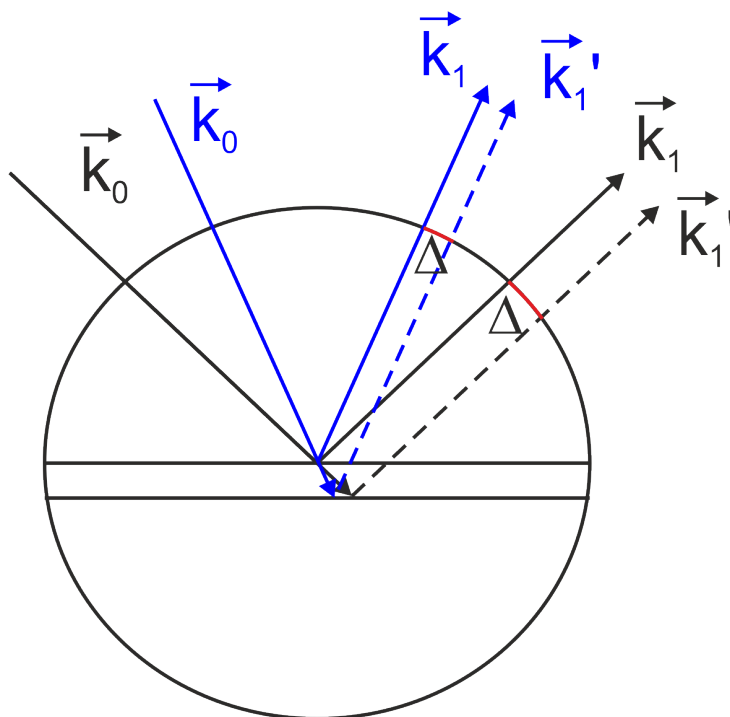


**Figure 35:** Geometrical interpretation of the peak shift. The circle illustrates the goniometer circle. The colors black and blue stand for different angles of incidence.  $\vec{k}_0$  is the incoming wave vector which is diffracted once at the center of the goniometer circle into the wave  $\vec{k}_1$  and once deeper inside the sample into  $\vec{k}_1'$ . The red parts along the circumference stand for the difference in the angle of detection (peak shift). Additionally the angular dependence of the peak shift can be seen.

Figures 36, 37 and 38 compare the measurement with calculated powder patterns of the software Powder Cell. The detected signal has to be a superposition of the different phases. No single phase is able to reproduce the pattern completely. Figure 37 is a strong indicator for the presence of a  $\beta$  phase in the powder. Every indexed peak matches a measured peak or is at least very close to a measured peak. The  $\gamma$  phase is the phase which is most similar to the measured pattern (37). From inspection by eye one immediately notices the dominance of this phase in the diffraction pattern. If peak shifts are considered, it can be concluded that the  $\beta$  and  $\gamma$  are phase present. The  $\alpha$  phase is illustrated in figure 38. It is the least similar phase comparing the diffraction patterns, but it still has a lot in common with the measurement. Close to every  $\alpha$  peak there is either a peak from  $\gamma$  or  $\beta$  phase and as a consequence of that it is not easy to say that the  $\alpha$  phase is present or can be excluded. The refinement tool can be used for a very rough quantitative phase analysis of the measured pattern. The fitting of the three phases to the measurement leads to a presence of the  $\gamma$ -phase with 86%. The  $\beta$  phase contributes with 10% and the  $\alpha$  phase with 4% (without knowledge about the error). Usually refinement is used to determine the crystal structure for a specific diffraction pattern. The starting point was the crystallographic data for Quinacridones well known three phases. After refinement the same structure was obtained as in the

exactly solved structure. It added a background, a zero shift, and fitted the calculated pattern to the measured one. Regardless of the accuracy it is a strong indicator that all three phases are present and it is in agreement with the inspection by eye which stated that the  $\gamma$  phase is the dominant phase. The second most dominant is the  $\beta$  phase and the weakest one if present is the  $\alpha$  phase.

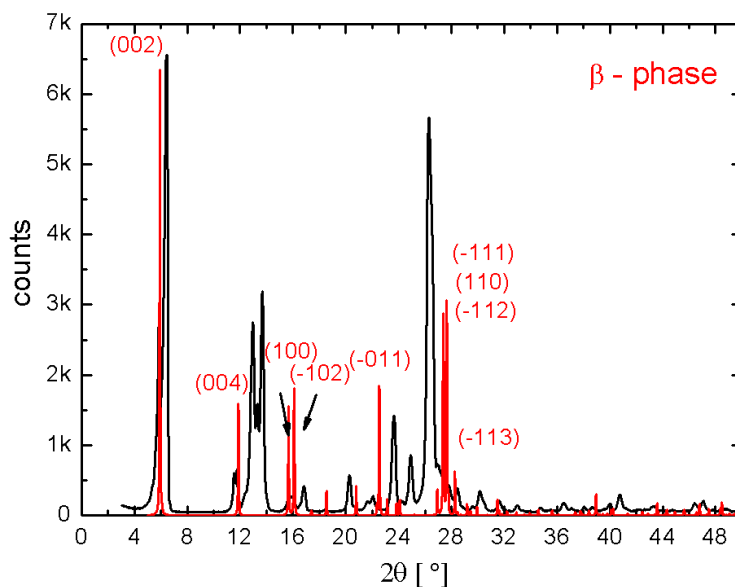


**Figure 36:**  $\theta/2\theta$  scan of finely grinded Quinacridone powder. The black line is the experimental scan and the red line stands for a theoretical calculation of the  $\beta$  phase.

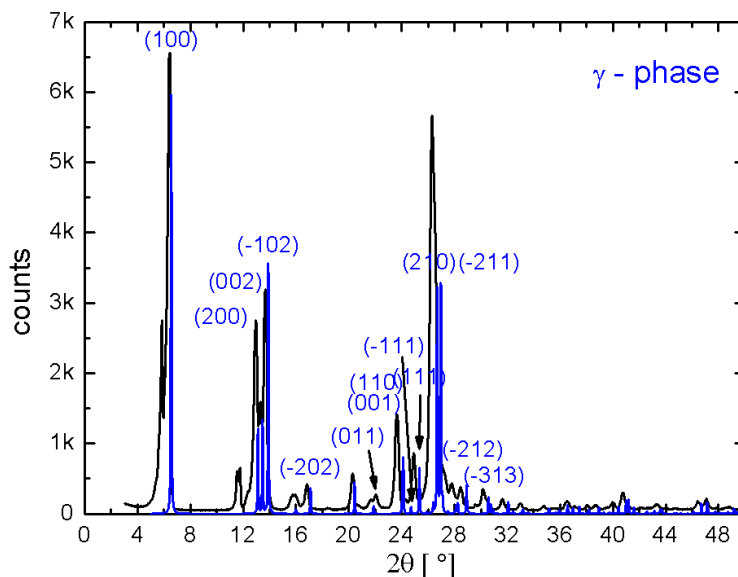


**Figure 37:**  $\theta/2\theta$  scan of finely grinded Quinacridone powder. The black line is the experimental scan and the blue line stands for a theoretical calculation of the  $\gamma$  phase.

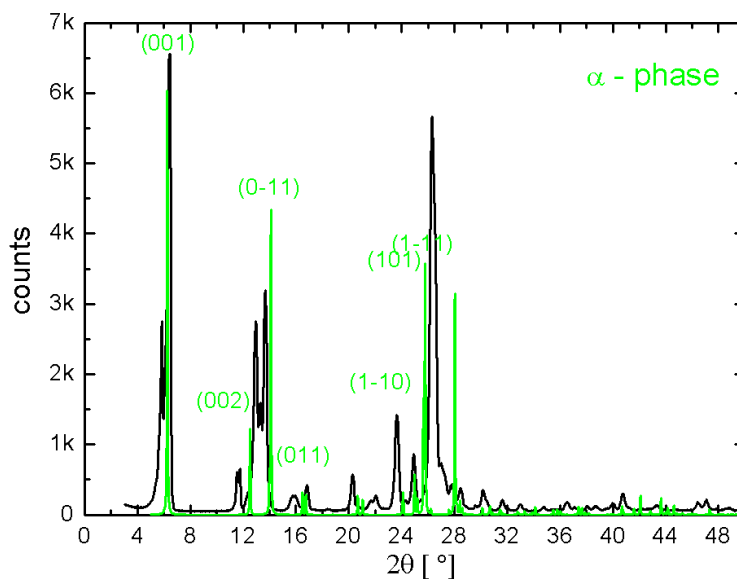


**Figure 38:**  $\theta/2\theta$  scan of finely grinded Quinacridone powder. The black line is the experimental scan and the green line stands for a theoretical calculation of the  $\alpha$  phase.

## 6.2 "Thick" Film Samples

This section treats films produced for x-ray diffraction experiments. The following three samples have a thickness between 20 and 30 nanometers. They were investigated by the measurement techniques described in chapter 3.3 (specular scans, rocking curves and polefigures). Every sample was measured with the Phillips X'Pert four circle texture goniometer. Additionally some UPS data is going to be presented.

### 6.2.1 Sample 1, Quinacridone on Cu(110) at $T_S$ 25 °C

**Sample preparation** This sample was prepared on the ADES 400 spectrometer (described in section 4.3) under UHV conditions. The substrate was cleaned by three cycles of sputtering and annealing. The cleaning parameters can be seen in table 7. From the knowledge of later samples, the flash and annealing temperatures should be higher. Unlike the following two samples, this thick film was produced in steps. At first a monolayer was evaporated onto the substrate surface. The evaporation rate was measured with a micro balance and turned out to be 0.035 Å/s. It took 40 minutes for the evaporator to obtain a stable rate. The whole evaporation lasted 100 seconds, leading to a film thickness of 3.5 Å. Afterwards an ultraviolet photoemission spectroscopy measurement was performed. Subsequently the film was heated up to 250 °C and was measured again. Once the sample cooled off a film of 23.3 Å thickness was evaporated on top, and UPS measurements were carried out again. The workfunction did not change from the monolayer to the multilayer. This means the first evaporation covered the hole substrate surface. The last evaporation was performed in a time window of 130 minutes with a rate of 0.032 Å/s, resulting in a thickness of 246.8 Å. The total thickness of the film is  $3.5 + 23.3 + 246.8 = 273.9$  Å (27.4 nm). This film was used for the following x-ray diffraction experiments. The substrate was always at room temperature during the film growth processes.

**Table 7:** Sample 1 : cleaning parameters of the substrate prior to preparation of the Quinacridone film. In the case of flashing or annealing voltage stands for the filament heating voltage and the current corresponds to the filament current. Temperature is the sample temperature and high voltage is the applied high voltage to accelerate the electrons from the heating filament towards the sample. In the case of a sputtering process current stands for the filament current and the high voltage is the acceleration voltage for argon ions.

Process	Voltage	Current	Pressure $P_s(0.1mA)$	Temperature	High Voltage Settings	Current	Time
Flash	5.4 V	1.65 A		445 °C	650 V	22 mA	
Sputter	1k V	25 mA	$10^{-4}$ mbar				15 min
Anneal	5.4 V	1.66 A		585 °C	550 V	42 mA	3 min
Sputter	1k V	25 mA	$10^{-4}$ mbar				15 min
Anneal	5.4 V	1.66 A		487 °C	250 V	51 mA	3 min
Sputter	1k V	25 mA	$10^{-4}$ mbar				15 min
Anneal	5.4 V	1.65 A		445 °C	185 V	48 mA	5 min

**XRD Measurements** The experimental parameters for the following measurements can be seen in table 8. A collimator with a 1 millimeter width and 4 millimeter height was used on the primary side. In front of the detector was an aperture with 1.2mm and the small beam mask (secondary side). The sample alignment in the Philips is straight forward. There is a rockable needle and its tip points exactly at the goniometer center. The sample surface has to be aligned exactly to the end of the tip without getting damaged. If the sample is to low peak shifts to lower angles occur.

**Table 8:** Experimental parameters for the x-ray diffraction measurements of a 27.4 nm thick film of Quinacridone on a Cu(110) substrate using the Phillips X'Pert four circle Texture Goniometer. The collimator defines the aperture at the side of the x-ray source and detector aperture specifies the aperture on the detector side, followed by the beam mask.

Parameters [units]	Value
Acceleration Voltage [kV]	40
Current [mA]	30
Cr $K_\alpha$ [ $\text{\AA}$ ]	2.29
Cr $K_\beta$ [ $\text{\AA}$ ]	2.08
Collimator [mm]	1x4
Beam mask	small
Detector aperture [mm]	1.2

**Specular Scan  $\theta/2\theta$**  Specular scans are mostly used for the identification of the present crystalline phases, assuming one knows the material under investigation. Figure 39 shows the  $\theta/2\theta$  scan of the Quinacridone film described above. The counts are plotted on the vertical axis and the horizontal axis shows the diffraction angle  $2\theta$ . A peak arises at an angle of  $41.1^\circ$  and it has a maximum value of 15 counts. Despite low intensity the peak could be clearly distinguished from the background. Calculations for the diffraction pattern had to be performed. The measurement was compared to these calculations. They give the necessary information about the  $2\theta$  positions of all the peaks of the different phases and also their relative intensity. Only one of the three phases has noticeable peaks in the area around  $41.1^\circ$ . Table 9 shows the three relevant peaks of the  $\beta$  phase. By using of a polefigure from later on the (-112) plane could be identified as the one responsible for the diffraction peak. The difference in the measured peak position and the calculated peak position via Powder Cell for the (-112) plane is  $0.52^\circ$ .

**Table 9:** Relevant peaks of the  $\beta$  phase close to the experimentally observed peak at  $41.1^\circ$  of a 27.4 nm thick film of Quinacridone on a Cu(110) substrate (sample 1).

hkl	$2\theta [^\circ]$	$d_{hkl} [\text{\AA}]$	peak shift $[^\circ]$
-111	41.171	3.256	0.071
110	41.233	3.251	0.133
-112	41.620	3.222	0.520

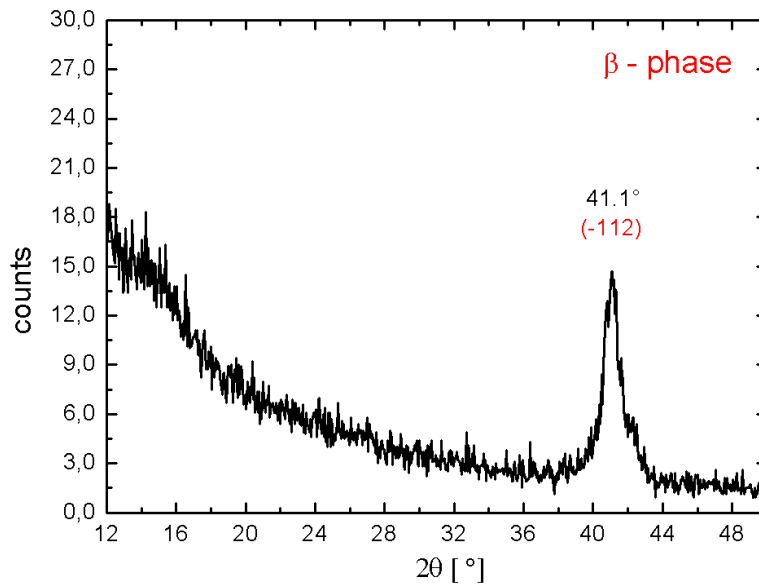


**Figure 39:**  $\theta/2\theta$  scan of a 27.4 nm thick film of Quinacridone on a Cu(110) surface (sample 1). The peak at  $41.1^\circ$  is from the  $\beta$  phase and originates in the (-112) plane.

**Rocking Curve** A rocking curve probes the spatial distribution of the crystallites. Figure 40 shows a rocking curve around the (-112) peak found in the specular scan. It has a Full Width at Half Maximum of  $6.7^\circ$ . Which means that there is wide spatial disorder. The vertical axis displays the counts whereas  $\omega$  is plotted on the horizontal axis.  $\omega$  is nothing else than the incident angle  $\theta$  of the radiation. The (-112) peak should be centered at  $\frac{2\theta}{2}$ , however it is shifted by  $1^\circ$  to an angular position of  $21.5^\circ$ . The shift in the peak position comes simply from sample alignment. There will always be a shift away from ideal values if the sample is not perfectly aligned, which is not that easy to do.

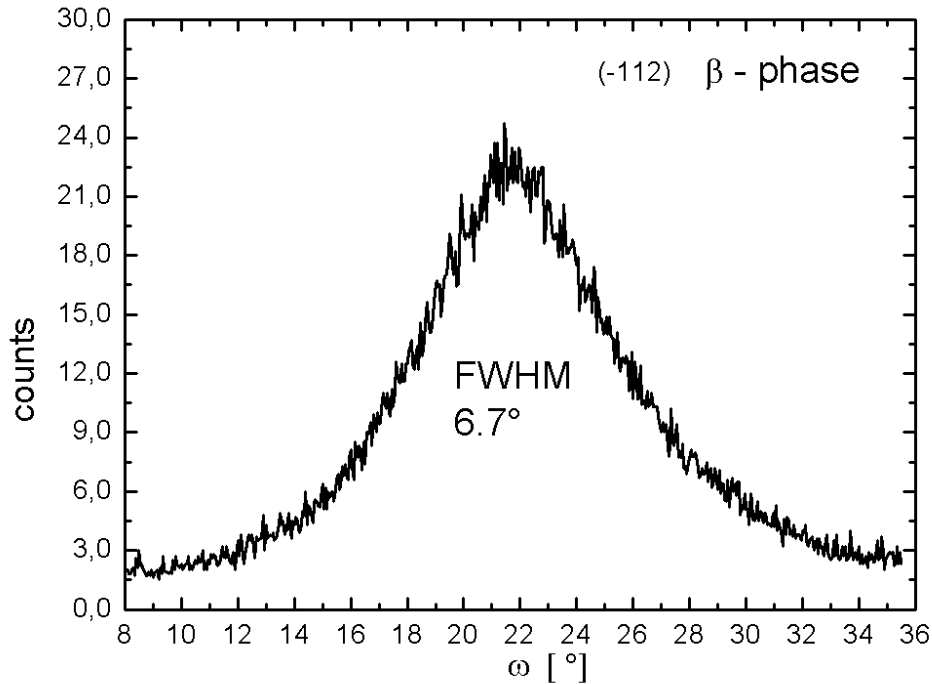


**Figure 40:**  $\omega$  scan of the (-112) peak ( $2\theta$   $41.1^\circ$ ) from a 27.4 nm thick film of Quinacridone on a Cu(110) surface (sample 1).

**Pole Figures** A series of polefigure measurements was performed around the major peaks of all three phases. The peak positions were determined by Powder Cell via powder diffraction calculations. Only one polefigure contained information about the present phase on the sample ( $2\theta = 41.57^\circ$ ). Additionally a polefigure measurement around the copper(111) peak was carried out to determine the substrate directions. The program stereopole [27] was used to evaluate polefigures. Figure 41 shows a polefigure measurement around the angle  $2\theta = 41.57^\circ$ . Different colors denote different stereographic projections calculated by stereopole. All colors except red are from the  $\beta$  phase. It is the only phase that was able to reproduce this pattern. The red color corresponds to copper(110) where [001] and [1-10] are the inplane directions. The copper(111) and (11-1) spots could be matched to the measurement. They orientate the substrate unambiguously. Usually the polefigure around the copper (110) peak is used to orient the substrate. Since all pole figures are measured in a row it is valid to orient the substrate in this polefigure and use this orientation of copper for all the other polefigures around the Quinacridone peaks. This is valid because the mounting of the sample was not changed during the subsequent polefigure measurements. There are some copper spots visible in the case of the polefigure around the (-112) peak ( $41.57^\circ$ ) of Quinacridone and they can be used to orientate the substrate. This leads to the same result as the procedure described above. Additionally the (001), (1-10) directions and its mirrors were introduced to make the substrate directions visible. The enhanced pole densities in the center of the polefigure agrees

with the measurement. All outer spots of the different beta phases ( (-10-20) and (1 0 20)) are artificially introduced and describe the direction of the long molecular axis of a single Quinacridone molecule in the  $\beta$  phase. They all lie close to the outer circle of the polefigure, which corresponds to a tilt of roughly  $90^\circ$  with respect to the measured plane. That leads to molecules which are nearly flat with respect to the surface. The directions of the long molecular axis were determined via the program Powder Cell where it is possible to set the view along a specific direction. If a single molecule was isolated from the structure the direction of the long molecular axis could be determined by guessing the hkl values for the view. Once the correct set of values was guessed the view was right along the direction of the long molecular axis. Since the long molecular axis of the tilted and the non tilted molecule are nearly the same only the one of the flat molecules was used for the polefigure. This polefigure clearly shows four domains of  $\beta$  phase Quinacridone. It is possible to determine the angle between the direction of the long molecular axis of Quinacridone and the substrate directions simply by measuring the angle difference in the polefigure via stereopole. The definition for the sign of the angle is given in figure 42.

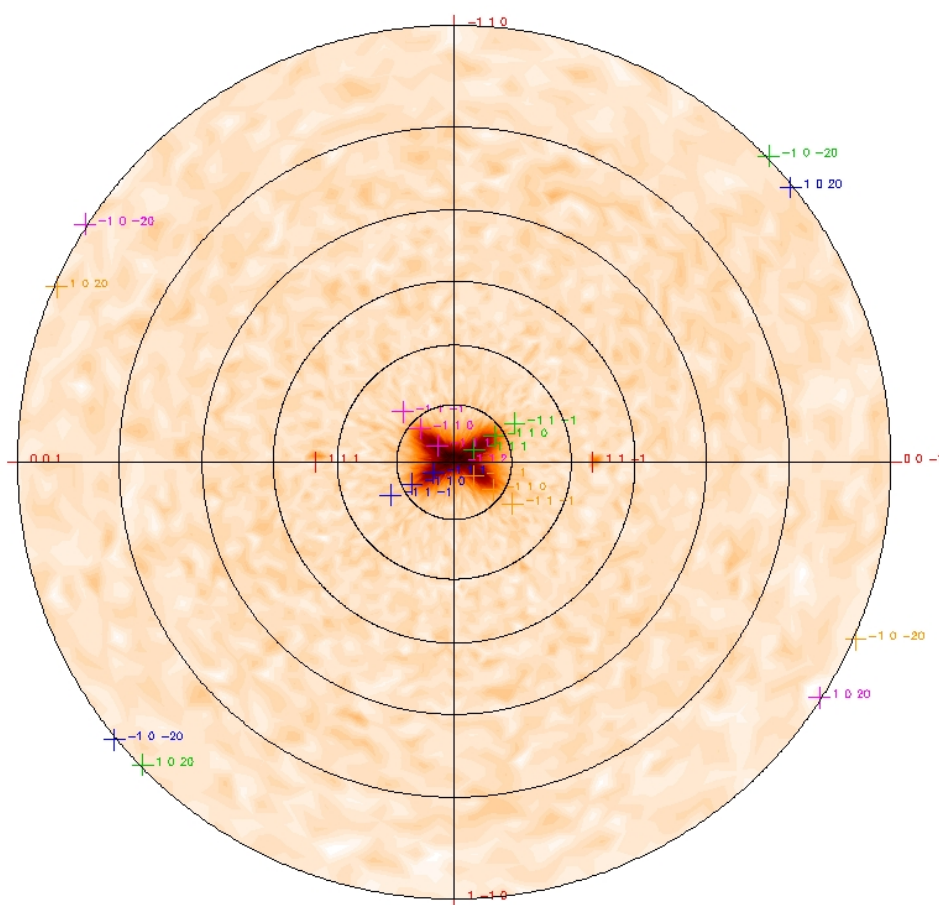


**Figure 41:** Polefigure measured at  $2\theta = 41.57^\circ$  on a 27.4nm thick film of Quinacridone on a Cu(110) surface (sample 1). Different colors denote different crystallite orientations for the  $\beta$  phase, except red. Red crosses represent the copper substrate and its directions. The numbers are the hkl indices of the planes. The stereogram was calculated with the  $\beta$  phase and the  $\{-112\}$  family of planes parallel to the Cu(110) surface.

**Models** A top view of the (-112) plane of the  $\beta$  phase can be seen in figure 43. This plane is defined by a two dimensional periodic lattice with a basis of two molecules per lattice points. The basis is blue dotted bordered and the flat molecules are nearly parallel to the (-112) plane. One can immediately see that all the molecules have nearly the same long molecular direction but one set of molecules is tilted

**Table 10:** Enhanced pole densities calculated by stereopole for a 27.4 nm thick film of Quinacridone on a Cu(110) substrate (sample 1). The corresponding polefigure (figure 41) was measured at  $2\theta = 41.57^\circ$ . Cu(100) refers to the substrate spots and 5Q represents the  $\beta$  phase of Quinacridone with the (-112) plane parallel to the substrate surface. The numbers 1, 2, 3 and 4 refer to specific calculations where 1 corresponds to blue coloring, 2 to green, 3 to orange and 4 to pink.

crystal / phase	$2\theta^\circ$	(hkl)	$\psi^\circ$	$\phi^\circ$
Cu(110)	37	(001)	90	180
Cu(110)	37	(00-1)	90	0
Cu(110)	53.33	(-110)	90	90
Cu(110)	53.33	(1-10)	90	270
Cu(110)	66.69	(111)	35.26	180
Cu(110)	66.69	(11-1)	35.26	0
<hr/>				
5Q $\beta$ 1	41.80	(-11-1)	18.62	207.57
5Q $\beta$ 1	41.23	(-110)	12.46	207.57
5Q $\beta$ 1	41.62	(-112)	0	6.44
5Q $\beta$ 1	109.58	(1020)	89.71	39.21
5Q $\beta$ 1	109.58	(-1020)	90.29	219.21
5Q $\beta$ 1	41.17	(-111)	6.20	207.57
<hr/>				
5Q $\beta$ 2	41.80	(-11-1)	18.62	32.57
5Q $\beta$ 2	41.23	(-110)	12.46	32.57
5Q $\beta$ 2	41.62	(-112)	0	191.44
5Q $\beta$ 2	109.58	(1020)	89.71	224.21
5Q $\beta$ 2	109.58	(-1020)	90.29	44.21
5Q $\beta$ 2	41.17	(-111)	6.20	32.57
<hr/>				
5Q $\beta$ 3	41.80	(-11-1)	18.62	324.57
5Q $\beta$ 3	41.23	(-110)	12.46	324.57
5Q $\beta$ 3	41.62	(-112)	0	105.00
5Q $\beta$ 3	109.58	(1020)	89.71	156.21
5Q $\beta$ 3	109.58	(-1020)	90.29	336.21
5Q $\beta$ 3	41.17	(-111)	6.20	324.57
<hr/>				
5Q $\beta$ 4	41.80	(-11-1)	18.62	135.57
5Q $\beta$ 4	41.23	(-110)	12.46	135.57
5Q $\beta$ 4	41.62	(-112)	0	294.44
5Q $\beta$ 4	109.58	(1020)	89.71	327.21
5Q $\beta$ 4	109.58	(-1020)	90.29	147.21
5Q $\beta$ 4	41.17	(-111)	6.20	135.57

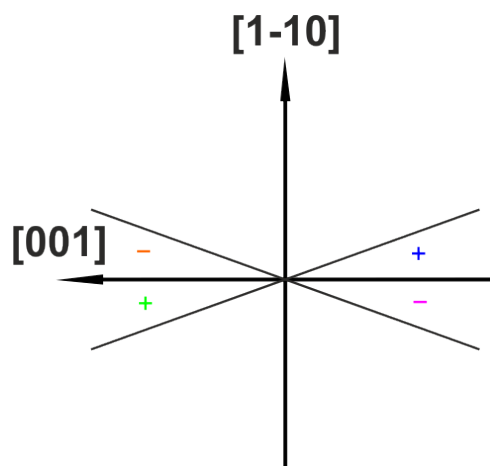


**Figure 42:** Definition of the angle between the copper [001] direction and the long molecular axis. The coloring is identical with the coloring from figure 41, giving the information which crystallite has a positive or negative rotation with respect to the [001] direction of copper.

with respect to the others. The four different orientations of the  $\beta$  domains and their angular distance with respect to the copper [001] direction is given in table 11.

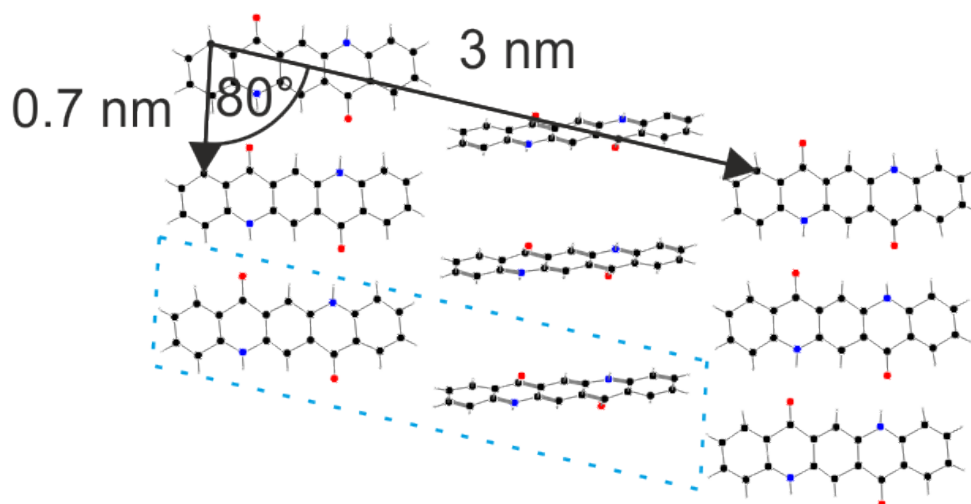


**Figure 43:** Top view of the  $\beta$  phase with the (-112) plane parallel to the surface. The two unit cell vectors have a magnitude of 30 Å and 6.9 Å. The angle between them is 80°. The hole plane is spanned by two molecules per lattice point (cyan borderd).

Crystallite 1 can be seen in figure 44a. The model shows the first domain with its correct orientations with respect to the substrate. It has an angle inclined to the [001] direction of copper of 39.21°. The second domain is displayed in figure 44b with a angular distance of -23.79°. A model for the orientation of crystallite 3 is represented by figure 44c and the last domain can be seen in figure 44d.

**Table 11:** Inclined angles between the copper [001] direction and the long molecular axis of the molecules of a 27.4 nm thick film of Quinacridone on a Cu(110) substrate (sample 1). The crystallite number refers to one specific orientation which has a specific coloring in the polefigures. The column figure stands for the figure number of corresponding models.

Crystallite Number	Angular distance	Coloring	figure
1	$39.21^\circ$	blue	44a
2	$-23.79^\circ$	orange	44b
3	$44.21^\circ$	green	44c
4	$-33^\circ$	pink	44d

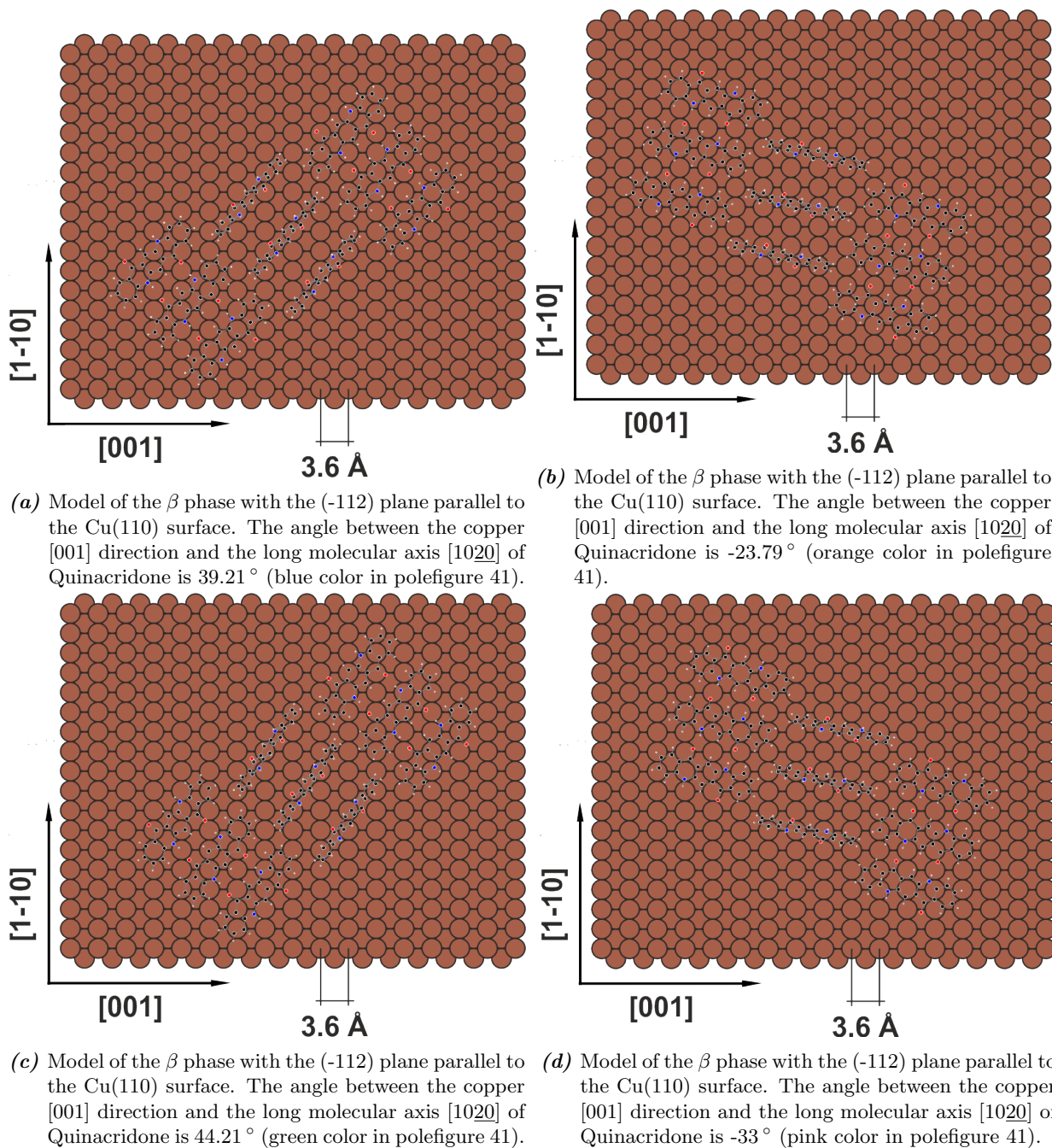


**Figure 44:** Collection of the models associated to the  $\beta$  phase with the (1-12) plane parallel to the surface of a 27.4 nm thick film of Quinacridone on a Cu(110) substrate (sample 1).

### 6.2.2 Sample 2, Quinacridone on Cu(110) at $T_S$ 140 °C

**Sample Preparation** The copper substrate was cleaned by flashing and four circles of sputtering and annealing. The parameters for the cleaning procedure are given in table 12. The copper crystal was heated up to a temperature of 140 °C. The hole evaporation process of Quinacridone took 99 minutes with a rate of 0.036 Å/s, leading to a film thickness of 21.4 nm.

**Table 12:** Sample 2: cleaning parameters of the substrate prior to preparation of the Quinacridone film. In the case of flashing or annealing voltage stands for the filament heating voltage and the current corresponds to the filament current. Temperature is the sample temperature and high voltage is the applied high voltage to accelerate the electrons from the heating filament towards the sample. In the case of a sputtering process current stands for the filament current and the high voltage is the acceleration voltage for argon ions.

Process	Voltage	Current	Pressure $P_s(0.1mA)$	Temperature	High Voltage Settings	Current	Time
Flash	5.2 V	1.65 A		487 °C	500 V	30.5 mA	
Sputter	1k V	25 mA	$10^{-4}$ mbar				12 min
Anneal	5.2 V	1.66 A		507 °C	460 V	26.7 mA	4 min
Sputter	1k V	25 mA	$10^{-4}$ mbar				20 min
Anneal	5.4 V	1.66 A		512 °C	650 V	24.4 mA	3 min
Sputter	1k V	25 mA	$10^{-4}$ mbar				17 min
Anneal	5.2 V	1.65 A		487 °C	609 V	21 mA	3 min
Sputter	1k V	25 mA	$10^{-4}$ mbar				13 min
Anneal	5.4 V	1.65 A		475 °C	700 V	20 mA	5 min

**XRD Measurements** The sample was measured with the Philips X'pert four circle texture goniometer. At the primary side was a collimator with a width of 2 mm and a height of 4 mm. The detector aperture was 1.2 mm and the big beam mask was used. All experimental parameters are given in table 13.

**Table 13:** Experimental parameters for the x-ray diffraction measurements of a 21.4 nm thick film of Quinacridone on a Cu(110) substrate using the Phillips X'Pert four circle Texture Goniometer. The collimator defines the aperture at the side of the x-ray source and detector aperture specifies the aperture on the detector side, followed by the beam mask.

Parameters [units]	Value
Acceleration Voltage [kV]	40
Current [mA]	30
Cr $K_\alpha$ [Å]	2.29
Cr $K_\beta$ [Å]	2.08
Collimator [mm]	2x4
Beam mask	big
Detector aperture [ mm]	1.2

**Specular Scan  $\theta/2\theta$**  Figure 45 shows the specular scan of sample 2. A well defined peak is observed at 42.5°. It is at a different angle compared to the first sample and therefore suggest that a different phase is present. This peak has its origin in the (1-12) plane of the  $\alpha$  phase. The peak itself has got a better aspect ratio than the peak of sample 1. It has a five times higher intensity, even tough the film is six nanometer thinner and therefore less scattering volume is present. The width of the peaks in a specular scan by small crystallite sizes is related to  $\frac{1}{crystallitesize}$ . According to that the elevated

temperature sample turns out to have bigger crystallites. This is consistent with atomic force microscopy measurements of the Johannes Kepler University in Linz from samples with similar conditions. The peak position itself has a little angular shift in  $2\theta$  of  $0.3^\circ$  which could be due to the alignment of the sample.

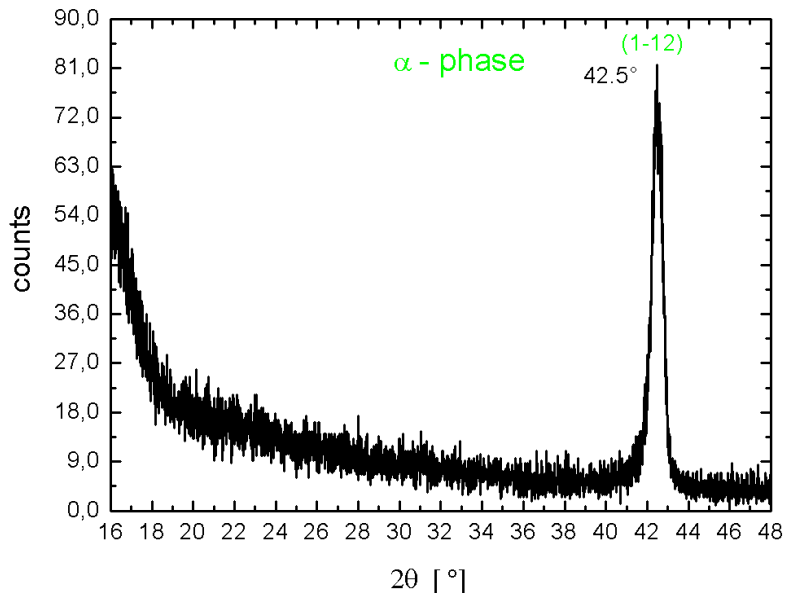


**Figure 45:**  $\theta/2\theta$  scan of a 21.4 nm thick film of Quinacridone on a Cu(110) surface ( sample 2). The peak at  $42.5^\circ$  is from the  $\alpha$  phase and is indexed with (1-12).

**Table 14:** Relevant peak of the  $\alpha$  phase close to the experimentally observed peak at  $42.5^\circ$  of a 21.4 nm thick film of Quinacridone on a Cu(110) substrate (sample 2).

hkl	$2\theta$ [°]	$d_{hkl}$ [Å]	peak shift [°]
1-12	42.179	3.18	0.303

**Rocking Curve** The rocking curve measurement was performed at the specular (1-12) peak (figure 46) of the  $\alpha$  phase. The full width at half maximum is  $2.2^\circ$  and about  $\frac{1}{3}$  of the FWHM of sample 1. The crystallites in sample 2 have a better out-of-plane order. This leads to a bigger detected intensity in a specular scan since a greater amount of crystallites fulfill the parallelism condition and the diffracted signal is able to reach the detector. The peak isn't exactly at half its specular angle. It has a little shift in angle due to not perfect alignment.

**Pole Figures** The polefigure measurement was performed at an angle  $2\theta = 38.72^\circ$  (figure 47) which is exactly between the (101) and (1-11) peaks of the  $\alpha$  phase. The polefigure itself reveals four domains. Every domain has a tuple of enhanced pole densities which is perfect for orienting the simulations. The only combination of phase and (hkl) values which reproduced this pattern was the  $\alpha$  phase with the (1-12) plane parallel to the copper (110) surface. That is consistent with the specular scan given above. We immediately see that all long molecular axis of the molecules are now oriented along to the (001) direction of copper. The  $\beta$  phase before had molecules in the direction of both azimuths. Additionally the molecules no longer lie flat on the substrate surface. There is a little tilt angle in between. Figure

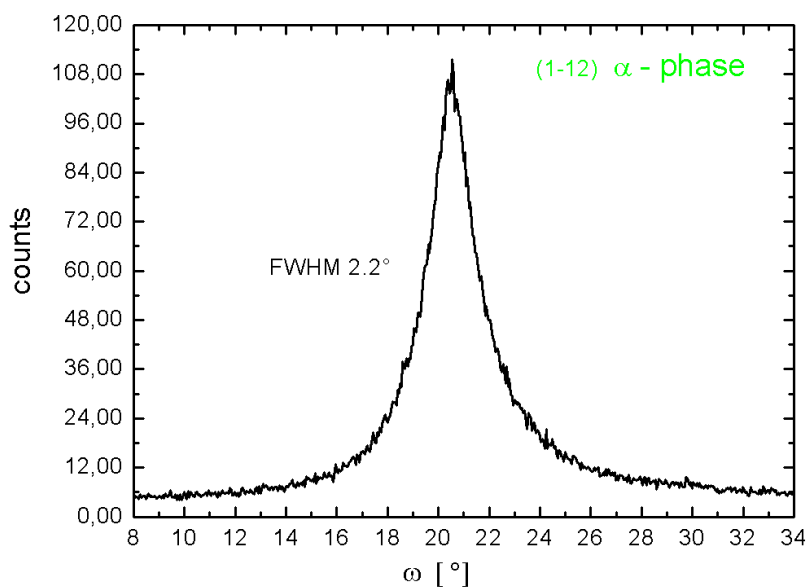


**Figure 46:**  $\omega$  scan of the (1-12) peak ( $2\theta$   $42.5^\circ$ ) from a 21.4 nm thick film of Quinacridone on a Cu(110) substrate (sample 2).

56 illustrates a topview of the molecules from the (1-12) of the  $\alpha$  phase parallel to the substrate surface. All the molecules of one phase have the same direction of the long molecular axis. And the structure can be built up by a unit cell including one molecule.

**Models** Figure 49a, 49b, 49c and 49d display the four  $\alpha$  phases of Quinacridone on the copper (110) surface found in the polefigure at  $2\theta = 38.72^\circ$ . Table 16 contains all the information about the angular distance in azimuthal direction with respect to the substrate directions. Figure 49a shows a model of the blue colored simulation from polefigure 47. The long molecular axis has an angular distance of  $-6^\circ$  inclined to the [001] direction of copper. Additionally the molecules are no longer entirely flat on the surface. There is a tilt angle of  $7^\circ$  between the long molecular axis and the substrate surface. All domains of the  $\alpha$  phase only have orientations close to the [001] substrate direction. The maximum angular distance in both directions is  $-6^\circ$  and  $9.9^\circ$ . These angles are rather small compared to the big angles of the  $\beta$  phase ( $-33^\circ$  to  $44^\circ$ , see table 11). Surprisingly all the molecules lie across the atomic rows of copper. They were expected to be along the atomic rows. But observation showed that lying across the rows is energetic favorable. The orange calculation has an angle of  $6.9^\circ$  to the [001] direction and is shown in figure 49b. The out of plane tilt angle stays the same for all four domains. The green and pink calculations can be seen in figure 49c and 49d with tilt angles of  $-3^\circ$  and  $9.2^\circ$ .

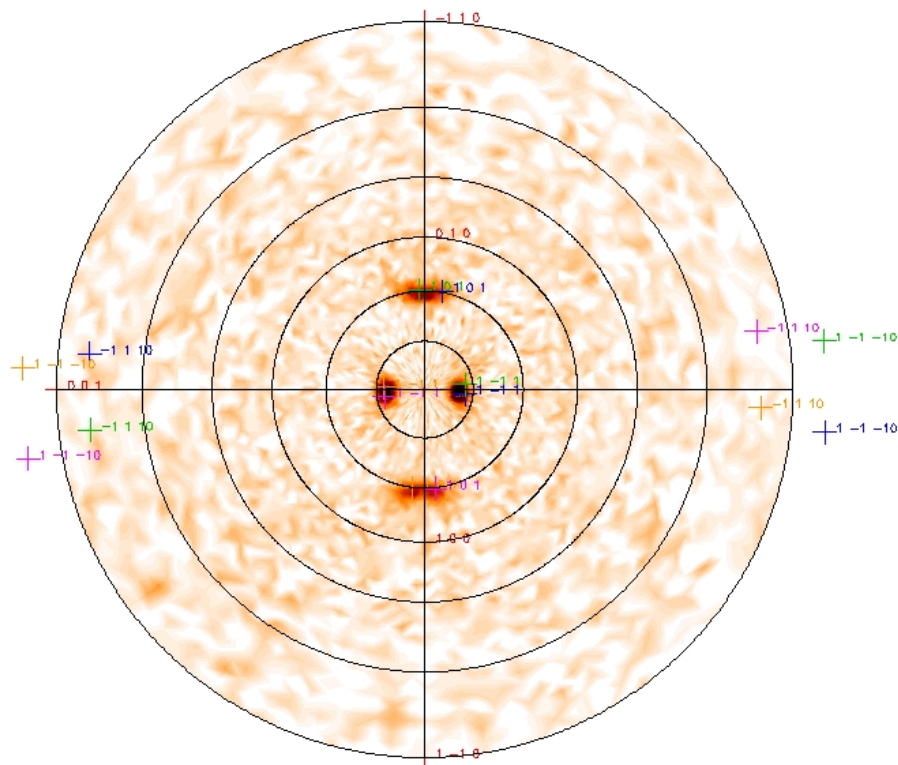


**Figure 47:** Polefigure measured at an angle of  $2\theta = 38.72^\circ$  on a 21.4 nm thick film of Quinacridone on a Cu(110) substrate (sample 2). This is exactly between the  $2\theta$  angles of the (101) and the (1-11) plane. Different colors denote different crystallite orientations for the  $\alpha$  phase, except red. Red crosses represent the copper substrate and its directions. The numbers are the hkl indices of the planes. The stereogram was calculated with the  $\alpha$  phase and the {1-12} family of planes parallel to the Cu(110) surface.

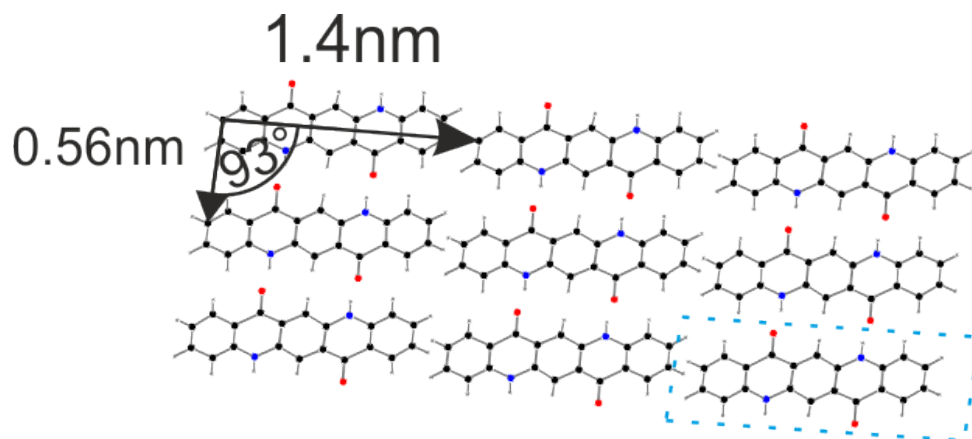


**Figure 48:** Topview of the (1-12) plane of the  $\alpha$  phase. It can be recreated by a two dimensional lattice with one molecule per lattice point. The basis is given inside the cyan dotted parallelogram.

**Table 15:** Enhanced pole densities calculated by stereopole for a 21.4 nm thick film of Quinacridone on a Cu(110) substrate (sample 2). The corresponding polefigure (figure 47) was measured at  $2\theta = 38.72^\circ$ . Cu(100) refers to the substrate spots and 5Q represents the  $\alpha$  phase of Quinacridone with the (1-12) plane parallel to the substrate surface. The numbers 1, 2, 3 and 4 refer to specific calculations where 1 corresponds to blue coloring, 2 to green, 3 to orange and 4 to pink.

crystal / phase	$2\theta^\circ$	(hkl)	$\psi^\circ$	$\phi^\circ$
CU(110)	37	(001)	90	180
CU(110)	53.33	(1-10)	90	270
CU(110)	37	(100)	45	270
CU(110)	37	(-100)	135	90
CU(110)	37	(100)	45	270
CU(110)	37	(010)	45	90
5Q $\alpha$ 1	38.53	(101)	30.26	80.1
5Q $\alpha$ 1	38.72	(1-11)	12.61	353.927
5Q $\alpha$ 1	121.32	(-1110)	84.9	173.92
5Q $\alpha$ 1	121.32	(1-1-10)	95.1	353.92
5Q $\alpha$ 2	38.53	(101)	30.26	6.92
5Q $\alpha$ 2	38.72	(1-11)	12.61	93.1
5Q $\alpha$ 2	121.32	(-1110)	84.9	186.92
5Q $\alpha$ 2	121.32	(1-1-10)	95.1	6.92
5Q $\alpha$ 3	38.53	(101)	30.26	263.1
5Q $\alpha$ 3	38.72	(1-11)	12.61	176.92
5Q $\alpha$ 3	121.32	(-1110)	84.9	356.92
5Q $\alpha$ 3	121.32	(1-1-10)	95.1	176.92
5Q $\alpha$ 4	38.53	(101)	30.26	276.1
5Q $\alpha$ 4	38.72	(1-11)	12.61	189.92
5Q $\alpha$ 4	121.32	(-1110)	84.9	9.92
5Q $\alpha$ 4	121.32	(1-1-10)	95.1	189.92

**Table 16:** Inclined angle between the copper [001] direction and the long molecular axis of the molecules of a 21.4 nm thick film of Quinacridone on a Cu(110) substrate (sample 2). The crystallite number refers to one specific orientation which has a specific coloring in the polefigures. The column figure stands for the figure number of corresponding models.

Crystallite Number	Angular distance	Coloring	figure
1	-6.08°	blue	49a
2	-3.09°	orange	49c
3	6.92°	green	49b
4	9.92°	pink	49d

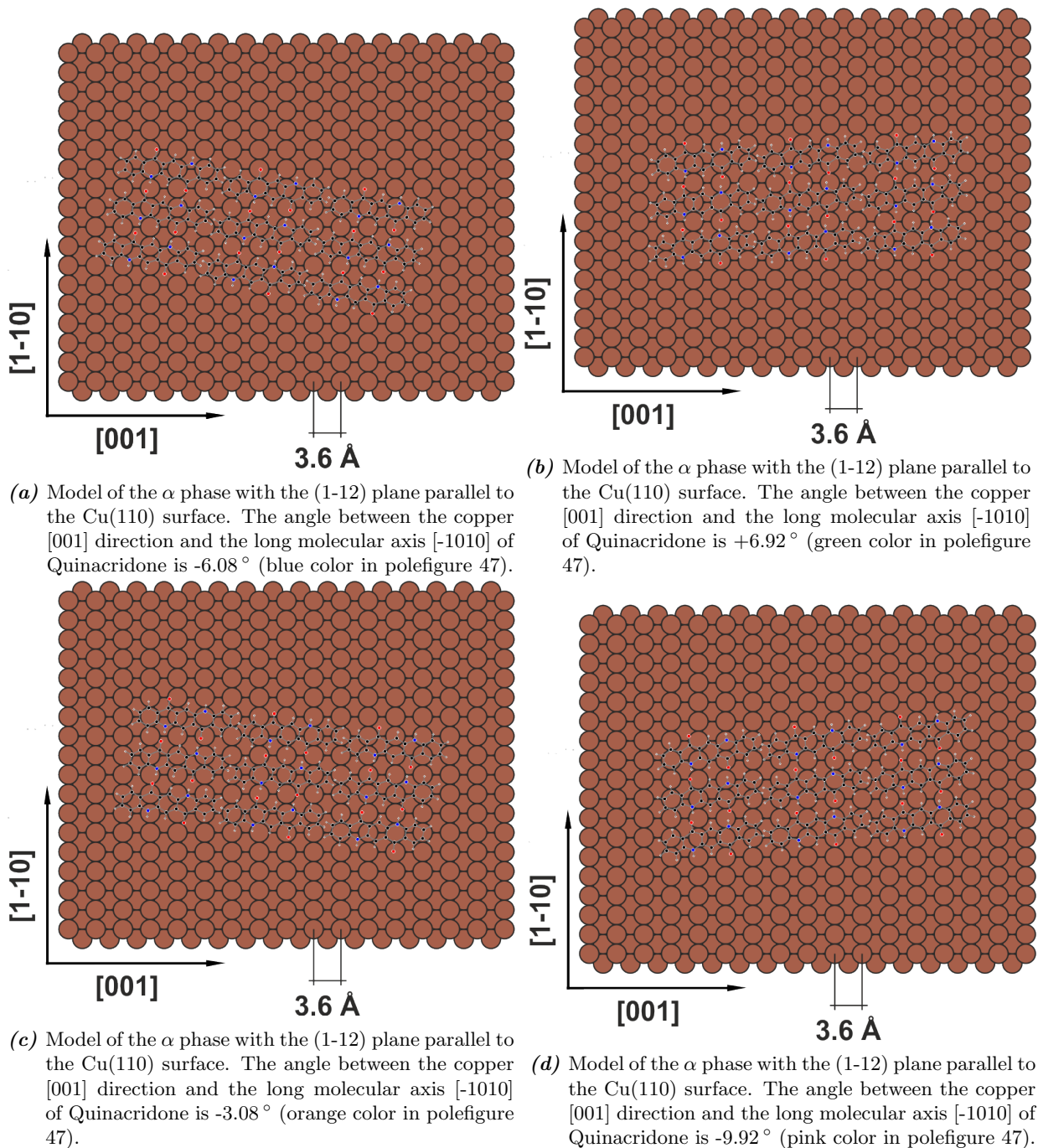


**Figure 49:** Collection of the models associated to the  $\alpha$  phase with the (1-12) plane parallel to the substrate surface of a 21.4 nm thick film of Quinacridone on a Cu(110) substrate (sample 2).

### 6.2.3 Sample 3, Quinacridone on Cu(110)-(2x1)O at $T_S$ 25 °C

**Sample Preparation** Sample 3 was Quinacridone evaporated onto a Copper(110)-(2x1)O reconstruction of the surface. The copper crystal itself was cleaned by an initial flash of the substrate followed by four consecutive cycles of sputtering and annealing. A workfunction measurement was performed as a check for the cleanliness of the substrate surface. The next step was the creation of the Cu(110)-(2x1)O reconstruction. The substrate heating was used to keep it at constant elevated temperature during the time frame for the oxygen reconstruction (190 s). A full oxygen reconstruction is achieved by applying 50 Langmuir of oxygen onto the substrate at elevated temperature (roughly 150 °). 50 Langmuir correspond to a oxygen pressure of  $4^{-7}$  mbar over 180 seconds. This leads to a full stripe system (hole surface covered). The creation of the oxygen reconstruction is very precise [19]. All cleaning and preparation parameters can be found in table 17 and it doesnt contain temperature values, since the thermocouple was broken. Everything at that point was done by experience and inspection by eye. It led to the cleanest copper substrate investigated in the whole master thesis. Evaporation followed at sample temperature = room temperature. A rate of 0.1 Å/s was obtained, leading to a total evaporation time of 44 minutes. The final film had a thickness of 30 nm (299.3 Å).

**Table 17:** Sample 3 : cleaning parameters of the substrate prior to preparation of the Quinacridone film. In the case of flashing or annealing voltage stands for the filament heating voltage and the current corresponds to the filament current. Temperature is the sample temperature and high voltage is the applied high voltage to accelerate the electrons from the heating filament towards the sample. In the case of a sputtering process current stands for the filament current and the high voltage is the acceleration voltage for argon ions.

Process	Voltage	Current	Pressure $P_s(0.1mA)$	High Voltage Settings	Current	Time
Flash	6.8 V	1.95 A		450 V	63 mA	
Sputter	1k V	25 mA	$10^{-4}$ mbar			10 min
Anneal	6.8 V	1.95 A		400 V	63 mA	8 min
Sputter	1k V	25 mA	$10^{-4}$ mbar			25 min
Anneal	6.6 V	1.9 A		400 V	56 mA	10 min
Sputter	1k V	25 mA	$10^{-4}$ mbar			11 min
Anneal	6.6 V	1.9 A		400 V	58 mA	10 min
Sputter	1k V	25 mA	$10^{-4}$ mbar			12 min
Anneal	6.6 V	1.9 A		400 V	57.7 mA	12 min

**XRD Measurements** The Philips X'pert four circle texture goniometer was chosen once more for the investigation of the sample. At primary side was a collimator with a width of 2 mm and a height of 4 mm. The detector aperture had 1.2 mm and the big beam mask was used. All experimental parameters can be seen in table 18.

**Specular Scan  $\theta/2\theta$**  Figure 50 displays the specular scan of the third sample. It looks very similar to the specular scan at elevated temperature. It has a peak at  $2\theta=42.05^\circ$  which is very close to its theoretical value of  $2\theta=42.197^\circ$ . The peak shift is pretty small with  $0.147^\circ$ . It has the smallest angular shift. The Full Width at Half Maximum of this peak is slightly broader than the peak of sample 2. One reason could be that the crystallites are slightly larger on the elevated temperature sample. Ultraviolet Photoemission spectroscopy shows that elevated temperatures lead to islanding and therefore bigger crystallite sizes which is great for x-ray diffraction experiments but not preferred for UPS measurements.

**Table 18:** Experimental parameters for the x-ray diffraction measurements of a 30 nm thick film of Quinacridone on a Cu(110)-(2x1)O reconstruction using the Phillips X'Pert four circle Texture Goniometer. The collimator defines the aperture at the side of the x-ray source and detector aperture specifies the aperture on the detector side, followed by the beam mask.

Parameters [units]	Value
Acceleration Voltage [kV]	40
Current [mA]	30
Cr $K_\alpha$ [ $\text{\AA}$ ]	2.29
Cr $K_\beta$ [ $\text{\AA}$ ]	2.08
Collimator [mm]	2x4
Beam mask	big
Detector aperture [ mm]	1.2

Additional features occur in the specular scan. A peak arises at  $2\theta = 38.6^\circ$  which corresponds to the  $\alpha$  phase with the (1-11) plane parallel to the surface. Table 19 gives a overview of the relevant Quinacridone peaks, their shifts and the corresponding netplane distance. The peaks at  $2\theta = 34.6^\circ$  and  $25.7^\circ$  have their origin in the diffraction of the higher harmonics ( $\frac{\lambda}{3}$  and  $\frac{\lambda}{4}$ ) of the x-ray source at the copper (220) plane.

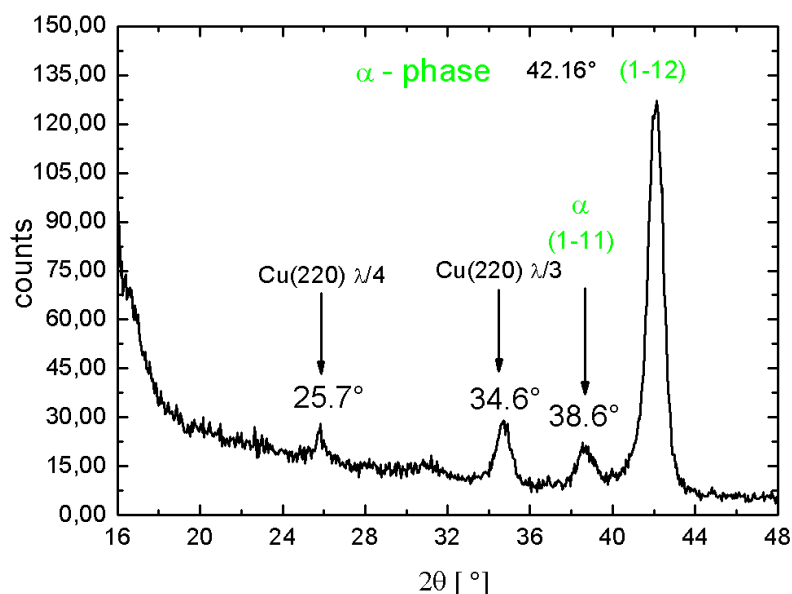


**Figure 50:**  $\theta/2\theta$  scan of a 30 nm thick film of Quinacridone on a Cu(110)-(2x1)O reconstruction (sample 3). The peak at  $42.16^\circ$  is from the  $\alpha$  phase and originates in the (1-12) plane. A second  $\alpha$  phase can be seen in the peak at  $38.6^\circ$ . It corresponds to the (1-11) plane.

**Rocking Curve** The rocking curve of the (1-12) peak can be seen in figure 51. It has a Full Width at Half Maximum of  $3.7^\circ$  and is therewith similar to the elevated temperature sample better aligned then the  $\beta$  phase from sample 1. (FWHM  $6.7^\circ$ ).

**Pole Figures** Two polefigures with a meaningful enhanced pole density pattern were recorded. The first polefigure was measured at an angle of  $2\theta = 21.19^\circ$  (figure 52) and could be reproduced only by

**Table 19:** Relevant peaks of the  $\alpha$  phase close to the experimental measured peaks at  $42.16^\circ$  and  $38.6^\circ$  of a 30 nm thick film of Quinacridone on a Cu(110)-(2x1)O reconstruction (sample 3).

hkl	$2\theta$ [ $^\circ$ ]	$d_{hkl}$ [ $\text{\AA}$ ]	peak shift [ $^\circ$ ]
1-12	42.05	3.18	0.15
1-11	38.61	3.45	0.11

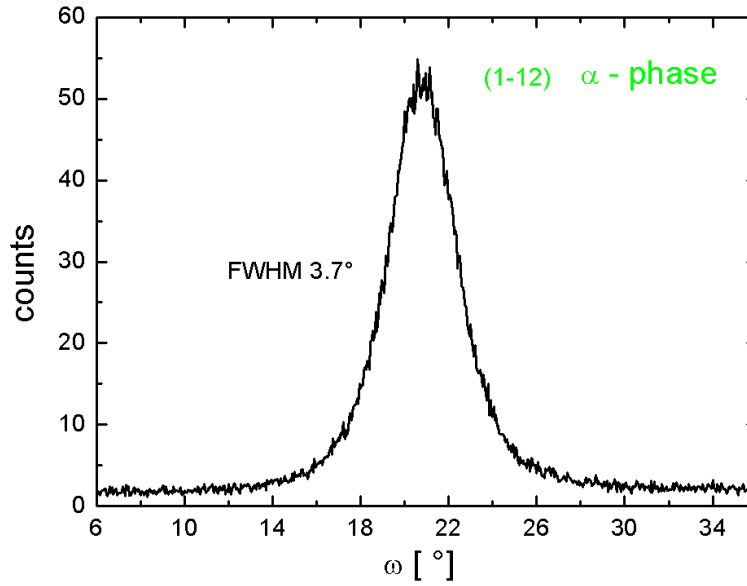


**Figure 51:**  $\omega$  scan of the (1-12) peak ( $2\theta$   $42.16^\circ$ ) from a 30 nm thick film of Quinacridone on a Cu(110)-(2x1)O reconstruction (sample 3).

simulations of the  $\alpha$  phase with two different sets of miller indices, namely (1-11) and (1-12). The second polefigure was measured at  $2\theta = 38.72^\circ$  (figure 54) and corresponds to the EPD pattern of the (1-12) and the (1-11) plane of the  $\alpha$  phase. Those results are in excellent agreement with the specular scan: The majority phase is the (1-12)  $\alpha$  phase and the minority phase has the (1-11) plane parallel to the substrate surface. The long molecular axis lies close to the [001] substrate direction, regardless of the current state of phase. Every Quinacridone molecule is now closely aligned to the atomic rows of oxygen. All the polefigures are symmetric (as they should be). Every polefigure has four domains of the  $\alpha$  phase and all the molecules have a tilt angle inclined to the substrate surface. A topview of the (1-11) and (1-12)  $\alpha$  phases can be seen in figure 55 and 56. They look similar but the (1-11) plane has bigger lattice vectors (15.4 nm and 6.4 nm) and the angle between those vector is now smaller with  $71.4^\circ$  compared to the  $93^\circ$  of the (1-12) plane.

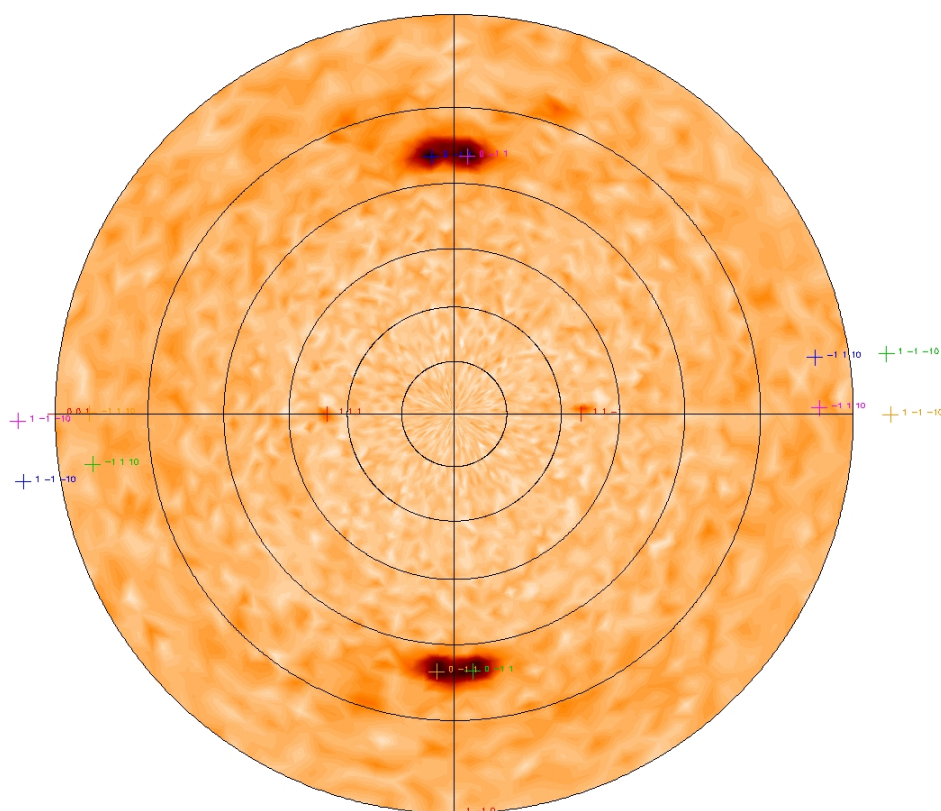


**Figure 52:** Polefigure measured at an angle of  $2\theta = 21.019^\circ$  on a 30 nm thick film of Quinacridone on a Cu(110)-(2x1)O reconstruction (sample 3). This corresponds to the (0-11) plane. Different colors denote different crystallite orientations for the  $\alpha$  phase, except red. Red crosses represent the copper substrate and its directions. The numbers are the hkl indices of the planes. The stereogram was calculated with the  $\alpha$  phase and the {1-12} family of planes parallel to the Cu(110)-(2x1)O surface.

**Models** Figures 57a, 57b, 57c and 57d are the models for the different phases measured in polefigure 54. Polefigure 54 shows the enhanced pole density pattern for the (1-12)  $\alpha$  phase. Figure 57a shows the model for the blue simulation. The long molecular axis [1-110] has an angle of  $3.92^\circ$  inclined to the [001] direction of the copper substrate. Additionally a tilt angle of  $4.9^\circ$  exists between the (110) plane of the substrate and the [1-110] direction. This means that the molecules lie only approximately flat on the surface. They are tilted with an angle of  $-4.9^\circ$  with respect to the substrate surface and the tilt angle is the same for every domain. Polefigure 57b displays the green simulation. It has an inplane

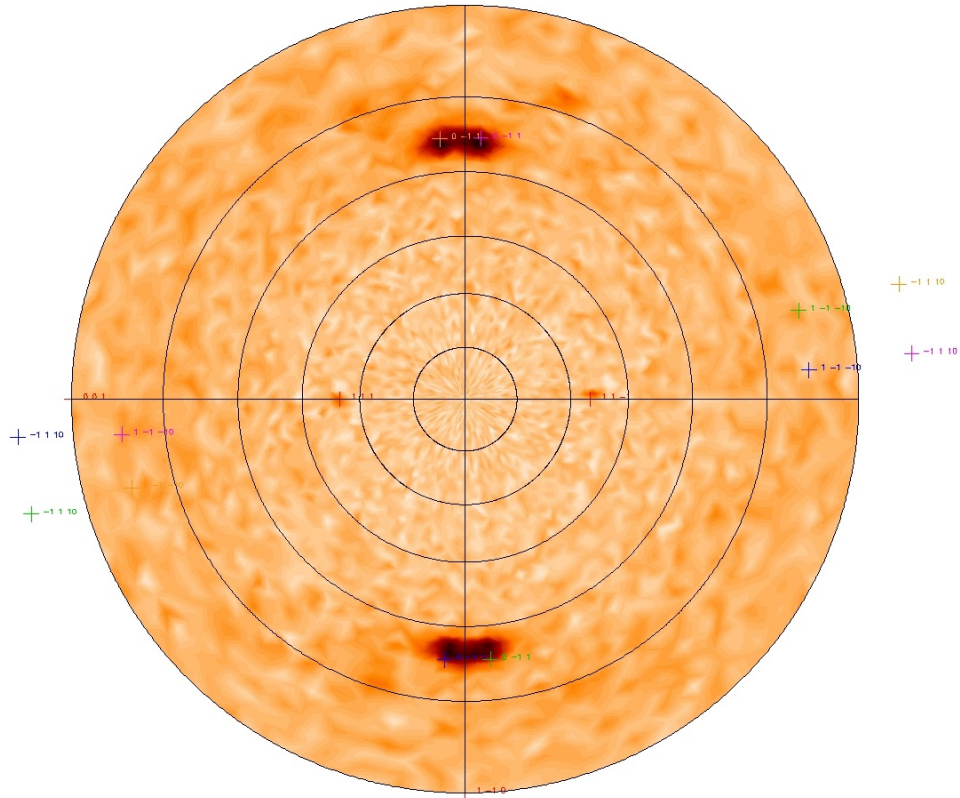


**Figure 53:** Polefigure measured at an angle of  $2\theta = 21.019^\circ$  on a 30 nm thick film of Quinacridone on a Cu(110)-(2x1)O reconstruction (sample 3). This corresponds to the (0-11) plane. Different colors denote different crystallite orientations for the  $\alpha$  phase, except red. Red crosses represent the copper substrate and its directions. The numbers are the hkl indices of the planes. The stereogram was calculated with the  $\alpha$  phase and the {1-11} family of planes parallel to the Cu(110)-(2x1)O surface.

**Table 20:** Inclined angles between the copper [001] direction and the long molecular axis of the molecules of a 30 nm thick film of Quinacridone on a Cu(110)-(2x1)O reconstruction (sample 3). The crystallite number refers to one specific orientation which has a specific coloring in the pole-figures. The column figure stands for the figure number of corresponding models.

Crystallite Number	Angular distance	Coloring	figure
1	$4.84^\circ$	blue	58a
2	$14.85^\circ$	orange	58a
3	$14.85^\circ$	green	58a
4	$5.85^\circ$	pink	58c

**Table 21:** Enhanced pole densities calculated by stereopole for a 30 nm thick film of Quinacridone on a Cu(110) substrate (sample 3). The corresponding polefigure (figure 53) was measured at  $2\theta = 21.02^\circ$ . Cu(100) refers to the substrate spots and 5Q represents the  $\alpha$  phase of Quinacridone with the (1-11) plane parallel to the substrate surface. The numbers 1, 2, 3 and 4 refer to specific calculations where 1 corresponds to blue coloring, 2 to green, 3 to orange and 4 to pink.

crystal / phase	$2\theta^\circ$	(hkl)	$\psi^\circ$	$\phi^\circ$
Cu(110)	37	(001)	90	180
Cu(110)	53.3	(1-10)	90	270
Cu(110)	66.69	(111)	35.26	180
Cu(110)	66.69	(11-1)	35.26	0
5Q $\alpha$ 1	21	(0-11)	67.2	265.5
5Q $\alpha$ 1	121.32	(1-1-10)	82.5	4.8
5Q $\alpha$ 1	121.32	(-1110)	97.5	184.85
5Q $\alpha$ 2	21	(0-11)	67.2	275.5
5Q $\alpha$ 2	121.32	(1-1-10)	82.5	14.85
5Q $\alpha$ 2	121.32	(-1110)	97.5	194.85
5Q $\alpha$ 3	21	(0-11)	67.2	95.5
5Q $\alpha$ 3	121.32	(1-1-10)	82.5	194.85
5Q $\alpha$ 3	121.32	(-1110)	97.5	14.85
5Q $\alpha$ 4	21	(0-11)	67.2	86.5
5Q $\alpha$ 4	121.32	(1-1-10)	82.5	185.85
5Q $\alpha$ 4	121.32	(-1110)	97.5	5.85

**Table 22:** Inclined angles between the copper [001] direction and the long molecular axis of the molecules of a 30 nm thick film of Quinacridone on a Cu(110)-(2x1)O reconstruction (sample 3). The crystallite number refers to one specific orientation which has a specific coloring in the polefigures. The column figure stands for the figure number of corresponding models.

Crystallite Number	Angular distance	Coloring	figure
1	+3.92°	blue	57a
2	+8.92°	orange	57b
3	2.92°	green	57c
4	-3.08°	pink	57d

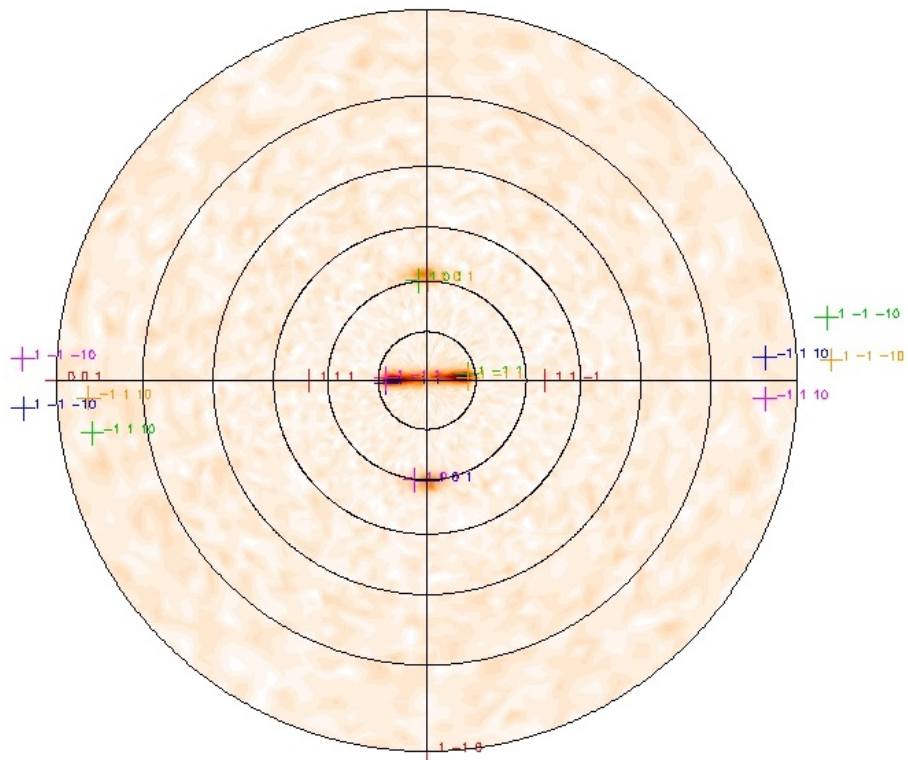


**Figure 54:** Polefigure measured at an angle of  $2\theta = 38.72^\circ$  on a 30 nm thick film of Quinacridone on a Cu(110)-(2x1)O reconstruction (sample 3), which is exactly between the (101) and the (1-11) plane. Different colors denote different crystallite orientations for the  $\alpha$  phase, except red. Red crosses represent the copper substrate and its directions. The numbers are the hkl indices of the planes. The stereogram was calculated with the  $\alpha$  phase and the {1-12} family of planes parallel to the Cu(110)-(2x1)O surface.

**Table 23:** Enhanced pole densities calculated by stereopole for a 30 nm thick film of Quinacridone on a Cu(110) substrate (sample 3). The corresponding polefigure (figure 54) was measured at  $2\theta = 38.72^\circ$ . Cu(100) refers to the substrate spots and 5Q represents the  $\alpha$  phase of Quinacridone with the (1-12) plane parallel to the substrate surface. The numbers 1, 2, 3 and 4 refer to specific calculations where 1 corresponds to blue coloring, 2 to green, 3 to orange and 4 to pink.

crystal / phase	$2\theta^\circ$	(hkl)	$\psi^\circ$	$\phi^\circ$
Cu(110)	37	(001)	90	180
Cu(110)	53.3	(1-10)	90	270
Cu(110)	66.69	(111)	35.26	180
Cu(110)	66.69	(11-1)	35.26	0
5Q $\alpha$ 1	38.72	(1-11)	12.6	183.9
5Q $\alpha$ 1	38.53	(101)	30.26	270.1
5Q $\alpha$ 1	121.32	(1-1-10)	95.26	183.92
5Q $\alpha$ 1	121.32	(-1110)	84.9	3.92
5Q $\alpha$ 2	38.72	(1-11)	12.6	183.9
5Q $\alpha$ 2	38.53	(101)	30.26	270.1
5Q $\alpha$ 2	121.32	(1-1-10)	95.26	183.92
5Q $\alpha$ 2	121.32	(-1110)	84.9	3.92
5Q $\alpha$ 3	38.72	(1-11)	12.6	8.92
5Q $\alpha$ 3	38.53	(101)	30.26	95.1
5Q $\alpha$ 3	121.32	(1-1-10)	95.26	8.92
5Q $\alpha$ 3	121.32	(-1110)	84.9	188.92
5Q $\alpha$ 4	38.72	(1-11)	12.6	2.92
5Q $\alpha$ 4	38.53	(101)	30.26	89.1
5Q $\alpha$ 4	121.32	(1-1-10)	95.26	182.92
5Q $\alpha$ 4	121.32	(-1110)	84.9	2.92
5Q $\alpha$ 4	38.72	(1-11)	12.6	176.92
5Q $\alpha$ 4	38.53	(101)	30.26	263.1
5Q $\alpha$ 4	121.32	(1-1-10)	95.26	176.92
5Q $\alpha$ 4	121.32	(-1110)	84.9	356.92

angle with respect to the [001] substrate azimuth of  $8.92^\circ$ . Polefigure 57c (orange) and 57d (pink) have an angle inclined to the copper [001] direction of  $2.92^\circ$  and  $-3.08^\circ$ . The different domains are closer aligned to the [001] one direction then in the previous samples. The  $\beta$  phase has a maximum angle of  $44.21^\circ$  inclined to the [001] direction. Quinacridone on elevated temperature evaporation has an angle of  $9.9^\circ$  where in the previous measurements the biggest angle is  $8.9^\circ$  with respect to the [001] substrate azimuth.

Figures 58a, 58b and 58c are the corresponding model for polefigure 53. They shows the calculated and measured enhanced pole density pattern for the (1-11)  $\alpha$  phase. Table 20 is a summary of the different models, their figure number, the inclined angle and the coloring in the polefigure. The correct value for every enhanced pole density can be found in table 21. They all have an tilt angle of  $7.5^\circ$  with respect to the substrate surface and all the molecules are close to the [001] azimuth of copper. Figure 58a is the model for the blue simulation. It has an angle of  $4.84^\circ$  with respect to the copper [001] azimuth.

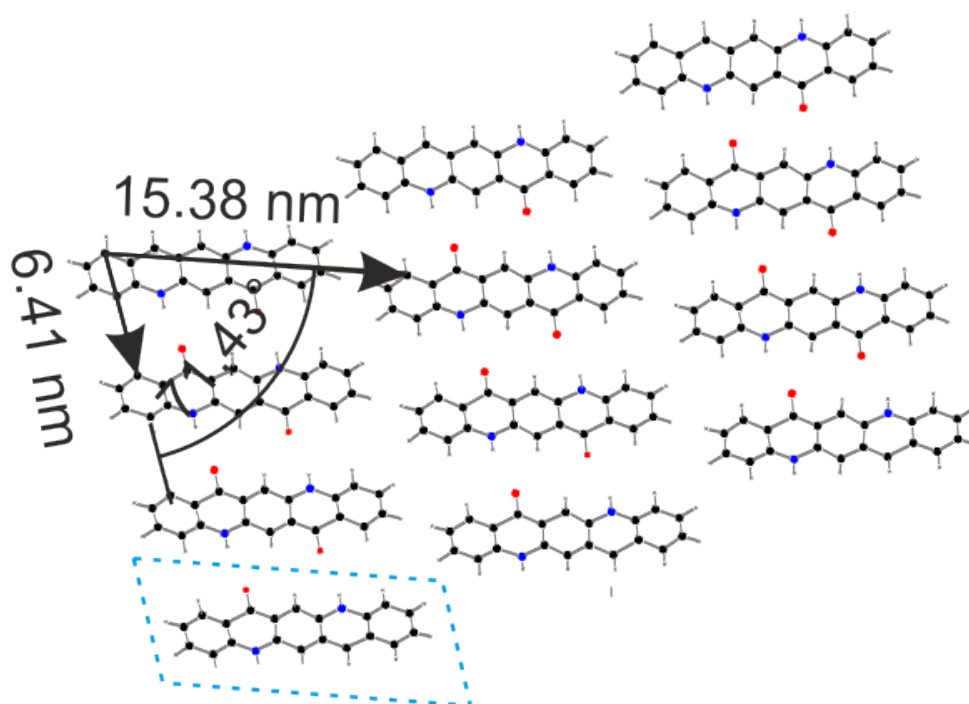


**Figure 55:** Topview of the (1-11) plane of the  $\alpha$  phase. It can be recreated by a two dimensional lattice with one molecule per lattice point. The basis can be seen inside the cyan dotted parallelogram.

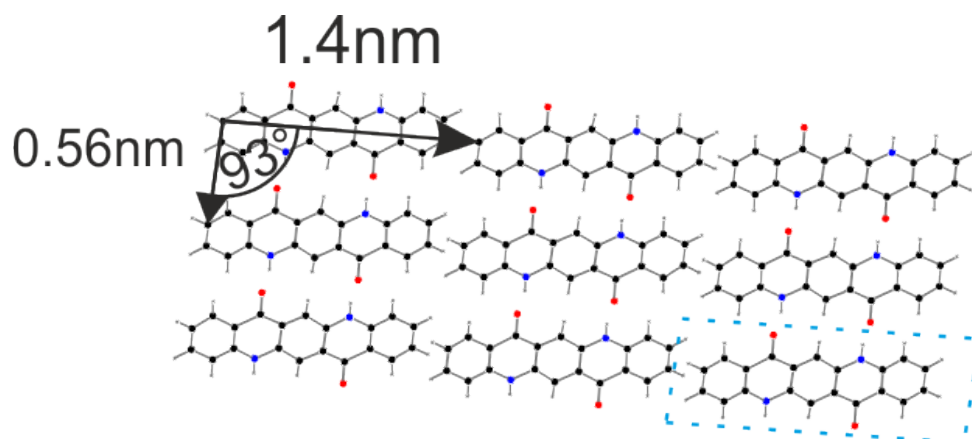


**Figure 56:** Topview of the (1-12) plane of the  $\alpha$  phase. It can be recreated by a two dimensional lattice with one molecule per lattice point. The basis can be seen inside the cyan dotted parallelogram.

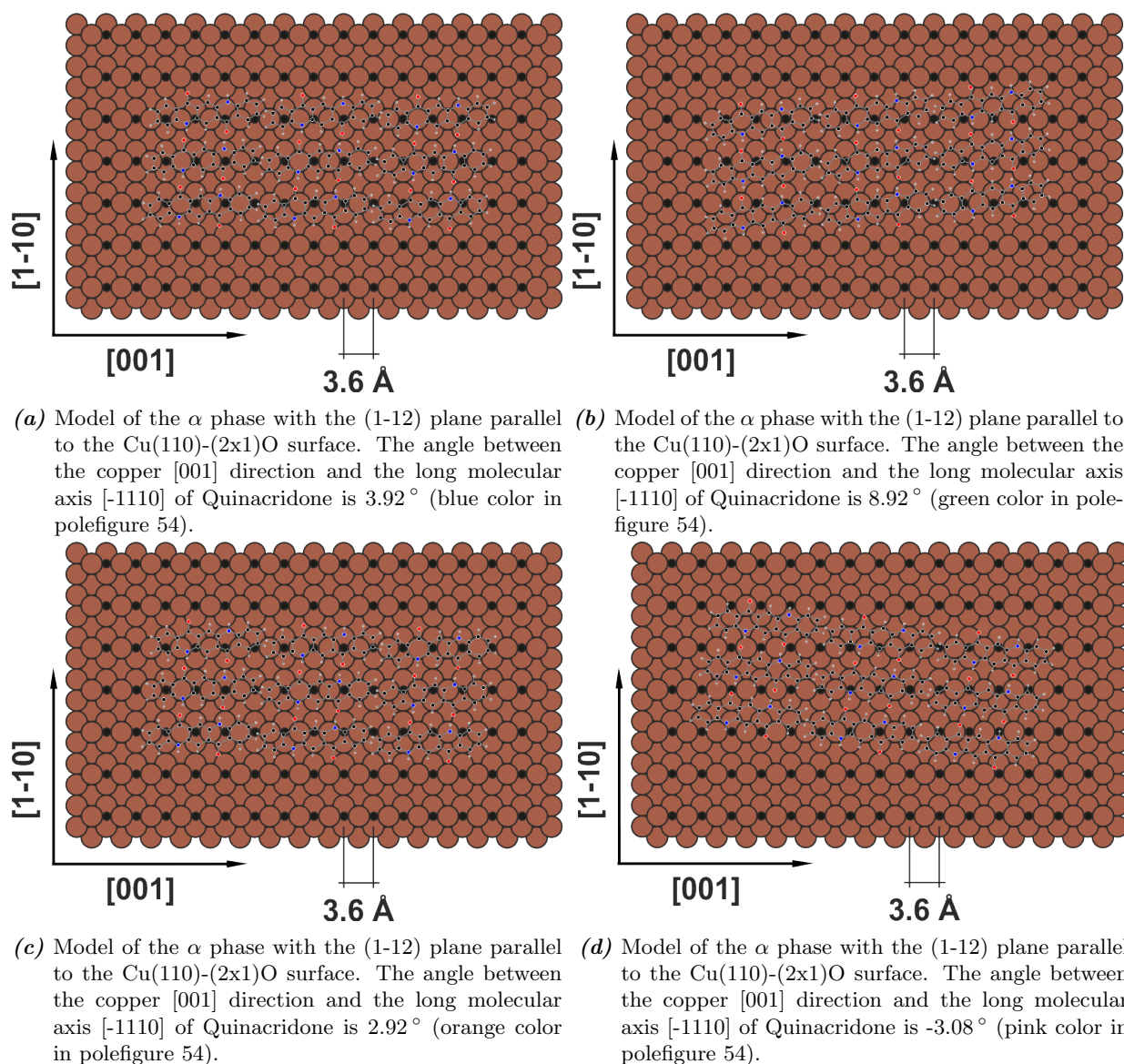
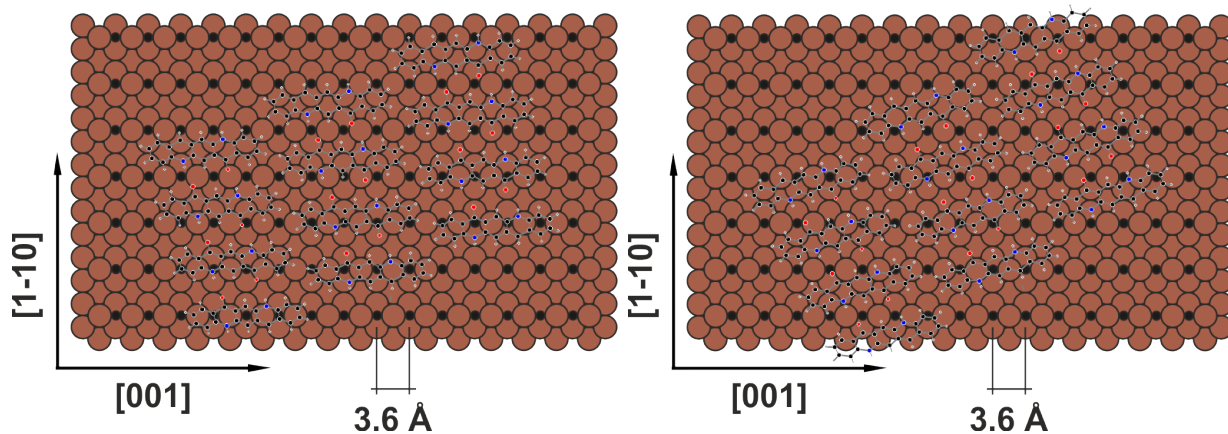
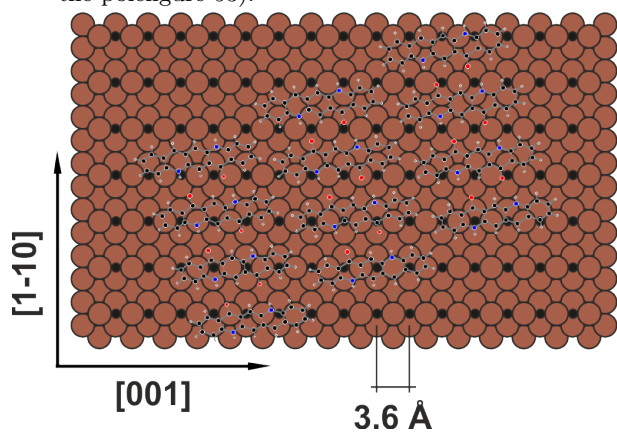


**Figure 57:** Collection of the models associated to the  $\alpha$  phase with the (1-12) plane parallel to the Cu(110)-(2x1)O surface of a 30 nm thick film of Quinacridone (sample 3).



- (a) Model of the  $\alpha$  phase with the (1-11) plane parallel to the Cu(110)-(2x1)O surface. The angle between the copper [001] direction and the long molecular axis [-1110] of Quinacridone is  $4.84^\circ$  (blue color in the polefigure 53).
- (b) Model of the  $\alpha$  phase with the (1-11) plane parallel to the Cu(110)-(2x1)O surface. The angle between the copper [001] direction and the long molecular axis [-1110] of Quinacridone is  $14.84^\circ$  (green and orange color in the polefigure 53).



- (c) Model of the  $\alpha$  phase with the (1-11) plane parallel to the Cu(110)-(2x1)O surface. The angle between the copper [001] direction and the long molecular axis [-1110] of Quinacridone is  $5.84^\circ$  (pink color in the polefigure 53).

**Figure 58:** Collection of the models associated to the  $\alpha$  phase with the (1-11) plane parallel to the Cu(110)-(2x1)O surface of a 30 nm thick film of Quinacridone (sample 3).

### 6.3 Growth and Electronic Structure measurements of Monolayer, Multilayer and Bulk Films of Quinacridone on Cu(110) and Cu(110)-(2x1)O.

Film growth was performed in UHV on atomically controlled single crystal surfaces Cu(110) and Cu(110)-(2x1)O. The controllable parameters of the films were deposition rate, substrate temperature and the substrate itself. The evaporation rate was controlled by a quartz micro-balance. The evaporators were home built based on a heatwave button heater. For the rates used I and V of the heater were between 1.25-1.46 A and 1.7-6.1 V. The spread in the I and U settings originates in the different resistance of the three used evaporators. The most used setting were I and V of 1.3 A and 6.1 V. All experimental parameters are given in table 24. Clean Cu(110) and Cu(110)-(2x1)O are both highly corrugated to encourage single molecular orientation and thus crystallite orientation. These substrates have a different corrugation, different chemistry and different interactions strengths in the first monolayer. ARUPS was used to control the growth and ascertain whether there was a preferred orientation. The objectives where:

- Can we grow single crystalline Quinacridone for latter structure determination (x-ray diffraction, chapter 6.2).
- To acquire a reliable DOS as a benchmark for assessing theoretical calculations for the hydrogen bonded system.[20]

**Table 24:** Experimental parameters for the growth of Quinacridone (5Q) on Cu(110) and Cu(110)-(2x1)O. Heating voltage and heating current are the applied voltage and the measured current at the button heater. Three different sets for the heating parameters are given, since three different evaporators were used. This is accounted for with the numbers 1, 2 and 3.

Parameters [units]	Value
Density 5Q [ $\frac{g}{cm^3}$ ]	1.47
Heating Voltage 1 [V]	1.7-1.9
Heating Current 1 [A]	1.4-1.46
Heating Voltage 2 [V]	6.1
Heating Current 2 [A]	1.3
Heating Voltage 3 [V]	4.7
Heating Current 3 [A]	1.25
Evaporation Rate Range [ $\frac{\text{Å}}{\text{s}}$ ]	0.01-0.045
Substrate Temperature [°C]	25 and 140

The following chapters treats the investigation of thin films of Quinacridone via ultraviolet photoemission spectroscopy. Thin in this context means films with a thickness from a single monolayer (3.2 Å) up to multilayer systems consisting of a couple of monolayers. There will be one exception in the last chapter, where we were able to measure the electronic structure of a thick film used for x-ray diffraction experiments. All the samples were prepared and measured under UHV conditions as described in section 5.1.2. The electronic structure of the  $\beta$  phase of Quinacridone is given in advance to the following chapter in figure 59. It shows the electronic structure at normal emission (solid line) and at a takeoff angle of 50° (dotted line). The contributing orbitals, their wavefunction and their energy ordering can be seen. The orbitals indicated in yellow and orange originate from localized  $\sigma$  orbitals, whereas all the other orbitals have their origin in delocalized  $\pi$  orbitals. The energetic positions were obtained with optimally tuned ranged separated hybrid functional (OT-SRSH) calculations and are in excellent agreement with the measured photoemission spectra.[20]

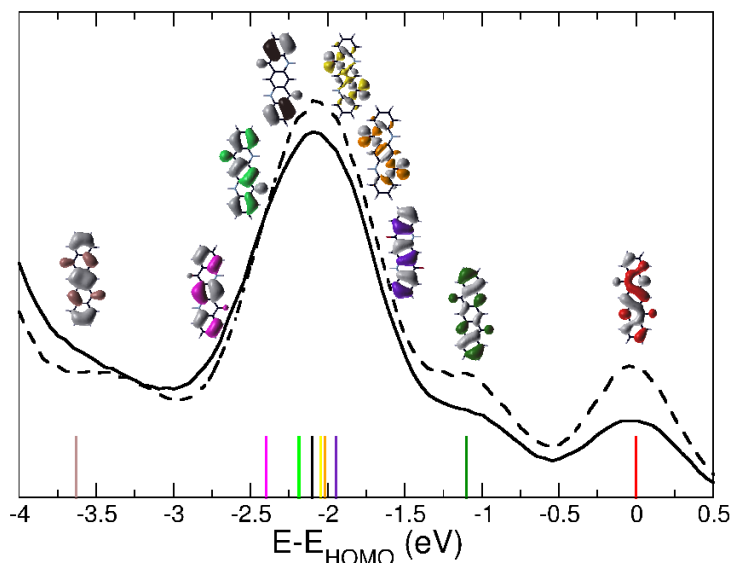


**Figure 59:** Experimental measured photoemission spectra of the  $\beta$  phase of Quinacridone at normal emission (solid line) and at a takeoff angle of  $50^\circ$  (dotted line). The contributing orbitals and their wavefunction are displayed. Their energetic positions are given in the colored vertical lines.[20]

### 6.3.1 Experiments on Cu(110) at $T_S$ 25 °C

**Dosing Series** Figure 60 shows a dosing series (uptake curve) of Quinacridone on a clean copper(110) substrate. Every spectrum in this plot is acquired at a takeoff angle of  $50^\circ$  and in the [001] azimuthal direction. Different colors stand for different film thicknesses. The black line on the bottom is the spectrum of clean copper. Zero is the energy reference of the ups spectrum. It is the position of the Fermi energy of copper. Copper has the 4s electron at a binding energy of -1 eV with respect to the Fermi level. The d bands are in the range of -5 to -2 eV. The Y-axis in figure 60 reflects the counts of the individual signals which are given in arbitrary units. The copper spectra had to be scaled down because of the extremely high intensity of the d bands. A individual offset was introduced for every spectrum in order to make the plots better visible. The red line is the spectrum of a monolayer of Quinacridone evaporated onto the substrate surface. The first thing to notice is an increase of intensity close to the Fermi level (even without the copper descaling, division by 3). This peak originates in the LUMO of Quinacridone. Usually we should not be able to see the LUMO with UPS measurements. It is per definition the lowest unoccupied molecular orbital and therefore has no electrons in it. In our case the Fermi level of copper is energetically above the LUMO of Quinacridone and since they are in contact a transfer of electrons is possible. The LUMO is being filled due to the chemical bonding of copper with Quinacridone. This makes it possible to measure the LUMO of Quinacridone with UPS. If it is really the LUMO then it should disappear in the second layer. UPS is an extremely surface sensitive technique and the second layer cannot be doped with electrons from the copper surface, since this layer is now spatially separated. The LUMO vanishes in the second layer (figure 60 blue curve). Its energetic position with a binding energy of -0.2 eV is extremely close to the Fermi level. Sticking to the spectrum of a monolayer (red curve, figure 60) we observe a new peak arising at -1.5 eV. This is the highest occupied molecular orbital (HOMO) of Quinacridone. By moving down further in binding energy changes in the copper d-band structure can be seen: The influence of the d bands is too strong to be able to tell which features originate from the molecule and which originate from copper in the monolayer in this area. Two more

features arise below the copper d bands. In order to distinguish which features are from the molecule and which features are from copper thicker films have to be measured. The blue spectrum in figure 60 was measured on a two monolayer thick film (6.4 Å). All the molecular features are more distinct. Every peak experienced a characteristic shift of 0.8 eV. By adding another monolayer of Quinacridone a spatial separation of the top layer of 5Q from the copper atoms occur. A positive hole is left during a photo excitation process, which leads to an attractive potential for the outgoing electrons and reduces their kinetic energy. This positive photo hole can be screened by substrate electrons, electrons from neighboring molecules and electrons in the molecule itself where the excitation took place. The screening of the photo hole will be best close to the substrate surface. The copper crystal is a infinite source of free electrons. The better the screening the more kinetic energy will be measured. Therefore the monolayer has a lower binding energy than the bi-layer or the multilayer. There should be no further change of the electronic positions of the molecular orbitals for additional layers. Which is observed for the orange spectrum (18 Å thick film) in figure 60. The only change is that the molecular features are better defined and the copper d bands are completely suppressed. The ionization potential obtained for the monolayer and multilayer are  $IP_{mono} = 5.4\text{ eV}$  and  $IP_{multi} = 6.1\text{ eV}$ .

compared with high level density functional theory calculations. It shows the contributing molecular states

**Determination of the Work Function and the Monolayer thickness** Uptake curves can be used to determine the work function and the thickness of the monolayer of Quinacridone. Clean copper has a work function between 4.3 eV and 4.4 eV. Adding Quinacridone to it will lower its work function. Later chapters will show that the addition of oxygen leads to an increase of the work function. The work function is per definition the energy that is needed to remove an electron from a solid and place it at a point in the vacuum outside the solid surface. Therefore we expect the work function to saturate once the monolayer is completed. There should be no change for increasing thickness up to a multilayer system. Figure 61 shows different work functions plotted against their film thickness. Exponential convergence towards saturation could be observed. The work function for Quinacridone on a Cu(110) surface is 3.8 eV and the corresponding thickness of the monolayer is 3.2 Å.

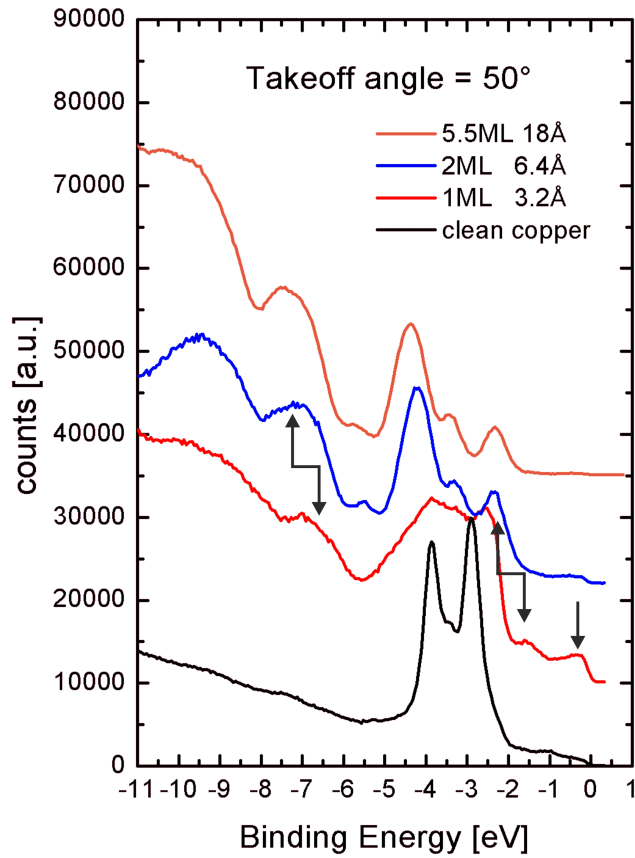


**Figure 60:** UPS measurement of a dosing series (uptake curve) of Quinacridone on a Cu(110) substrate. The measurement was performed along the [001] azimuthal direction at a takeoff angle of 50°. The dosing series starts with clean copper at the bottom (black line), continues with a monolayer (red), a bi-layer (blue) and stops at a multilayer with a thickness of 5.5 ML.

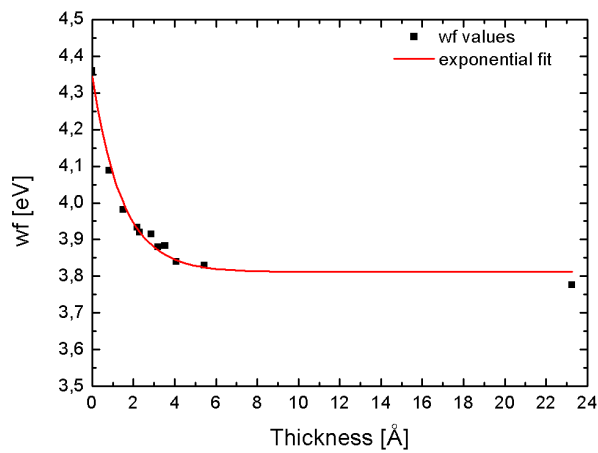
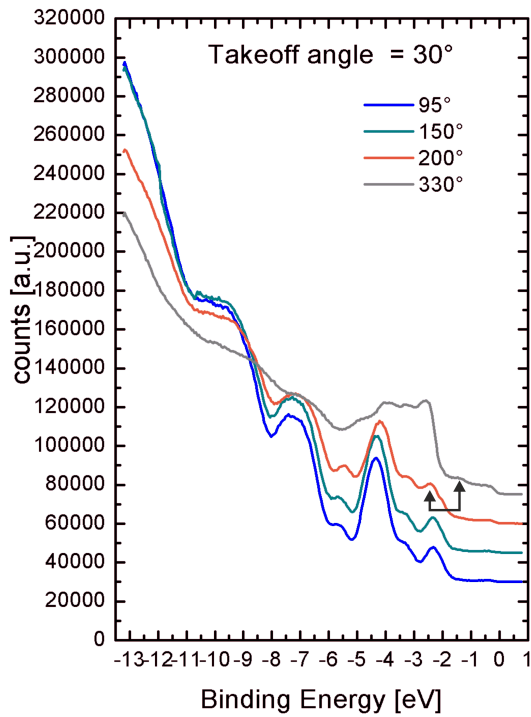
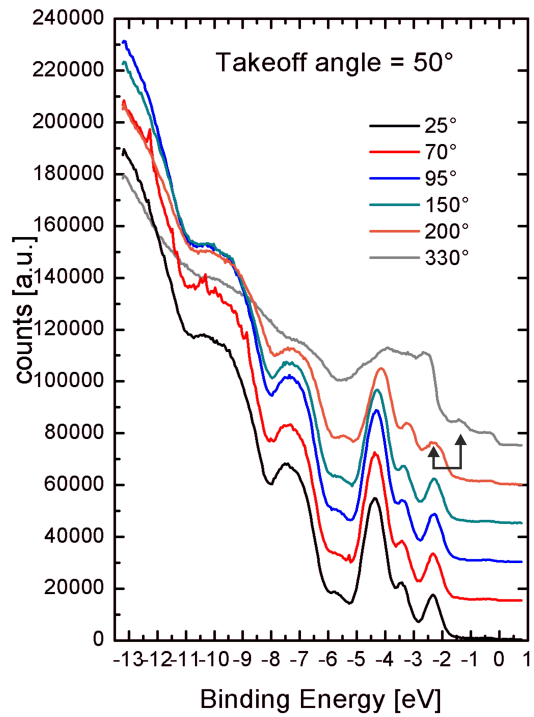


**Figure 61:** Determination of the work function and the thickness of the monolayer for Quinacridone on a Cu(110) surface. It converges exponentially against 3.8 eV. A thickness of 3.2 Å was observed.

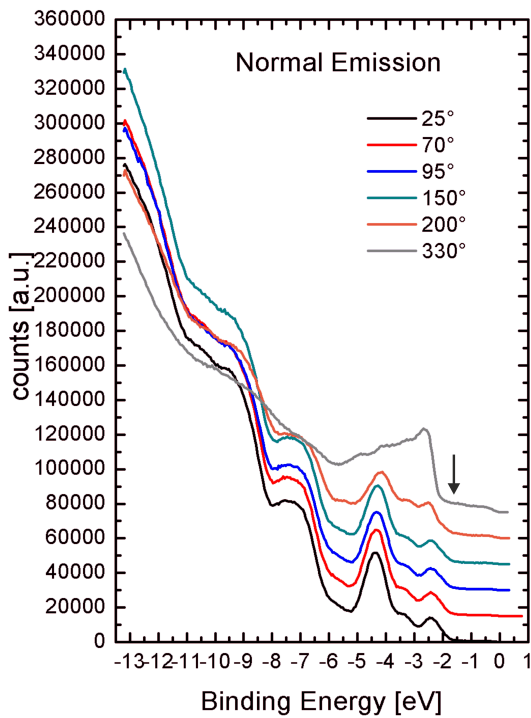
**Heating Series of a Multilayer Film** Heating series are in principal inverse dosing series. The starting point is always a multilayer film. After the film creation a couple of UPS spectra are taken at defined takeoff angles and the azimuth of interest. This measurement contains the takeoff angles normal emission,  $30^\circ$  and  $50^\circ$  along the [001] azimuth. The film was gradually heated and spectra were taken at every step. The results can be seen in figures 62c (NE), 62a ( $30^\circ$ ) and 62b ( $50^\circ$ ). The black line at the bottom of figure 62b arises from a  $18 \text{ \AA}$  thick film. This is the baseline of the experiment. Everything is aligned to the Fermi energy of copper at zero eV. By gradually heating the sample evaporation of the deposited Quinacridone film is expected. The first minor change in the spectrum can be found at  $200^\circ\text{C}$ . This change could be due to rearrangement of the deposited film. At some point between  $200^\circ\text{C}$  and  $330^\circ\text{C}$  evaporation of the multilayer happens. Every spectrum before the evaporation looked exactly like the spectrum of the bulk film from the previous dosing series (figure 60). The gray curve is very similar to a monolayer. The HOMO has shifted by a amount of  $0.8 \text{ eV}$ . This is exactly the inverse behavior of the evaporation from a mono- to a bi-layer or multilayer. Quinacridone is stable up to  $200^\circ\text{C}$  and most likely even higher. It evaporates at some point between  $200^\circ\text{C}$  and  $330^\circ\text{C}$  and therefore is thermal far more stable than its non hydrogen bonding analogon pentacene which evaporates below  $140^\circ\text{C}$ . The monolayer itself cannot be flashed off. The chemical bonding of Quinacridone to copper is so strong that sputtering is necessary to get rid of the monolayer. According to figure 62b the HOMO is strongest at a takeoff angle of  $50^\circ$  it is weaker at a takeoff angle of  $30^\circ$  (figure 62a) and it is not existent in normal emission (figure 62c).



(a) Heating series at a takeoff angle of  $30^\circ$ .



(b) Heating series at a takeoff angle of  $50^\circ$ .



(c) Heating series at normal emission.

**Figure 62:** Heating series of a  $18 \text{ \AA}$  thick film of Quinacridone on a Cu(110) substrate in the [001] azimuthal direction at three different takeoff angles:  $30^\circ$ ,  $50^\circ$  and normal emission. Different curves correspond to different heating steps. Starting at the bottom with  $25^\circ$  and increasing in temperature towards the top curve.<sup>78</sup>

**ARUPS Measurement of a Monolayer** Angle resolved ultraviolet photoemission spectroscopy was performed to gather more information about the electronic structure of a monolayer (3.2 Å). ARUPS was carried out in the [001] and the [1-10] azimuthal direction. An angle of 45° between the two substrate directions was covered as well. The takeoff angle was measured in the range from normal emission to 50° with an increment of 1°. Since the ARUPS looked messy, a specific selection of the taken spectra is shown in figure 63. These spectra combined with theoretical calculations (figure 64) gave information about the orientation of the molecules on the substrate surface. Figure 64 shows the momentum maps for the HOMO (left side) and the LUMO (right side). These maps were obtained out of density functional theory calculations. Momentum maps are cuts through the electronic structure at constant energy. The vertical direction is given by the momentum vector  $\vec{k}_y$  and the horizontal axis shows  $\vec{k}_x$ . The coloring corresponds to the emission intensity of the orbitals. Red represents the highest emission intensity, whereas blue stands for zero emission intensity. Every spectrum in figure 63 which is colored in blue was taken at a takeoff angle of 50°, everything in red was taken at a takeoff angle of 35° and everything in black corresponds to normal emission. By looking only on one color the top spectrum was taken along the [001] azimuth, the bottom spectrum was taken along the [1-10] and the spectrum in the center was taken exactly between the two substrate directions (45°). If the molecules are aligned with the long molecular axis close to the [001] direction and its short axis in the [1-10] then figure 64 is valid with the plotted coordinate system. Otherwise the coordinate system has to be rotated accordingly. Under the assumption made above, the momentum map of the HOMO (figure 64 left side) shows that the intensity of the HOMO should be the strongest in between the two substrate directions (45°). This behavior can be seen in figure 63 at a binding energy of -1.5 eV. The LUMO has the highest intensity (figure 64 right side) in the [001] substrate direction. This characteristic is in good agreement with the experiment. There is no HOMO and no LUMO visible in normal emission independent on the azimuthal directions, which also fits perfectly fine. This tells us that the molecules are aligned close to the [001] direction with their long molecular axis. It is very important to have very well ordered films in UPS measurements. More orientations of the molecules would lead to a superposition of the rotated calculations and no azimuthal behavior could be observed. To see if the experiment follows the intensity distribution of the simulation along the azimuthal directions equation 52 had to be used to calculate the parallel momentum. Takeoff angles of 50° are very close to the maxima (red zones) in the simulations. The highest experimentally measured intensities were around a takeoff angle of 50° for the HOMO and the LUMO. Figure 65 displays the wavefunction of the HOMO (right side) and LUMO (left side) in real space. The coloring reflects the sign of the wavefunction.

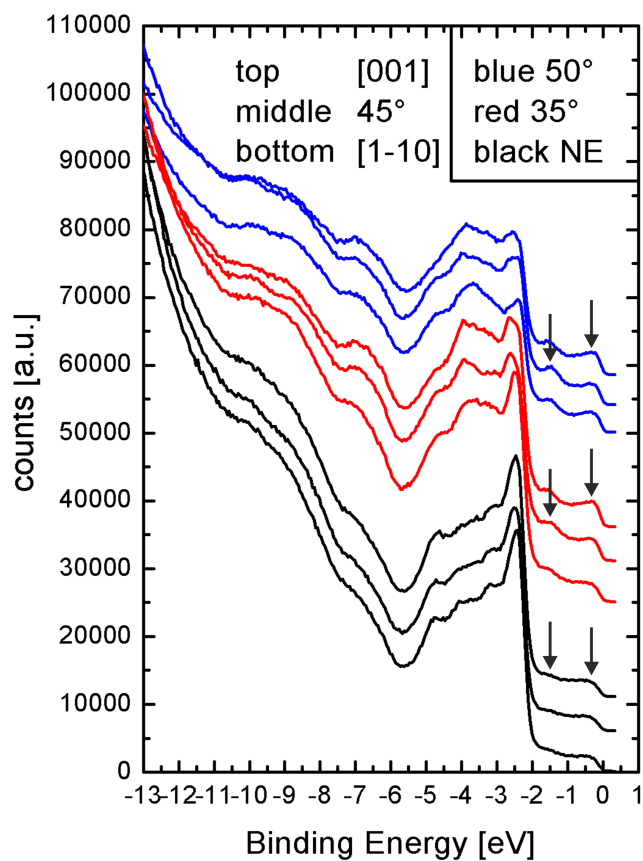


**Figure 63:** Selected spectra out of the ARUPS series on a monolayer of Quinacridone on a Cu(110) substrate. Different colors denote to different takeoff angles: blue 50°, red 35° and black normal emission. Considering only one color the top line corresponds to the [001] substrate direction, followed by 45° between the two azimuths and the bottom curve represents the [1-10] direction.

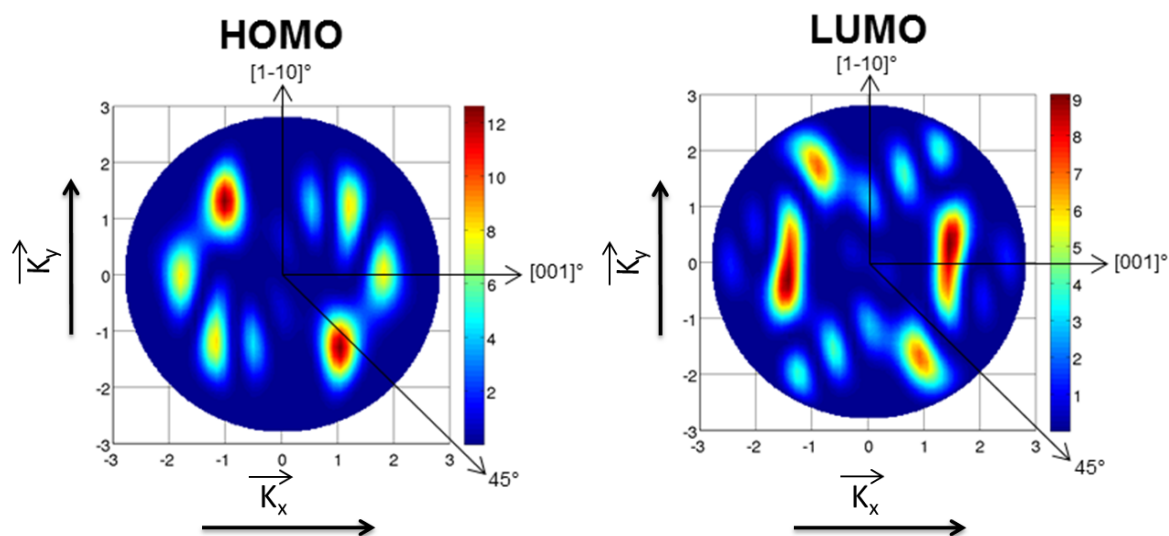


**Figure 64:** Theoretical calculations (density functional theory) for the momentum maps of an isolated Quinacridone molecule. The figure on the left side illustrates the momentum map of the HOMO, whereas the figure on the right side shows the momentum map of the LUMO. The coloring corresponds to the intensity.

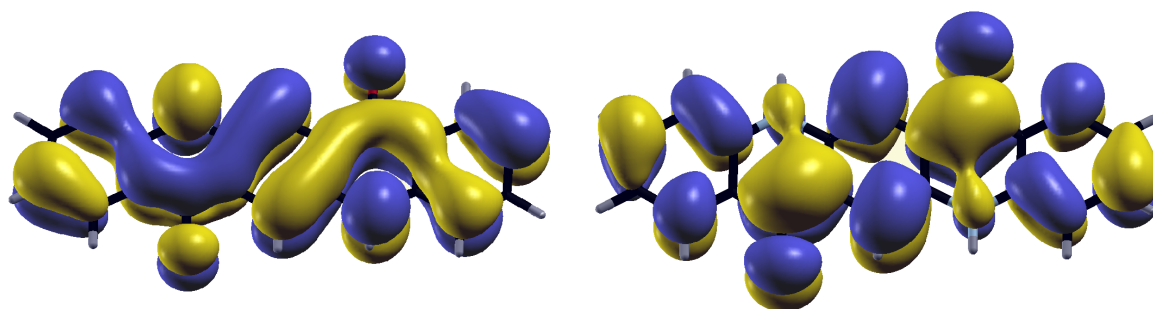


**Figure 65:** Theoretical calculations (density functional theory) for the wavefunctions of an isolated Quinacridone molecule. The left figure shows the wave function of the HOMO and the right part of the figure shows the wavefunction of the LUMO. The coloring corresponds to the sign of the wavefunction.

### 6.3.2 Experiments on Cu(110) at $T_S$ 140 °C

All samples investigated in this section were prepared at a substrate temperature of 140 °C during the evaporation process. The basic idea behind this was to introduce a certain amount of kinetic energy into the system to help the molecules align into their preferred orientation.

**Dosing Series** Figure 66 shows a dosing series starting from a monolayer of Quinacridone up to a 30 Å thick film. The left figure shows an uptake curve taken into the [001] substrate direction taken at a takeoff angle of 50°. The black line on the bottom is the monolayer. The LUMO is again visible at -0.2 eV. It disappears in the second layer as it should. That behavior is exactly the same as in figure 60 of evaporation at room temperature (section 6.3.1). The HOMO arises at a binding energy of -1.5 eV. All the peaks undergo a shift of -0.8 eV from the first to the second monolayer. This is exactly the same behavior as in the dosing series from section 6.3.1. However there is one major difference with increasing film thickness. The Fermi energy level is still visible in the bulk film. This was not the case for evaporation at room temperature. Additionally the monolayer HOMO is present in the bi-layer and multilayer system. This clearly shows that a nice layer by layer growth is not possible with Quinacridone on a Cu(110) surface at elevated temperature. There is very little azimuthal difference between the left and right image of figure 66. The HOMO and the LUMO are visible in the [001] direction and they both vanish along the [1-10] direction.

**ARUPS Measurement of a Monolayer** Figure 67 shows an ARUPS measurement of a monolayer in both azimuthal directions. The graph on the left side was measured along the [001] substrate direction and the graph on the right side was measured along the [1-10] azimuth. As in figure 66 there is very little difference in the azimuthal behavior of the ARUPS series. Looking at the left graph the HOMO shows a rather weak ARUPS behavior. It is not present in normal emission and at 10°. It appears around a takeoff angle of 20°. The HOMO decreases at 30° and starts to increase at 35° again. It stays visible up to 60°. The ARUPS measurements in the [1-10] directions show no HOMO and no LUMO at all (figure 67 right graph). However the LUMO is clearly visible along the [001] direction and it has a special ARUPS behavior. It increases in intensity at a takeoff angle of 30° up to 50° and decreases afterward.

**ARUPS Measurement of a Bi-layer** Figure 68 contains a ARUPS series of a 7 Å thick film along both azimuthal directions. The graph on the left side was measured along the [001] azimuth and the graph on the right side was measured along the [1-10] direction. At first glance both measurements look similar to each other and also very similar to the monolayer of figure 67. The most substantial difference is the orbital -5.3 eV. It has a very distinct angular and azimuthal behavior. The left graph displays that it is not present in normal emissions and appears at a takeoff angle close to 30°. It increases in intensity up to 40° until it is gone at a takeoff angle of 60°. The right graph shows a little different angular behavior. It is not present until a takeoff angle of 30° is reached, increases up to 35°, decreases and finally vanishes at 50°. The HOMO of the monolayer can be observed by very careful inspection along the [001] direction.

**ARUPS Measurement of a Multilayer** Figure 69 shows the ARUPS series of a 30 Å thick film of Quinacridone in both azimuthal directions. It looks shape wise very similar to the bi-layer in figure

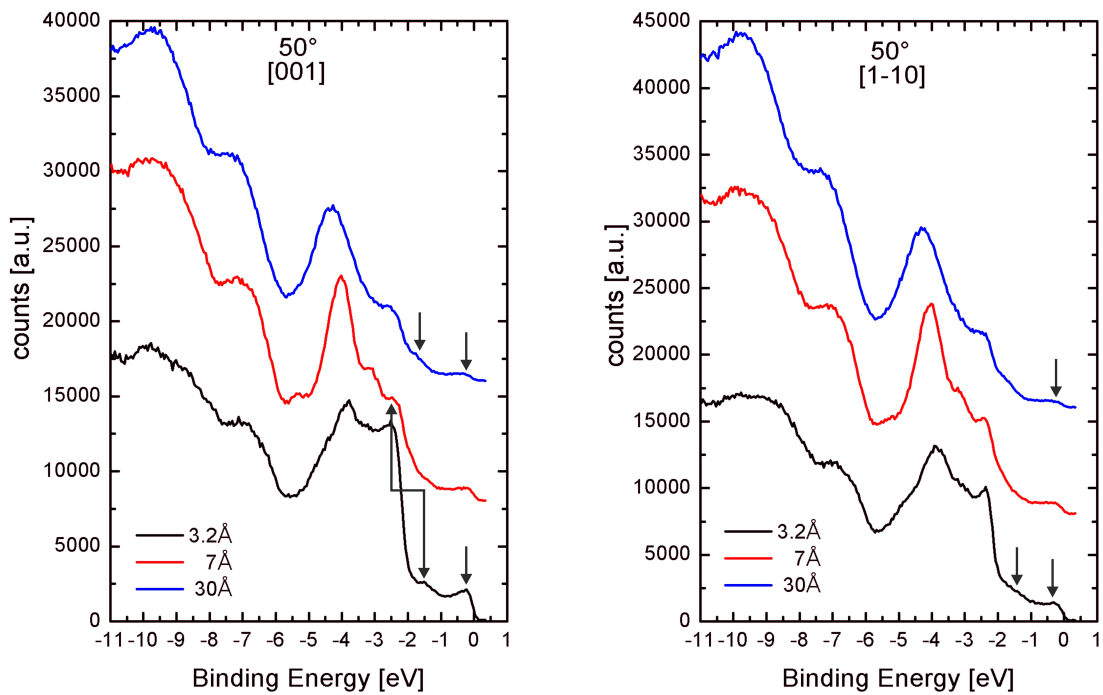


**Figure 66:** Uptake curve at elevated sample temperature ( $140^{\circ}\text{C}$ ) measured along both azimuthal directions at a fixed takeoff angle of  $50^{\circ}$ . The left figure shows the measurement along the  $[001]$  direction, whereas the right figure represents the measurement along the  $[1-10]$  direction. The bottom line is not clean copper. This dosing series started with a monolayer of Quinacridone evaporated onto the  $\text{Cu}(110)$  substrate while the temperature was hold constant at  $140^{\circ}\text{C}$ .

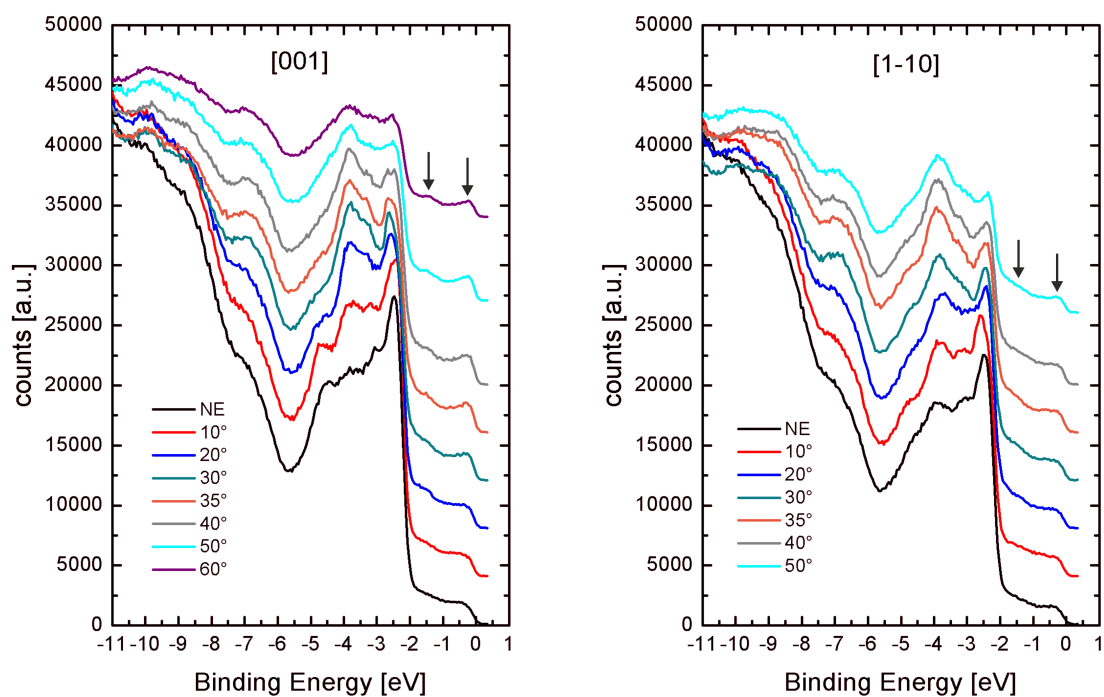


**Figure 67:** Angle resolved ultraviolet photoemission spectroscopy of a 3.2 Å thick film of Quinacridone on the Cu(110) surface. The left side shows the ARUPS in the [001] substrate direction and the right side illustrates the ARUPS along the [1-10] azimuth. The black line was taken at normal emission. Moving up the takeoff angle with respect to normal emission increases.

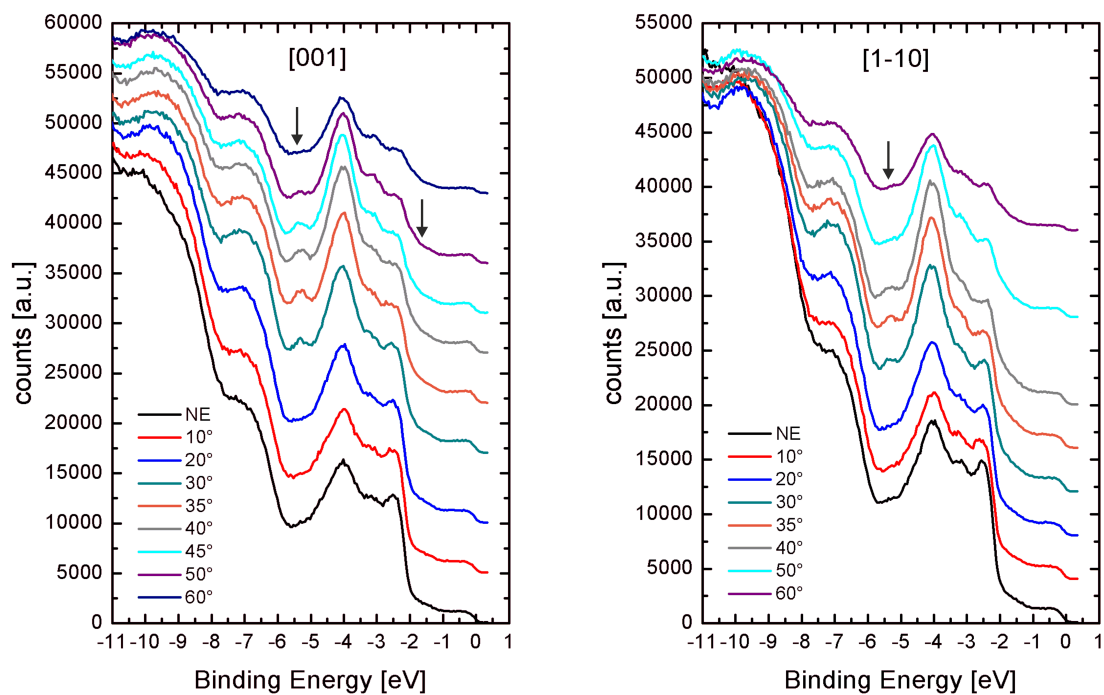


**Figure 68:** Angle resolved ultraviolet photoemission spectroscopy of a 7 Å thick film of Quinacridone on the Cu(110) surface. The left side shows the ARUPS in the [001] substrate direction and the right side illustrates the ARUPS along the [1-10] azimuth. Different colors denote to different takeoff angles.

68. All the orbitals have the same binding energy except the one at  $-5.3$  eV. It disappeared completely. Additionally the ARUPS of the  $[001]$  direction and the ARUPS of the  $[1-10]$  direction look nearly identical. The most important information contained in figure 69 is that the Fermi level of copper and the HOMO of the monolayer ( $-1.5$  eV) are still visible in the bulk. The only reasonable explanation for this is islanding. Ultraviolet photoemission spectroscopy is a surface sensitive technique. About a square millimeter of the sample gets illuminated and the detected signal is integrated. This means that if part clean copper, part monolayer and a bulk film is present in the illuminated area the resulting signal will be a superposition of their individual spectrum. That is in very good agreement with measurement given in figure 69. Elevated temperature is not preferable for the preparation of UPS samples, but it is great for preparing samples for x-ray diffraction experiments. Elevated temperature leads to bigger crystallites which is desirable for diffraction experiments.

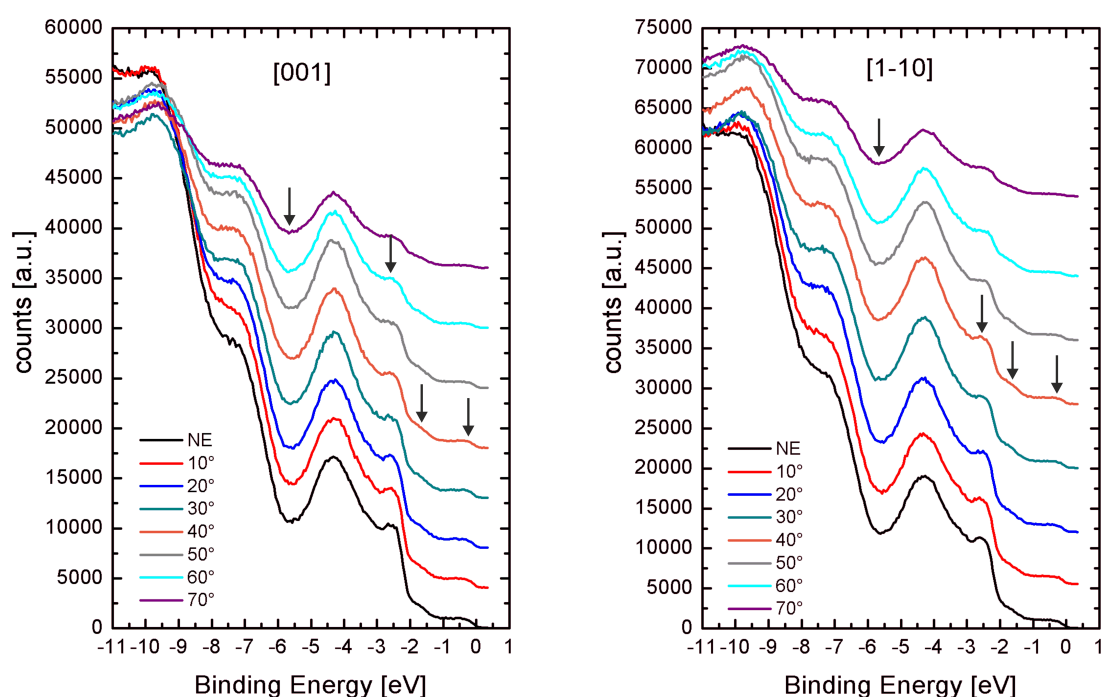
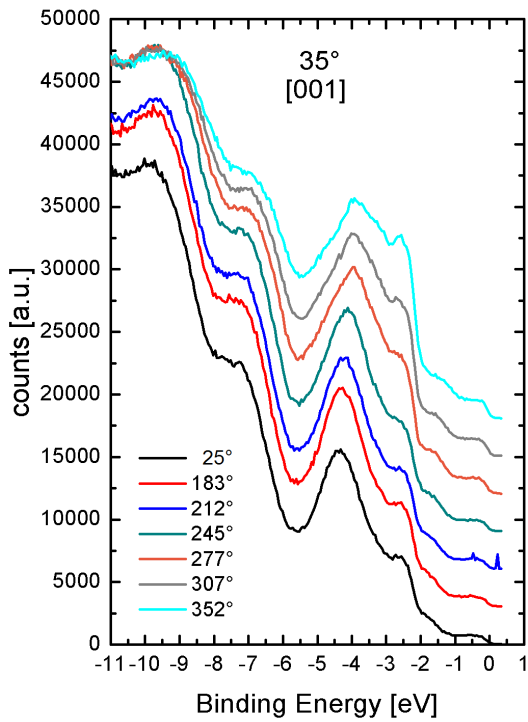


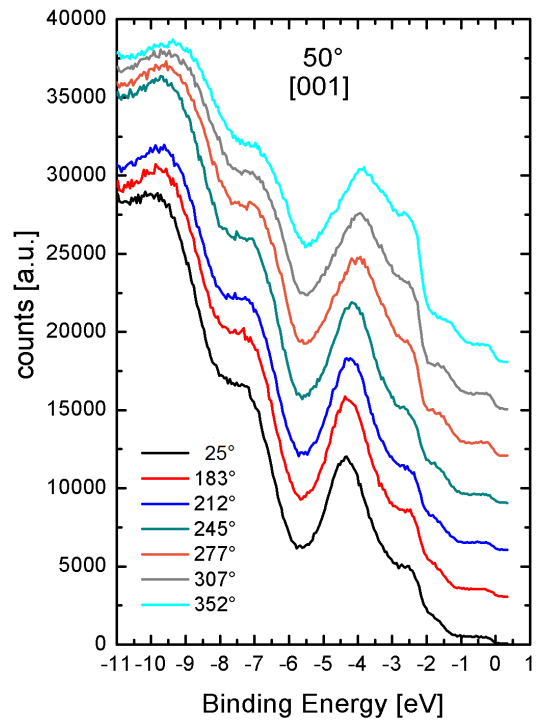
**Figure 69:** Angle resolved ultraviolet photoemission spectroscopy of a  $30 \text{ \AA}$  thick film of Quinacridone on a Cu(110) substrate (about 10 monolayer). The left side shows the ARUPS in the  $[001]$  substrate direction and the right side illustrates the ARUPS along the  $[1-10]$  azimuth. Different colors denote to different takeoff angles.

**Heating Series of a Multilayer** This heating series was performed different than the heating series in chapter 6.3.1. The applicable high voltage was used to heat up the sample. Illustration 70 shows a heating series from the  $30 \text{ \AA}$  thick film. The measurement series was carried out along the  $[001]$  azimuth and single spectrum were taken at three distinct takeoff angles, normal emission,  $35^\circ$  and  $50^\circ$ . The graph on the left side represents the spectra measured at a takeoff angle  $35^\circ$  (figure 70a). Graph 70b represents a takeoff angle of  $50^\circ$  and graph 70c accounts for normal emission. The bottom line of each graph was measured at room temperature ( $25^\circ\text{C}$ ). The first spectrum was taken at  $183^\circ\text{C}$ . Successive heating and measuring was done until a final temperature of  $352^\circ\text{C}$  was reached. One can clearly see the

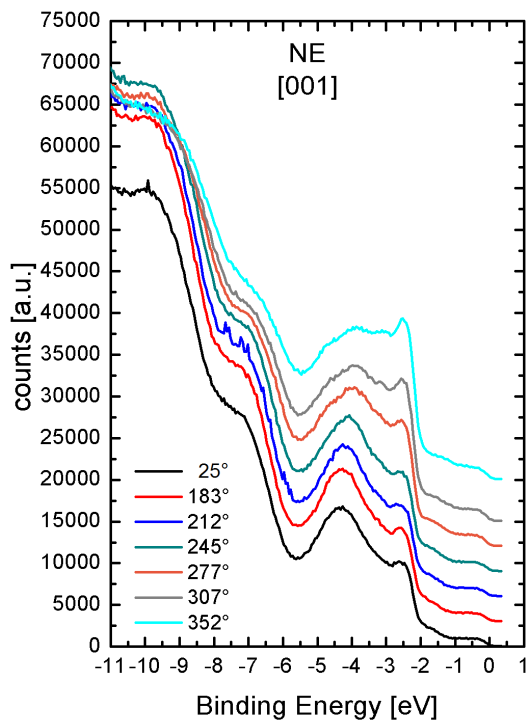
HOMO and the LUMO of the monolayer of Quinacridone getting stronger during the iterative procedure but the film looks even stable at 352 °C. This film is more stable than the film in the heating series in chapter 6.3.1. That is not the case. The heating experiment in chapter 6.3.1 was performed with slower heating and the copper crystal had more time to reach temperature. In this experiment the high voltage was used and the thermocouple showed the desired temperature quickly. The thermocouple was mounted very close to the copper crystal and not on the crystal itself. The heating for the sample should have been prolonged over time at constant temperature to give the sample the possibility to reach the desired temperature.



(a) Heating series at a takeoff angle of  $35^\circ$



(b) Heating series at a takeoff angle of  $50^\circ$



(c) Heating series at normal emission

**Figure 70:** Heating series of a  $30 \text{ \AA}$  thick film of Quinacridone on a Cu(110) surface at three different takeoff angles, along the [001] azimuth. The bottom line is the starting point and by moving up the temperature increases.

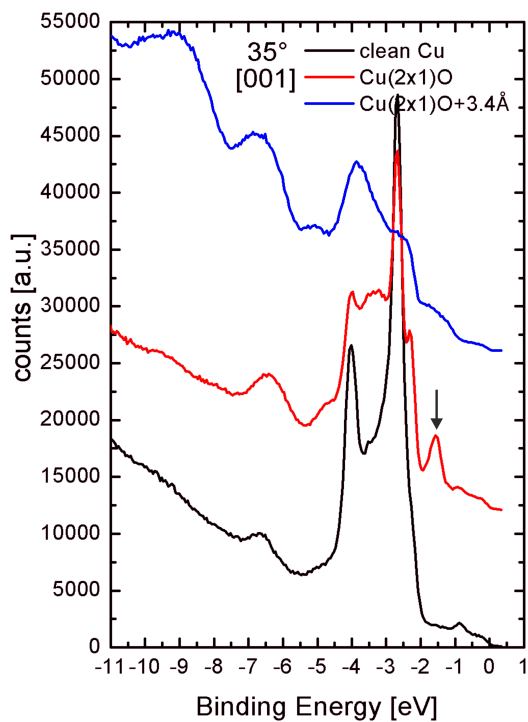
### 6.3.3 Experiments on a Cu(110)-(2x1)O at $T_S$ 25 °C

The strong interaction with copper is a problem for the determination of the electronic structure of Quinacridone, especially close to the d-band region. In order to minimize this influence a Cu(110)-(2x1)O reconstruction was used as a template for the atomically controlled growth. It provides a spatial separation from copper, a different chemistry and additionally a change in corrugation. The atomic rows of oxygen are perpendicular to the atomic rows of copper.

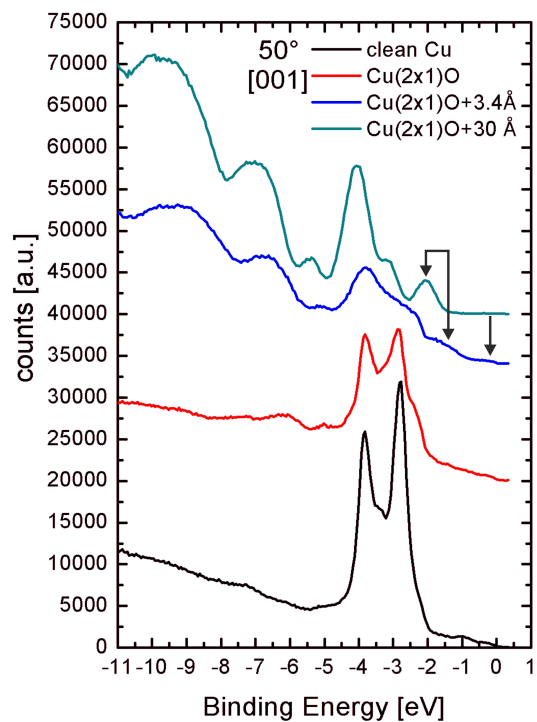
**Measurement of the Cu(110)-(2x1)O Template and a first Monolayer** Figure 71c shows spectra taken at normal emission along the [001] azimuth of a clean copper sample, a Cu(110)-(2x1)O reconstruction and a Cu(110)-(2x1)O + 3.4 Å of Quinacridone. The bottom line (black) is the spectrum of the clean Cu(110) surface. The red line corresponds the spectrum for the Cu(110)-(2x1)O reconstruction. It has a characteristic structure in the d-band region. A strong influence of the electronic structure of copper is still present. The blue line represents a monolayer of Quinacridone on a Cu(110)-(2x1)O reconstruction. The LUMO is no longer visible since there is no direct contact to copper. The curve on top (dark cyan) is from a 30 nm thick film of Quinacridone. It gives a clear view of how the electronic structure will look like at the given experimental parameters. The shift from monolayer to multilayer is smaller compared to the samples with direct copper contact. Its value is 0.46 eV, which is a little bit more than half the shift from section 6.3.1. Figure 71a contains the same measurements under a takeoff angle of 35 ° (left graph). A takeoff angle of 50 ° (right graph) is given in figure 71b. The most important detail in these graphs is the characteristic oxygen peak of the Cu(110)-(2x1)O reconstruction at a takeoff angle of 35 °. It is located at a binding energy of -1.5 eV. Figures 71c, 71a and 71b are shown to give a basic view of the clean substrate, the Cu(110)-(2x1)O reconstruction (the new substrate), a monolayer and a bulk film of Quinacridone on the new template for the film growth. The work functions and ionization potentials (IP) are as following:

- $\phi_{Cu}$  : 4.38 eV
- $\phi_{Cu(110)-(2x1)O}$  : 4.74 eV
- $\phi_{Cu(110)-(2x1)O+3.4\text{\AA}}$  : 4.22 eV
- $\phi_{Cu(110)-(2x1)O+30\text{\AA}}$  : 4.26 eV
- $IP_{Cu(110)-(2x1)O+3.4\text{\AA}}$  : 5.8 eV
- $IP_{Cu(110)-(2x1)O+30\text{\AA}}$  : 6.3 eV

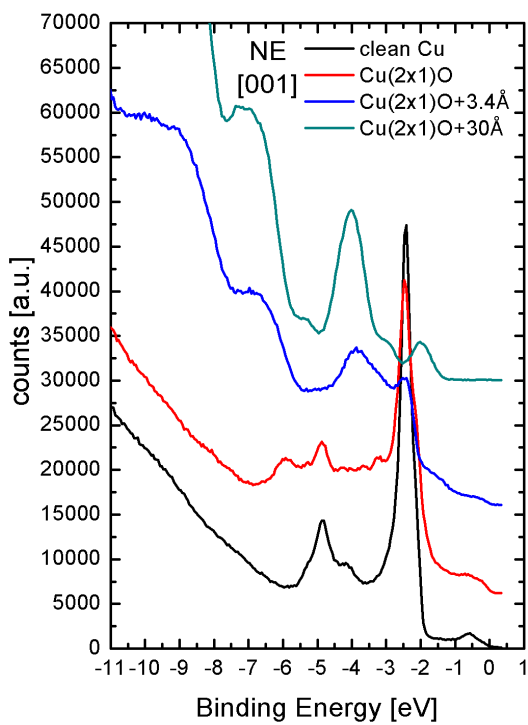
**ARUPS on a Monolayer of Quinacridone** Illustration 72 shows an ARUPS series of a 3.4 Å thick film of Quinacridone along both azimuthal directions and 45 ° in between. All measurement series seem very well defined. The graph on the top left side corresponds to the ARUPS measurement along the [001] substrate direction (figure 72a). It has an orbital with strong angular dependence at a binding energy of -5 eV. This orbital is not present before a takeoff angle of 30 °, afterwards it increases in intensity up to an angle of 30 ° and starts to decrease again until it vanishes completely at 60 °. This orbital has a very well defined angular behavior. As later measurements show, it will be of great importance. This orbital has additionally a strong azimuthal behavior as well. It is not present along the [1-10] direction (figure



(a) Takeoff angle  $30^\circ$



(b) Takeoff angle  $50^\circ$

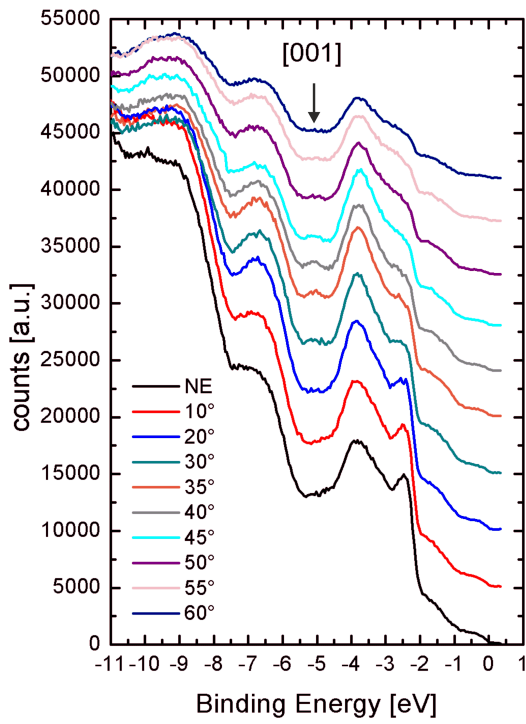


(c) Takeoff angle normal emission

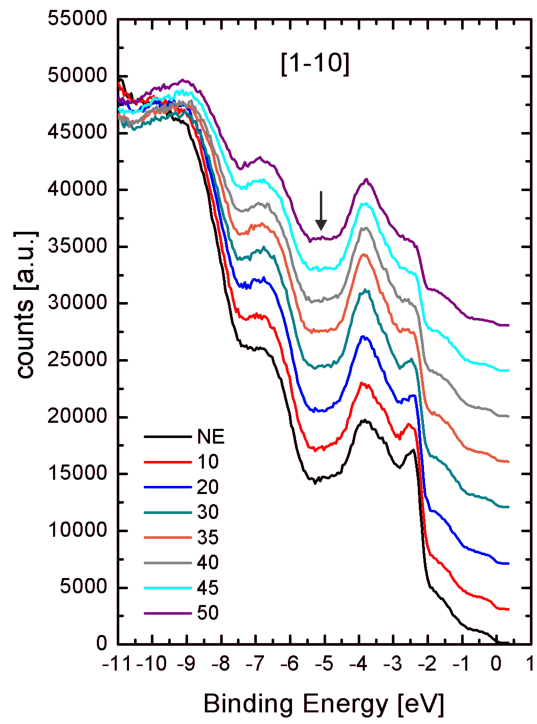
**Figure 71:** UPS measurement of clean copper (black), a Cu(110)-(2x1)O reconstruction (red), a Cu(110)-(2x1)O reconstruction with 3.4 Å of Quinacridone (blue) and a Cu(110)-(2x1)O reconstruction with 30 Å of Quinacridone (dark cyan). The measurements were carried out in the [001] azimuth at three different takeoff angles.

72b) and cannot be seen  $45^\circ$  in between (figure 72c). This lets us conclude that the monolayer on the Cu(110)-(2x1)O template is very well ordered.

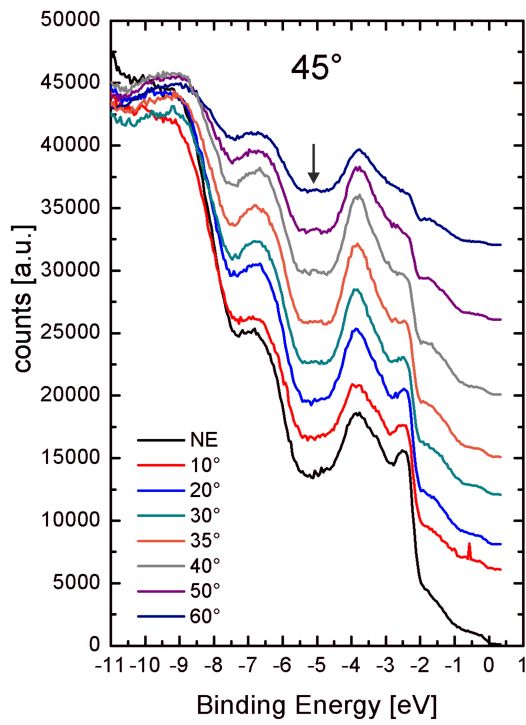
**ARUPS on a 30 nm thick film of Quinacridone** Figure 73 illustrates an ARUPS series in both azimuthal directions on a 30 nm thick film of Quinacridone on a Cu(110)-(2x1)O substrate. This is the same film used as in the x-ray diffraction experiments from chapter 6.2.3. The ARUPS series shown in figure 73 looks extremely similar to the ARUPS of the monolayer in figure 72. It has an orbital at a binding energy of -5.4 eV (-0.4 eV shift from the monolayer to multilayer) with an extremely strong angular behavior. This orbital also has very distinct azimuthal behavior. Both measurement series seem very well defined and the strong similarity to the monolayer ARUPS allows the conclusion that Quinacridone follows on a Cu(110)-(2x1)O template after evaporation at  $T_S$  25 °C a well ordered layer by layer growth. This mysterious orbital could be identified with the help of theoretical calculations performed by Daniel Lueftner of the university of Graz. It turns out that the orbital at -5.4 eV is the HOMO-9. It can be seen in figure 74. The picture on the left side shows the wavefunction of the HOMO-9 orbital in real space. The coloring is directly related to the sign of the wavefunction. The picture on the right side shows a momentum map of the HOMO-9. The coloring accounts for the emission intensity. Assuming that a molecule lies with its long molecular axis in the [001] direction of copper and its short axis is aligned with the [1-10] azimuth then the plotted coordinates system is valid. The momentum map tells us how the intensity of the HOMO-9 changes along the substrate directions. That can be directly confirmed with the experimental data (figure 73) and the use of equation 52. It turns out that the angular change in intensity in figure 73 follows the intensity pattern of the calculation very closely. All this information together allows the conclusion that the molecules are all aligned close to the [001] direction of copper. The same result for this film was obtained in the x-ray diffraction chapter 6.2.3. The only odd thing about the ARUPS series in figure 73 is that the HOMO itself has extremely weak angular and azimuthal behavior. Usually the behavior of the HOMO is expected to be more like the behavior of the HOMO-9. In this case we got lucky and were able to measure the HOMO-9 and consequently compare it to theoretical calculations. The electronic structure of the  $\alpha$  phase was pretty similar to the structure of the  $\beta$  phase. The major difference was the distinctness of the ARUPS of the  $\alpha$  phase. This distinctness originated in the orientation of the molecules. The  $\alpha$  phase had only molecules close to the [001] direction and therefore a clear spectrum with strong angular and azimuthal behavior. The  $\beta$  phase had more then one orientation of the molecules and that resulted in a spectrum compare able to a density of states.



(a) [001]



(b) [1-10]



(c) 45°

**Figure 72:** Angle resolved ultraviolet photoemission spectroscopy of a monolayer of Quinacridone on a Cu(110)-(2x1)O reconstruction in both azimuthal directions and 45°C in between. The coloring is related to different takeoff angles.

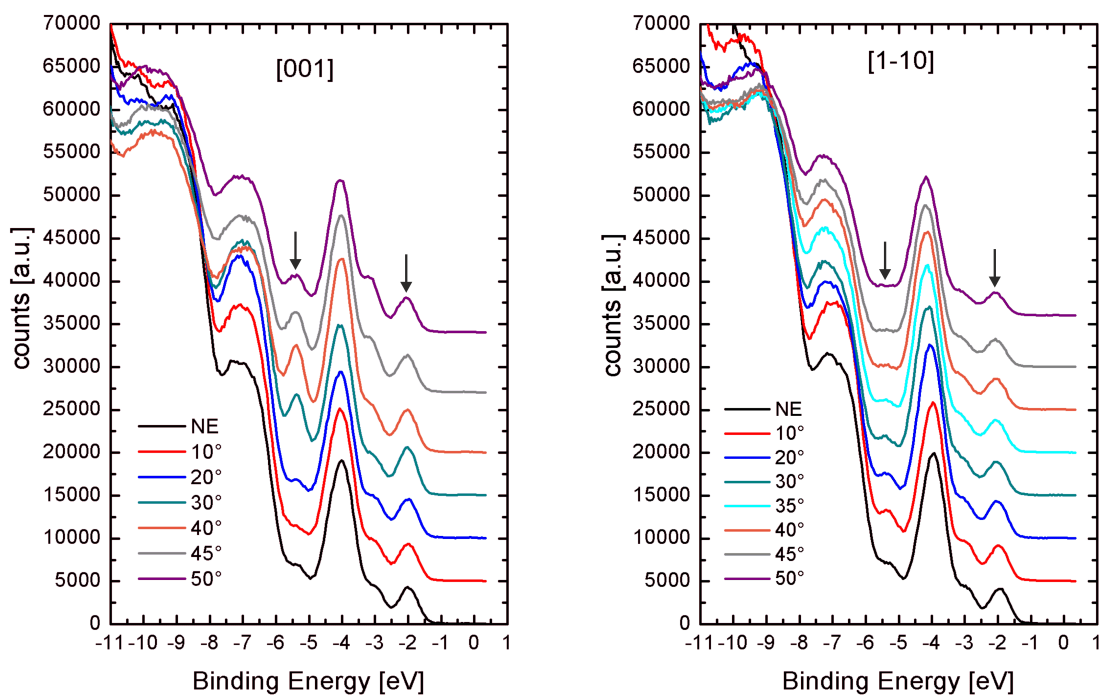


**Figure 73:** Angle resolved ultraviolet photoemission spectroscopy of a 30 nm thick film of Quinacridone on a Cu(110)-(2x1)O reconstruction as template for the growth. The left side shows an ARUPS series in the [001] azimuth. The graph on the right side illustrates an ARUPS series in [1-10] direction. The coloring is related to different takeoff angles.

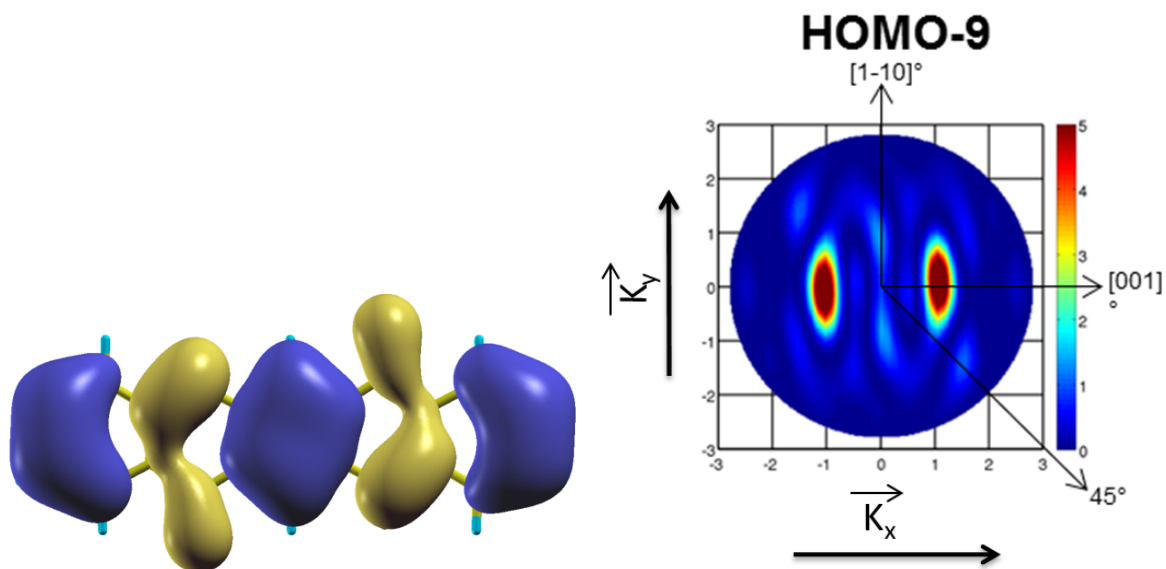


**Figure 74:** Density functional theory calculations with the GGA functional for the wavefunction and the momentum map of the HOMO-9. The left side shows the wavefunction of the HOMO-9 in real space and the coloring takes account for the sign of the wavefunction. The right side shows a momentum map of the HOMO-9. These calculations were performed by Daniel Lueftner.

## 7 Conclusion

**X-ray Diffraction Experiments** were performed on Quinacridone ( $C_{20}H_{12}N_2O_2$ ) thick films. They were grown on a Cu(110) surface and the Cu(110)-(2x1)O reconstruction. Sample 1 was a 27.4 nm thick film on the Cu(110) template. The substrate was held at room temperature during the deposition process. Polefigure measurements showed that this sample had the crystalline  $\beta$  phase with the (-112) plane parallel to the substrate surface. The molecules were inclined to both substrate directions and they oriented entirely flat on the substrate surface. Sample 2 was a 21.4 nm thick film on the Cu(110) substrate. Evaporation was performed at an elevated substrate temperature of 140 °C. The x-ray characterization showed a clear  $\alpha$  phase with the (1-12) plane parallel to the substrate surface. Sample number 3 had the Cu(110)-(2x1)O reconstruction as substrate and the evaporation process was carried out while the substrate was at room temperature. The Quinacridone film was 30 nm thick and the x-ray diffraction measurements revealed an  $\alpha$  phase with the (1-12) plane parallel to the surface. Every molecule in the  $\alpha$  phase was aligned close to the [001] substrate direction. That allows the conclusion that on a copper substrate the molecules lay across the atomic rows, whereas they were aligned along the oxygen rows on the Cu(110)-(2x1) reconstruction. The molecules were not entirely flat on the substrate surface, there was always a little tilt angle present. The rocking curve measurements showed that both  $\alpha$  phases had less mosaicity than the  $\beta$  phase. The full width at half maximum of the samples 1, 2 and 3 were 6.7 °, 2.2 ° and 3.7 °, respectively.

**Ultraviolet Photoemission Spectroscopy** was performed on various dosing series of Quinacridone leading to the workfunction  $\phi$  of the monolayer, the ionization potential of a monolayer and a multilayer as well as the thickness of the monolayer itself. These values were obtained from samples where the sample temperature was at room temperature during the evaporation process and the Cu(110) substrate was used. The monolayer had a thickness of 3.2 Å and the corresponding workfunction was  $\phi_{Cu+Mono} = 3.8$  eV. The ionization potential of the monolayer was 5.4 eV and it increased to 6.1 eV in the multilayer. A characteristic shift of 0.8 eV of the electronic structure from the monolayer to the multilayer could be observed. This shift originated from the weaker screening of the positive photo hole in the photo excitation process in the outer layers of the film (starting at the second layer). Additionally the LUMO was visible in the monolayer at a binding energy of 0.2 eV. The LUMO was occupied with electrons due to a chemical bond of Quinacridone with the copper atoms of the substrate surface. Thermal stability measurements showed that Quinacridone films are stable up to 200 °C. Evaporation of the multilayer started somewhere between 200 °C and 330 °C. ARUPS measurements of a monolayer in both azimuthal directions in combination with theoretical calculations gave a good hint about the orientation of the molecules on the substrate surface. They were all aligned close to the [001] direction with their long molecular axis. Measurements after sample preparation at elevated substrate (Cu(110)) temperature showed clearly that Quinacridone undergoes islanding at these experimental conditions. The Fermi edge and the HOMO of the monolayer were visible in the UPS spectrum of a 30 Å thick film.

In order to reduce the strong interactions of copper with Quinacridone a second template for the growth was chosen. The Cu(110)-(2x1)O reconstruction is an atomically controlled substrate which has a change in corrugation by 90 ° and a different chemistry. The workfunction of a monolayer turned out to be 4.22 eV. The corresponding ionization potential had a value of 5.8 eV. The multilayer showed an ionization potential of 6.3 eV. The most important result of the UPS section could be obtained from the ARUPS measurements of a monolayer of Quinacridone and a multilayer (30 nm thick film) on the Cu(110)-(2x1)O reconstruction. Their similarity and their well defined electronic structure were a consequence of layer

by layer growth. The combination of those measurements with theoretical calculations of the HOMO-9 (section 6.3.3, figures 72a, 72b, 73, and 74) led to the orientation of the molecules in the bulk film. All the molecules were aligned with their long molecular axis close to the [001] direction of copper. This is in excellent agreement with the x-ray diffraction characterization of the same film.

## 8 Table-, Picture- and Literature glossary

### List of Tables

1	Summary of the intermolecular forces responsible for crystal formation.[25] . . . . .	10
2	The classification of hydrogen bonds into strong, moderate and weak bonds. [8] . . . . .	12
3	Point and space groups of Bravais lattices and crystal structures. [22] . . . . .	15
4	Crystalline structure parameters of Cu(110) and important parameters.[3, 6, 24] . . . . .	39
5	The three well known crystalline structures of Quinacridone, namely the $\alpha$ , $\beta$ and $\gamma$ phase. a, b, and c are the length of the unit cell vectors and the corresponding angle are $\alpha$ , $\beta$ and $\gamma$ . Z is the amount of molecules in the unit cell.[9] . . . . .	42
6	Experimental parameters of the Siemens D501 Krystalloflex for the powder measurement of Quinacridone. . . . .	45
7	Sample 1 : cleaning parameters of the substrate prior to preparation of the Quinacridone film. In the case of flashing or annealing voltage stands for the filament heating voltage and the current corresponds to the filament current. Temperature is the sample temperature and high voltage is the applied high voltage to accelerate the electrons from the heating filament towards the sample. In the case of a sputtering process current stands for the filament current and the high voltage is the acceleration voltage for argon ions. . . . .	49
8	Experimental parameters for the x-ray diffraction measurements of a 27.4 nm thick film of Quinacridone on a Cu(110) substrate using the Phillips X'Pert four circle Texture Goniometer. The collimator defines the aperture at the side of the x-ray source and detector aperture specifies the aperture on the detector side, followed by the beam mask. . . . .	49
9	Relevant peaks of the $\beta$ phase close to the experimentally observed peak at $41.1^\circ$ of a 27.4 nm thick film of Quinacridone on a Cu(110) substrate (sample 1). . . . .	50
10	Enhanced pole densities calculated by stereopole for a 27.4 nm thick film of Quinacridone on a Cu(110) substrate (sample 1). The corresponding polefigure (figure 41) was measured at $2\theta = 41.57^\circ$ . Cu(100) refers to the substrate spots and 5Q represents the $\beta$ phase of Quinacridone with the (-112) plane parallel to the substrate surface. The numbers 1, 2, 3 and 4 refer to specific calculations where 1 corresponds to blue coloring, 2 to green, 3 to orange and 4 to pink. . . . .	53
11	Inclined angles between the copper [001] direction and the long molecular axis of the molecules of a 27.4 nm thick film of Quinacridone on a Cu(110) substrate (sample 1). The crystallite number refers to one specific orientation which has a specific coloring in the polefigures. The column figure stands for the figure number of corresponding models. . . . .	55
12	Sample 2: cleaning parameters of the substrate prior to preparation of the Quinacridone film. In the case of flashing or annealing voltage stands for the filament heating voltage and the current corresponds to the filament current. Temperature is the sample temperature and high voltage is the applied high voltage to accelerate the electrons from the heating filament towards the sample. In the case of a sputtering process current stands for the filament current and the high voltage is the acceleration voltage for argon ions. . . . .	56
13	Experimental parameters for the x-ray diffraction measurements of a 21.4 nm thick film of Quinacridone on a Cu(110) substrate using the Phillips X'Pert four circle Texture Goniometer. The collimator defines the aperture at the side of the x-ray source and detector aperture specifies the aperture on the detector side, followed by the beam mask. . . . .	56

14	Relevant peak of the $\alpha$ phase close to the experimentally observed peak at $42.5^\circ$ of a 21.4 nm thick film of Quinacridone on a Cu(110) substrate (sample 2). . . . .	57
15	Enhanced pole densities calculated by stereopole for a 21.4 nm thick film of Quinacridone on a Cu(110) substrate (sample 2). The corresponding polefigure (figure 47) was measured at $2\theta = 38.72^\circ$ . Cu(100) refers to the substrate spots and 5Q represents the $\alpha$ phase of Quinacridone with the (1-12) plane parallel to the substrate surface. The numbers 1, 2, 3 and 4 refer to specific calculations where 1 corresponds to blue coloring, 2 to green, 3 to orange and 4 to pink. . . . .	60
16	Inclined angle between the copper [001] direction and the long molecular axis of the molecules of a 21.4 nm thick film of Quinacridone on a Cu(110) substrate (sample 2). The crystallite number refers to one specific orientation which has a specific coloring in the polefigures. The column figure stands for the figure number of corresponding models. . . . .	60
17	Sample 3 : cleaning parameters of the substrate prior to preparation of the Quinacridone film. In the case of flashing or annealing voltage stands for the filament heating voltage and the current corresponds to the filament current. Temperature is the sample temperature and high voltage is the applied high voltage to accelerate the electrons from the heating filament towards the sample. In the case of a sputtering process current stands for the filament current and the high voltage is the acceleration voltage for argon ions. . . . .	62
18	Experimental parameters for the x-ray diffraction measurements of a 30 nm thick film of Quinacridone on a Cu(110)-(2x1)O reconstruction using the Phillips X'Pert four circle Texture Goniometer. The collimator defines the aperture at the side of the x-ray source and detector aperture specifies the aperture on the detector side, followed by the beam mask. . . . .	63
19	Relevant peaks of the $\alpha$ phase close to the experimental measured peaks at $42.16^\circ$ and $38.6^\circ$ of a 30 nm thick film of Quinacridone on a Cu(110)-(2x1)O reconstruction (sample 3). . . . .	64
20	Inclined angles between the copper [001] direction and the long molecular axis of the molecules of a 30 nm thick film of Quinacridone on a Cu(110)-(2x1)O reconstruction (sample 3). The crystallite number refers to one specific orientation which has a specific coloring in the polefigures. The column figure stands for the figure number of corresponding models. . . . .	66
21	Enhanced pole densities calculated by stereopole for a 30 nm thick film of Quinacridone on a Cu(110) substrate (sample 3). The corresponding polefigure (figure 53) was measured at $2\theta = 21.02^\circ$ . Cu(100) refers to the substrate spots and 5Q represents the $\alpha$ phase of Quinacridone with the (1-11) plane parallel to the substrate surface. The numbers 1, 2, 3 and 4 refer to specific calculations where 1 corresponds to blue coloring, 2 to green, 3 to orange and 4 to pink. . . . .	67
22	Inclined angles between the copper [001] direction and the long molecular axis of the molecules of a 30 nm thick film of Quinacridone on a Cu(110)-(2x1)O reconstruction (sample 3). The crystallite number refers to one specific orientation which has a specific coloring in the polefigures. The column figure stands for the figure number of corresponding models. . . . .	67
23	Enhanced pole densities calculated by stereopole for a 30 nm thick film of Quinacridone on a Cu(110) substrate (sample 3). The corresponding polefigure (figure 54) was measured at $2\theta = 38.72^\circ$ . Cu(100) refers to the substrate spots and 5Q represents the $\alpha$ phase of Quinacridone with the (1-12) plane parallel to the substrate surface. The numbers 1, 2, 3 and 4 refer to specific calculations where 1 corresponds to blue coloring, 2 to green, 3 to orange and 4 to pink. . . . .	69

24 Experimental parameters for the growth of Quinacridone (5Q) on Cu(110) and Cu(110)-(2x1)O. Heating voltage and heating current are the applied voltage and the measured current at the button heater. Three different sets for the heating parameters are given, since three different evaporators were used. This is accounted for with the numbers 1, 2 and 3. . . . . 73

## List of Figures

1	The left side shows pentacene ( $C_{22}H_{14}$ ). It has a full intramolecular $\pi$ -conjugation. This conjugation is broken in Quinacridone due to the change of atoms. The right side displays a single Quinacridone ( $C_{20}H_{12}N_2O_2$ ) molecule. The coloring is as follows: grey... carbon, white... hydrogen, red... oxygen, blue... nitrogen . . . . .	7
2	Schematic of hydrogen bonding in water. O... oxygen, H... hydrogen and $\delta^\pm$ describes the partial charge of the atom. [25] . . . . .	12
3	The crystal structure is build by a convolution of the basis with the Bravais lattice. (a) shows a squared Bravais lattice. (b) is a basis with two different atoms, and the resulting crystal structure is depicted in (c). . . . .	13
4	A two dimensional Bravais lattice with three different choices for the translation vectors $\vec{a}_i$ of the lattice. The vectors $\vec{a}_1$ , $\vec{a}_2$ , $\vec{a}'_1$ and $\vec{a}'_2$ are primitive lattice vectors. Any point of the lattice fulfills equation 5 with these vectors. The area of the parallelograms 1 and 2 are the same and they could be taken as a primitive cell. The lattice vectors $\vec{a}''_1$ and $\vec{a}''_2$ are no primitive translation vectors and therefore the area of the parallelogram 3 differs from the area of the parallelograms 1 and 2. . . . .	13
5	Schematic for the derivation of the Miller indices. . . . .	14
6	Bragg diffraction on a set of parallel atomic planes. $\vec{k}$ is the wavevector of the incoming x-ray radiation, $\vec{k}'$ is the wavevector of the outgoing radiation. $\theta$ is the angle between the wavevector and the net planes. $d$ is the netplane distance and $2d \sin \theta$ is the path difference.	17
7	Schematic for the derivation of the scattered radiation from the target to a point of interest B. Q is the position of the radiation source. P is the point where the scattering happens and B is the point of interest.[12] . . . . .	18
8	Ewald construction for elastic scattering with the incoming wavevector $\vec{k}_0$ , the outgoing wavevector $\vec{k}$ and the reciprocal lattice vectors $\vec{G}$ . . . . .	21
9	The Philips XPERT four circle texture goniometer [26]. It was used in this work for specular scans, rocking curves and polefigure measurements. . . . .	23
10	Schematic of the diffraction geometry in a specular scan. $\vec{k}_0$ is the incoming wavevector, $\vec{k}_1$ is the outgoing wavevector and $\vec{q}$ accounts for the scattering vector. . . . .	23
11	Ewald construction for the $\theta/2\theta$ scan geometry. $\vec{k}_0$ and $\vec{k}_1$ are the wavevectors of the incoming and outgoing radiation. $\vec{k}_0$ is pointing towards the origin in reciprocal space and the dotted lines display the situation after some steps in a $\theta/2\theta$ scan. As one can see $\vec{q}$ changes only in magnitude not in direction. . . . .	24
12	Specimen: different crystallite orientations on top of the substrate. The normal vector of each crystallite is given by $\vec{n}$ . $\vec{q}$ stands for the scattering vector. [2] . . . . .	24
13	Basic principal of a rocking curve measurement in reciprocal space by making use of the Ewald construction. $\vec{k}_0$ is the incoming radiation and $\vec{k}_1$ are the diffracted x-rays. $\vec{k}_0$ is pointing towards the origin in reciprocal space. The scattered lines display the situation after a couple of tilts. The scattering vector changes perpendicularly to the direction of change in a specular scan. . . . .	25
14	Scheme of a polefigure measurement. Every point in the polefigure has its own unique tuple $(\psi, \phi)$ . [2] . . . . .	26
15	Diffraction geometry for a polefigure measurement at a specific $2\theta$ peak. A clear view of the limiting aperture in front of the detector is given. The grey oval is the probed volume at specific point in reciprocal space. [26] . . . . .	26

16	The volume mapped in reciprocal space by a single polefigure is a half sphere shell. The thickness of the shell is defined by the beam broadening and the acceptance angle of the detector (defined by the receiving slit)[26] . . . . .	27
17	Example of a polefigure measured at $2\theta = 41.197$ which corresponds to the (1-12) plane of the $\alpha$ phase. The angle $\psi$ goes into the radial direction. From one circle to another there are always $10^\circ$ steps even if the spacing gets wider with increasing radius. $\phi$ goes along the circumference from $0^\circ$ to $360^\circ$ . . . . .	27
18	Geometry of an ARUPS experiment. The incoming radiation has the energy $\hbar\omega$ . $\alpha$ determines the angle of incidence and $\theta$ is the the takeoff angle. $\phi$ describes the inplane rotation. The gray shaded area is the scattering plane defined by the incoming wavevector, the outgoing wavevector and the scattering vector. [21] . . . . .	29
19	Schematic of the electronic excitation process in a semiconductor. Only vertical transitions are taken into account. $E_F$ is the energy reference level (Fermi energy). The energy of the final state $E_f$ and the initial state $E_i$ are given with respect to $E_F$ . [21] . . . . .	29
20	Schematic for the transmission of the emitted electron through the surface and conservation of the momentum parallel to the surface. [21] . . . . .	30
21	Siemens D501 Crystalloflex powder diffractometer. The x-ray tube is on the left side (1). It emits Cu $K_\alpha$ radiation. (2) and (3) are the positions of the aperture at the primary side. The sample is mounted on (4). (5), (7) and (9) are the aperture at the secondary side. A filter can be used in position (6). The incoming beam from (1) gets diffracted at the sample (4) and passes the monochromator (8) which is in front of the detector (10). The whole systems uses Bragg-Brentano focusing. . . . .	35
22	Phillips X'Pert four circle texture goniometer. On the primary side is the x-ray tube (1) emitting Cr $K_\alpha$ radiation. (2) is the position of the collimator. The sample is mounted on the holder (3) which is able to rotate in three directions. The aperture on the secondary side is placed on (4), (5) is the monochromator and (6) is the detector. . . . .	36
23	Schematic of the ADES 400 Spectrometer: DP... diffusion pump, V... valve, GEL... gas discharge lamp, AA... air admit, GHL... gas handling line, GI... gas inlet (for HE lamp), HP... helium purifier, AR... argon inlet, RV... roughing valve, RP... roughing purifier [28]	37
24	Side view of the ADES 400 Spectrometer . . . . .	38
25	Manipulator head with a mounted crystal in the center. The handle bars are for the wobble stick to rotate the azimuth of the sample. The wobble stick can be seen on the left side and the microbalance on the right side. The shutter for the LEED optic can be seen in the background.[28] . . . . .	38
26	Face centered cubic lattice of copper [6]. The plane indicated in gray is the (110) plane. .	39
27	A clean Cu(110) surface is shown on the left side. The right side shows a partial Cu(110)-(2x1)O reconstruction. The grey atoms are copper atoms and the black dots are the oxygen atoms. . . . .	40
28	Model of the $\alpha$ phase of Quinacridone with a view in the $[1\bar{1}2]$ direction. . . . .	42
29	Model of the $\alpha$ phase of Quinacridone with a view along the long molecular axis. . . . .	42
30	Model of the $\beta$ phase of Quinacridone with a view close to the long molecular axis. . . . .	43
31	Model of the $\beta$ phase of Quinacridone with a view parallel to the c axis. . . . .	43
32	Model of the $\gamma$ phase of Quinacridone with a view along the long molecular axis. . . . .	44
33	Model of the $\gamma$ phase of Quinacridone with a view along the c axis. The horizontal axis is the a axis and the vertical axis is the b axis. . . . .	44
34	$\theta/2\theta$ scan of the finely grinded Quinacridone powder . . . . .	45

35	Geometrical interpretation of the peak shift. The circle illustrates the goniometer circle. The colors black and blue stand for different angles of incidence. $\vec{k}_0$ is the incoming wave vector which is diffracted once at the center of the goniometer circle into the wave $\vec{k}_1$ and once deeper inside the sample into $\vec{k}_1'$ . The red parts along the circumference stand for the difference in the angle of detection (peak shift). Additionally the angular dependence of the peak shift can be seen. . . . .	46
36	$\theta/2\theta$ scan of finely grinded Quinacridone powder. The black line is the experimental scan and the red line stands for a theoretical calculation of the $\beta$ phase. . . . .	47
37	$\theta/2\theta$ scan of finely grinded Quinacridone powder. The black line is the experimental scan and the blue line stands for a theoretical calculation of the $\gamma$ phase. . . . .	47
38	$\theta/2\theta$ scan of finely grinded Quinacridone powder. The black line is the experimental scan and the green line stands for a theoretical calculation of the $\alpha$ phase. . . . .	48
39	$\theta/2\theta$ scan of a 27.4 nm thick film of Quinacridone on a Cu(110) surface (sample 1). The peak at $41.1^\circ$ is from the $\beta$ phase and originates in the (-112) plane. . . . .	50
40	$\omega$ scan of the (-112) peak ( $2\theta 41.1^\circ$ ) from a 27.4 nm thick film of Quinacridone on a Cu(110) surface (sample 1). . . . .	51
41	Polefigure measured at $2\theta = 41.57^\circ$ on a 27.4 nm thick film of Quinacridone on a Cu(110) surface (sample 1). Different colors denote different crystallite orientations for the $\beta$ phase, except red. Red crosses represent the copper substrate and its directions. The numbers are the hkl indices of the planes. The stereogram was calculated with the $\beta$ phase and the $\{-112\}$ family of planes parallel to the Cu(110) surface. . . . .	52
42	Definition of the angle between the copper [001] direction and the long molecular axis. The coloring is identical with the coloring from figure 41, giving the information which crystallite has a positive or negative rotation with respect to the [001] direction of copper. . . . .	54
43	Top view of the $\beta$ phase with the (-112) plane parallel to the surface. The two unit cell vectors have a magnitude of $30 \text{ \AA}$ and $6.9 \text{ \AA}$ . The angle between them is $80^\circ$ . The hole plane is spanned by two molecules per lattice point (cyan borderd). . . . .	54
44	Collection of the models associated to the $\beta$ phase with the (1-12) plane parallel to the surface of a 27.4 nm thick film of Quinacridone on a Cu(110) substrate (sample 1). . . . .	55
45	$\theta/2\theta$ scan of a 21.4 nm thick film of Quinacridone on a Cu(110) surface (sample 2). The peak at $42.5^\circ$ is from the $\alpha$ phase and is indexed with (1-12). . . . .	57
46	$\omega$ scan of the (1-12) peak ( $2\theta 42.5^\circ$ ) from a 21.4 nm thick film of Quinacridone on a Cu(110) substrate (sample 2). . . . .	58
47	Polefigure measured at an angle of $2\theta = 38.72^\circ$ on a 21.4 nm thick film of Quinacridone on a Cu(110) substrate (sample 2). This is exactly between the $2\theta$ angles of the (101) and the (1-11) plane. Different colors denote different crystallite orientations for the $\alpha$ phase, except red. Red crosses represent the copper substrate and its directions. The numbers are the hkl indices of the planes. The stereogram was calculated with the $\alpha$ phase and the $\{1-12\}$ family of planes parallel to the Cu(110) surface. . . . .	59
48	Topview of the (1-12) plane of the $\alpha$ phase. It can be recreated by a two dimensional lattice with one molecule per lattice point. The basis is given inside the cyan dotted parallelogram. . . . .	59
49	Collection of the models associated to the $\alpha$ phase with the (1-12) plane parallel to the substrate surface of a 21.4 nm thick film of Quinacridone on a Cu(110) substrate (sample 2). . . . .	61
50	$\theta/2\theta$ scan of a 30 nm thick film of Quinacridone on a Cu(110)-(2x1)O reconstruction (sample 3). The peak at $42.16^\circ$ is from the $\alpha$ phase and originates in the (1-12) plane. A second $\alpha$ phase can be seen in the peak at $38.6^\circ$ . It corresponds to the (1-11) plane. . . . .	63

51	$\omega$ scan of the (1-12) peak ( $2\theta$ 42.16°) from a 30 nm thick film of Quinacridone on a Cu(110)-(2x1)O reconstruction (sample 3). . . . .	64
52	Polefigure measured at an angle of $2\theta = 21.019^\circ$ on a 30 nm thick film of Quinacridone on a Cu(110)-(2x1)O reconstruction (sample 3). This corresponds to the (0-11) plane. Different colors denote different crystallite orientations for the $\alpha$ phase, except red. Red crosses represent the copper substrate and its directions. The numbers are the hkl indices of the planes. The stereogram was calculated with the $\alpha$ phase and the {1-12} family of planes parallel to the Cu(110)-(2x1)O surface. . . . .	65
53	Polefigure measured at an angle of $2\theta = 21.019^\circ$ on a 30 nm thick film of Quinacridone on a Cu(110)-(2x1)O reconstruction (sample 3). This corresponds to the (0-11) plane. Different colors denote different crystallite orientations for the $\alpha$ phase, except red. Red crosses represent the copper substrate and its directions. The numbers are the hkl indices of the planes. The stereogram was calculated with the $\alpha$ phase and the {1-11} family of planes parallel to the Cu(110)-(2x1)O surface. . . . .	66
54	Polefigure measured at an angle of $2\theta = 38.72^\circ$ on a 30 nm thick film of Quinacridone on a Cu(110)-(2x1)O reconstruction (sample 3), which is exactly between the (101) and the (1-11) plane. Different colors denote different crystallite orientations for the $\alpha$ phase, except red. Red crosses represent the copper substrate and its directions. The numbers are the hkl indices of the planes. The stereogram was calculated with the $\alpha$ phase and the {1-12} family of planes parallel to the Cu(110)-(2x1)O surface. . . . .	68
55	Topview of the (1-11) plane of the $\alpha$ phase. It can be recreated by a two dimensional lattice with one molecule per lattice point. The basis can be seen inside the cyan dotted parallelogram. . . . .	70
56	Topview of the (1-12) plane of the $\alpha$ phase. It can be recreated by a two dimensional lattice with one molecule per lattice point. The basis can be seen inside the cyan dotted parallelogram. . . . .	71
57	Collection of the models associated to the $\alpha$ phase with the (1-12) plane parallel to the Cu(110)-(2x1)O surface of a 30 nm thick film of Quinacridone (sample 3). . . . .	71
58	Collection of the models associated to the $\alpha$ phase with the (1-11) plane parallel to the Cu(110)-(2x1)O surface of a 30 nm thick film of Quinacridone (sample 3). . . . .	72
59	Experimental measured photoemission spectra of the $\beta$ phase of Quinacridone at normal emission (solid line) and at a takeoff angle of $50^\circ$ (dotted line). The contributing orbitals and their wavefunction are displayed. Their energetic positions are given in the colored vertical lines.[20] . . . . .	74
60	UPS measurement of a dosing series (uptake curve) of Quinacridone on a Cu(110) substrate. The measurement was performed along the [001] azimuthal direction at a takeoff angle of $50^\circ$ . The dosing series starts with clean copper at the bottom (black line), continues with a monolayer (red), a bi-layer (blue) and stops at a multilayer with a thickness of 5.5 ML. . . . .	76
61	Determination of the work function and the thickness of the monolayer for Quinacridone on a Cu(110) surface. It converges exponentially against 3.8 eV. A thickness of 3.2 Å was observed. . . . .	76
62	Heating series of a 18 Å thick film of Quinacridone on a Cu(110) substrate in the [001] azimuthal direction at three different takeoff angles: $30^\circ$ , $50^\circ$ and normal emission. Different curves correspond to different heating steps. Starting at the bottom with $25^\circ$ and increasing in temperature towards the top curve. . . . .	78

63	Selected spectra out of the ARUPS series on a monolayer of Quinacridone on a Cu(110) substrate. Different colors denote to different takeoff angles: blue 50 °, red 35 ° and black normal emission. Considering only one color the top line corresponds to the [001] substrate direction, followed by 45 ° between the two azimuths and the bottom curve represents the [1-10] direction. . . . .	80
64	Theoretical calculations (density functional theory) for the momentum maps of an isolated Quinacridone molecule. The figure on the left side illustrates the momentum map of the HOMO, whereas the figure on the right side shows the momentum map of the LUMO. The coloring corresponds to the intensity. . . . .	81
65	Theoretical calculations (density functional theory) for the wavefunctions of an isolated Quinacridone molecule. The left figure shows the wave function of the HOMO and the right part of the figure shows the wavefunction of the LUMO. The coloring corresponds to the sign of the wavefunction. . . . .	81
66	Uptake curve at elevated sample temperature (140 °C) measured along both azimuthal directions at a fixed takeoff angle of 50 °. The left figure shows the measurement along the [001] direction, whereas the right figure represents the measurement along the [1-10] direction. The bottom line is not clean copper. This dosing series started with a monolayer of Quinacridone evaporated onto the Cu(110) substrate while the temperature was hold constant at 140 °C. . . . .	83
67	Angle resolved ultraviolet photoemission spectroscopy of a 3.2 Å thick film of Quinacridone on the Cu(110) surface. The left side shows the ARUPS in the [001] substrate direction and the right side illustrates the ARUPS along the [1-10] azimuth. The black line was taken at normal emission. Moving up the takeoff angle with respect to normal emission increases. . . . .	84
68	Angle resolved ultraviolet photoemission spectroscopy of a 7 Å thick film of Quinacridone on the Cu(110) surface. The left side shows the ARUPS in the [001] substrate direction and the right side illustrates the ARUPS along the [1-10] azimuth. Different colors denote to different takeoff angles. . . . .	85
69	Angle resolved ultraviolet photoemission spectroscopy of a 30 Å thick film of Quinacridone on a Cu(110) substrate (about 10 monolayer). The left side shows the ARUPS in the [001] substrate direction and the right side illustrates the ARUPS along the [1-10] azimuth. Different colors denote to different takeoff angles. . . . .	86
70	Heating series of a 30 Å thick film of Quinacridone on a Cu(110) surface at three different takeoff angles, along the [001] azimuth. The bottom line is the starting point and by moving up the temperature increases. . . . .	88
71	UPS measurement of clean copper (black), a Cu(110)-(2x1)O reconstruction (red), a Cu(110)-(2x1)O reconstruction with 3.4 Å of Quinacridone (blue) and a Cu(110)-(2x1)O reconstruction with 30 Å of Quinacridone (dark cyan). The measurements were carried out in the [001] azimuth at three different takeoff angles. . . . .	90
72	Angle resolved ultraviolet photoemission spectroscopy of a monolayer of Quinacridone on a Cu(110)-(2x1)O reconstruction in both azimuthal directions and 45 °C in between. The coloring is related to different takeoff angles. . . . .	92
73	Angle resolved ultraviolet photoemission spectroscopy of a 30 nm thick film of Quinacridone on a Cu(110)-(2x1)O reconstruction as template for the growth. The left side shows an ARUPS series in the [001] azimuth. The graph on the right side illustrates an ARUPS series in [1-10] direction. The coloring is related to different takeoff angles. . . . .	93

74	Density functional theory calculations with the GGA functional for the wavefunction and the momentum map of the HOMO-9. The left side shows the wavefunction of the HOMO-9 in real space and the coloring takes account for the sign of the wavefunction. The right side shows a momentum map of the HOMO-9. These calculations were performed by Daniel Lueftner. . . . .	93
----	--	----

## References

- [1] A. D. McNaught and A. Wilkinson. *Compendium of Chemical Terminology The Gold Book, Second Edition*. Blackwell Scientific Publications: Oxford, 1997.
- [2] M. Oehlzelt and R. Resel. *Applied X-ray Diffraction*. Laboratory exercise, 2012.
- [3] P. A. Anderson. The work function of copper. *Phys. Rev.*, 76:388–390, Aug 1949.
- [4] S. Berkebile. Epitaxial organic films and their interfaces, 2009.
- [5] M. Birkholz. *Thin Film Analysis by X-ray Scattering*. WILEY-VCH Verlag, 2006.
- [6] G. Chiarotti. *Landolt-Boernstein - Group III Condensed Matter Volume 24D*. Springer Berlin Heidelberg, 1996.
- [7] E. D. Glowacki, L. Leonat, M. Irimia-Vladu, R. Schwodiauer, M. Ullah, H. Sitter, S. Bauer, and N. Serdar Sariciftci. Intermolecular hydrogen-bonded organic semiconductors quinacridone versus pentacene. *Applied Physics Letters*, 101(2):–, 2012.
- [8] A. O. Fletcher Jones. Towards high throughput single crystal neutron diffraction of hydrogen bonded molecular complexes, 2012.
- [9] H. Fukunaga, D. G. Fedorov, M. Chiba, K. Nii, and K. Kitaura. Theoretical analysis of the intermolecular interaction effects on the excitation energy of organic pigments: solid state quinacridone. *The journal of physical chemistry. A*, 112(43):10887–94, October 2008.
- [10] J. Kueppers G. Ertl. *Low Energy Electrons and Surfaces Chemistry*. VCH, 1985.
- [11] E. D. Glowacki. *Hydrogen-Bonded Semiconducting Pigments for Air-Stable Field-Effect Transistors*. Advanced Materials, 2013.
- [12] H. Lueth H. Ibach. *Festkörperphysik*. Springer, 2008.
- [13] J. N. Israelachvili. *Intermolecular and Surface Forces*. Academic Press.
- [14] R.W. James. *The Optical Principles of the Diffraction of X-ray*. G Bell and Sons LTD, 1962.
- [15] G. A. Jeffrey. *An Introduction to Hydrogen Bonding*. Oxford University Press, 1997.
- [16] R.A.L. Jones. *Soft Condensed Matter*. Oxford University Press, 2002.
- [17] A. I. Kitaigorodskii. The principle of close packing and the condition of thermodynamic stability of organic crystals. *Acta Crystallographica*, 18(4):585–590, Apr 1965.
- [18] C. Kittel. *Introduction to Solid State Physics*. John Wiley & Sons, 2005.
- [19] G. Koller. Controlling the organic-inorganic interface: Organic molecules on nanostructured surfaces, 2001.
- [20] D. Lueftner, S. Refaely-Abramson, M. Pachler, R. Resel, M. G. Ramsey, L. Kronik, and P. Puschnig. Experimental and theoretical electronic structure of quinacridone. *Phys. Rev. B*, 90:075204, Aug 2014.
- [21] H. Lueth. *Solid Surfaces, Interfaces and Thin Films*. Springer, 2001.
- [22] D. N. Mermin N. W. Ashcroft. *Solid State Physics*. Oldenbrough, 2007.

- [23] E. F. Paulus, F. J. J. Leusen, and M. U. Schmidt. Crystal structures of quinacridones. *CrystEngComm*, 9(2):131, 2007.
- [24] B. Predel. *Landolt-Boernstein - Group IV Physical Chemistry Volume 12A*. Springer Berlin Heidelberg, 1999.
- [25] R. Resel. *Soft Matter Physic*. lecture, 2012.
- [26] R. Resel, O. Lengyel, T. Haber, O. Werzer, W. Hardeman, D. M. de Leeuw, and H. J. Wondergem. Wide-range three-dimensional reciprocal-space mapping: a novel approach applied to organic monodomain thin films. *Journal of Applied Crystallography*, 40(3):580–582, May 2007.
- [27] I. Salzmann and R. Resel. *STEREOPOLE*: software for the analysis of X-ray diffraction pole figures with IDL. *Journal of Applied Crystallography*, 37(6):1029–1033, Dec 2004.
- [28] M. Wagner. *Electronic structure of clean and Ni-O decorated stepped Rh(553) surfaces*. Master Thesis, 2008.